University of Texas at El Paso

ScholarWorks@UTEP

Open Access Theses & Dissertations

2024-05-01

Earth Abundant Catalyst For Evironmental Sustainability Applications

Javier Hernandez
University of Texas at El Paso

Follow this and additional works at: https://scholarworks.utep.edu/open_etd

Part of the Inorganic Chemistry Commons, and the Mechanics of Materials Commons

Recommended Citation

Hernandez, Javier, "Earth Abundant Catalyst For Evironmental Sustainability Applications" (2024). *Open Access Theses & Dissertations*. 4104.
https://scholarworks.utep.edu/open_etd/4104

This is brought to you for free and open access by ScholarWorks@UTEP. It has been accepted for inclusion in Open Access Theses & Dissertations by an authorized administrator of ScholarWorks@UTEP. For more information, please contact lweber@utep.edu.

EARTH ABUNDANT CATALYST FOR EVIRONMENTAL SUSTAINABILITY APPLICATIONS

JAVIER HERNANDEZ ORTEGA

Doctoral Program in Chemistry

APPROVED:

Juan C. Noveron, Ph.D., Chair

James Salvador, Ph.D.

Jose A. Hernandez, Ph.D.

Jose L. Banuelos, Ph.D.

Stephen L. Crites, Jr., Ph.D.
Dean of the Graduate School

Copyright

By

Javier Hernandez Ortega
2024

Dedication

To my family for all the love and affection…

To my lovely wife for her love and support in my darkest moments…

And to my friends for their help and inspiration.

EARTH ABUNDANT CATALYST FOR EVIRONMENTAL SUSTAINABILITY APPLICATIONS

by

JAVIER HERNANDEZ ORTEGA, BSc.

DISSERTATION

Presented to the Faculty of the Graduate School of
The University of Texas at El Paso
in Partial Fulfillment
of the Requirements
for the Degree of

DOCTOR OF PHILOSOPHY

Department of Chemistry and Biochemistry
THE UNIVERSITY OF TEXAS AT EL PASO
May 2024

Acknowledgements

I wish to express my heartfelt gratitude to my advisor, Dr. Juan C. Noveron, for his invaluable mentorship and the profound lessons he has taught, not only in the academic research but also in personal development. His unwavering guidance, mentorship, and insightful advice have been instrumental in my evolution as an independent scientist, an effective educator, a capable mentor, and a collaborative team player. Under his expert tutelage, I have learned the art of self-driven research, equipping me to advance my own scholarly pursuits with confidence and purpose.

I extend my sincere gratitude to the esteemed members of my dissertation committee, Dr. James Salvador, Dr. Jose Hernandez, and Dr. Jose L. Banuelos. Their invaluable advice and constructive suggestions were of utmost significance during the research process and the development of this dissertation.

My sincere appreciation goes to Dr. Echegoyen and Dr. Narayan for generously granting me access to the laboratory instruments under their purview. I would like to extend special gratitude to Dr. Bernal for his invaluable assistance, particularly in the realm of high-resolution transmission electron microscopy. Furthermore, I warmly acknowledge and thank Dr. Bonifacio, Dominc Dieguez and Dr. Meta their kind support and guidance in the meticulous characterization of the materials synthesized during my Ph.D. research.

I would like to thank Dr. Sultana Kazi and Md Ariful Ahsan, and all the dedicated students within Dr. Noveron's lab. Their camaraderie, collaborative spirit, and unwavering assistance were invaluable during my tenure in the lab.

I wish to gratefully acknolodge the generous funding sources that made my research journey possible: The National Science Foundation grants ERC Nanotechnology-Enable Water

Treatment Center 1449500, CHE-0748913, and USD 2014 – 38422-22078. Additionally, I would like to express my appreciation for the financial support provided through my Teaching Assistantship by the Department of Chemistry and the College of Science at The University of Texas at El Paso.

Abstract

The development of experimental methodologies for synthesizing a diverse range of metallic and metal oxide nanoparticles tailored for sustainable water treatment applications was investigated. These nanoparticles are prepared using environmentally friendly and scalable synthesis methods, underscoring their potential for large-scale production. Synthesized nanoparticles are harnessed for various processes, including catalysis and electrocatalysis, with a primary objective of degrading and removing organic pollutants from water. Key to this research is the encapsulation of nanoparticles within solid supports. Multiple methodologies are explored to engineer supports that ensure nanoparticle stabilization, monodispersion, and prevent unintended release into the environment. Two alternative approaches were evaluated for the treatment of organic dyes, one within the factory encompassing the synthesis of Al@C nanomaterial through a MOF intermediate and the development of magnetic Fe@C nanomaterial, both exhibiting excellent catalytic activity in the reductive degradation of organic dyes such as MO, MB and 4-NP, comparable to Pt and Au based catalysts in terms of degradation time and rate constants. While, for water remediation and sanitization in already contaminated rivers it was successfully synthesized several ZnO nanoparticles through a saccharide combustion methodology, all of them showing very good catalytic activity in the MO degradation assisted by UV and sunlight. The stability studies also show the potential reusability of this nanomaterial, losing less than 10% of activity after 3 cycles. Finally in the field of energy for electrocatalytic applications two new nanomaterials based on Fe and Co were successfully synthesized and tested for electrocatalysis in OER, showcasing very good results comparable to rare earth metals such as Ru.

Table of Contents

List of Tables

List of Figures

List of Illustrations

NANOPARTICLES

Chapter 1: Synthesis, Properties, and Application of Nanoparticles in electrocatalyst and water remediation.

1.1. Introduction.

Nanotechnology has garnered significant attention over the years, with nanoparticles serving as its fundamental building blocks. Nanoparticles typically exhibit dimensions within the range of 1 to 100 nanometers and can be constructed from a variety of materials, including carbon, metals, metal oxides, or organic compounds[1]. Notably, nanoparticles exhibit distinct physical, chemical, and biological properties at the nanoscale when compared to their counterparts at larger scales. These unique properties are attributed to their relatively larger surface area-to-volume ratio, resulting in increased reactivity or stability in chemical processes, enhanced mechanical strength, and other advantageous characteristics[2]. Consequently, the exceptional properties of nanoparticles have found diverse applications in various fields.

Nanoparticles exhibit unique properties based on their size, shape, and material composition[3]. They can be categorized by their dimensionalities: Zero-Dimensional (0D) nanoparticles, such as nanodots, occupy only a single point in space. One-Dimensional (1D) nanoparticles, like graphene, have a single dimension, often length. Two-Dimensional (2D) nanoparticles, such as carbon nanotubes, possess two dimensions, typically length and breadth, with reduced height. Three-Dimensional (3D) nanoparticles, like gold nanoparticles, maintain all three dimensions, including length, breadth, and height. These diverse nanoparticle characteristics make them valuable for a wide range of applications.

Nanoparticles come in a variety of shapes, sizes, and structures, offering flexibility for different applications. They can be spherical, cylindrical, tubular, conical, hollow-core, spiral, flat, or exhibit irregular shapes. Their size typically ranges from 1 nm to 100 nm. The nanoparticle surface can be uniform or irregular, featuring surface variations. Additionally, nanoparticles can exist in both crystalline and amorphous forms, and they may consist of single or multiple crystal solids, sometimes found in loose or agglomerated configurations[4].

A wide range of synthesis methods for nanoparticles are continuously being developed and refined to enhance their properties and reduce production costs. These methods are often tailored to produce nanoparticles with specific characteristics, such as improved optical, mechanical, physical, and chemical properties[5]. Advances in instrumentation have significantly improved the characterization of nanoparticles, enabling more precise applications. Nowadays, nanoparticles find applications in various fields, from everyday objects like cooking vessels and electronics to advanced industries like renewable energy and aerospace. Nanotechnology plays a crucial role in achieving a cleaner and more sustainable future.

Nanotechnology is significantly improving our daily lives by enhancing the performance and efficiency of various everyday objects. It is contributing to a cleaner environment by ensuring safer air and water quality, as well as enabling clean and sustainable sources of renewable energy. The field of nanotechnology has garnered widespread attention, leading to increased investments in research and development by top institutions, industries, and organizations[6,7].

Nanotechnology has evolved into an advanced scientific discipline with extensive ongoing research aimed at practical implementations[8]. Researchers are continuously exploring new applications to enhance the efficiency and performance of objects or processes while simultaneously reducing costs, making these innovations accessible to a broader audience. Given its remarkable efficiency and environmentally friendly attributes, nanotechnology holds great promise for the future[9].

1.2. Solid Supports.

Metal nanoparticles exhibit intriguing properties that find applications across various fields, including catalysis[10,11], sensing[12,13], energy storage[14,15], and medicine[16,17]. Their remarkable contributions to heterogeneous catalyst development are well-established, characterized by exceptional catalytic performance and reusability. Central to their catalytic prowess is the surface interaction of reactants, facilitated by partially filled d-orbitals, promoting adsorption and catalysis at active sites. Consequently, the quantity of surface metal atoms emerges as a pivotal factor in catalytic processes. Smaller metal nanoparticles possess a proportionally larger specific surface area and an increased count of surface atoms, thereby augmenting active sites. Reducing the diameter of metal nanoparticles from 10 nm to 1 nm, for instance, elevates the proportion of "effective" accessible metal atoms from 20% to 90% [18]. Hence, precise control over metal nanoparticle size is imperative. Metal nanoparticles, typically characterized by an average size of less than 3 nm, hold significant promise in catalysis applications[19].

Usually, small nanoparticles possess a substantial surface area and exhibit a narrow size distribution, affording an abundance of accessible active sites crucial for heterogeneous catalysis. Notably, the thermodynamic instability of this small nanoparticles arises from their elevated count of surface atoms[20,21,22]. According to mechanisms like migration-coalescence and Ostwald ripening, smaller particles spontaneously aggregate, leading to the formation of larger particles. The aggregation of these nanoparticles results in diminished catalytic activity, thereby underscoring the need for strategies to preserve their dispersion and stability during catalysis. In this regard, solid supports and organic capping agents represent two widely employed methods for the synthesis of these nanoparticles, serving the dual purpose of preventing aggregation and enhancing their practical applicability in catalysis[23].

These solid supports are instrumental in guiding the development of such nanoparticles and precisely regulating their dimensions through a combination of spatial confinement and electronic influences. Consequently, a variety of these nanoparticles can be produced by altering the types and structures of the supports. Furthermore, by strengthening the interaction between metal nanoparticles (MNPs) and the support, the aggregation of MNPs can be reduced, thus enhancing the catalyst's longevity. Typically, metal ions or atoms with unfilled d-orbitals can form coordination bonds with electron-rich atoms on the support, such as sulfur, nitrogen, oxygen, and others. Therefore, supports often necessitate the presence of heteroatoms or organic functional groups to facilitate the growth and stabilization of these nanoparticles[24,25,26]. The confinement effect of supports on these nanoparticles also yields significant advantages. This effect is particularly pronounced in porous materials featuring aligned or interconnected nanopores or channels, as they effectively restrict the growth of metal nanoparticles. Various supports, including covalent organic frameworks (COFs), metal-organic frameworks (MOFs), and porous carbon materials, can be purposefully designed and synthesized to achieve fine-tuned control over the size of metal nanoparticles at the molecular level. By merely altering the chemical composition of solid supports, a range of these nanoparticles with exceptional activity, extensive surface area, and a tightly controlled size distribution can be synthesized [27,28,29].

The synthesis of these small nanoparticles, as well as their size control and dispersion, can be effectively managed through the utilization of solid supports. In the catalytic process, both the supports and these nanoparticles jointly influence the catalytic activity. Consequently, in situ synthesis of these small nanoparticles in the presence of a support, with regulated nucleation and growth, offers a promising approach for their controlled synthesis and application in catalysis. The support's structure and properties significantly impact the growth and utility of these nanoparticles. Numerous organic porous materials, such as COFs and MOFs, can be meticulously designed at the atomic level, allowing precise control over pore size and shape to govern the size and morphology of these nanoparticles. The ordered porous support structure promotes a narrow size distribution of these nanoparticles. Carbon-based materials like porous carbon, hollow carbon, and graphene exhibit outstanding chemical and thermal stability. Additionally, carbon materials are cost-effective and readily available, making them economical support materials. The design of supports is multifaceted. Porous supports offer effective confinement for the growth of these nanoparticles and prevent their aggregation through site isolation. Simultaneously, the high specific surface area provides numerous available active sites and anchoring sites. Furthermore, there is a synergistic catalysis effect facilitated by these nanoparticles and supports. Certain supports have the capability to absorb reaction substrates, leading to an increased local concentration of these substrates near the nanoparticles and thereby expediting catalytic reactions. Precisely controlling the shape and diameter of these nanoparticles remains a challenge but is crucial for enhancing their performance in heterogeneous catalysis.

1.3. Water pollution.

Water contamination encompasses a wide array of pollutants, each originating from diverse sources. Contaminants can be broadly classified into three categories: biological, organic, and inorganic. Organic pollutants can be further subdivided into specific groups, including pharmaceuticals and personal care products, pesticides, veterinary compounds, industrial chemicals and byproducts, food additives, as well as more specialized categories like nanomaterials and plasticizers[30,31,32]. These organic contaminants find their way into the environment through various pathways, including wastewater discharges, septic systems, hospital effluents, subsurface storage of industrial waste, and potential contamination via groundwater-surface water interactions[33,34,35]. While some sources of pollution are clearly defined, such as industrial discharges, resource extraction (e.g., mining, fracking), and landfills (referred to as point-source pollution), others, like stormwater runoff, catchment areas, and field drains, contribute to diffuse pollution, spanning a larger geographic area[36,37].

Inorganic pollution encompasses a broad spectrum of contaminants that differ in nature and characteristics. Generally, inorganic contaminants can be categorized into groups, such as heavy metals, oxyanions and cations, halides, and radioactive materials[38]. These contaminants are known for their persistence and resistance to degradation, which poses challenges for biological systems attempting to eliminate them[39]. For example, elevated nitrate levels in drinking water can increase the risk of methemoglobinemia and the formation of carcinogenic nitrosamines[40]. Similarly, excessive fluoride, while beneficial in small amounts, can lead to adverse health effects, including dental problems, skeletal fluorosis, and crippling, when present in higher concentrations[41]. Among inorganic contaminants, heavy metals like arsenic, cadmium, chromium, copper, mercury, lead, and zinc are commonly studied. Inorganic contamination can also originate from natural processes, including volcanic eruptions and soil erosion. However, human activities have substantially heightened the levels and variety of heavy metal pollution in the environment[42,43]. Wastewater from various industrial processes, such as mining, fracking, plastic production, smelting, and alloy manufacturing, represents a prominent source of toxic heavy metal pollution.

Elevated concentrations of heavy metals can exert extensive adverse impacts on ecosystems by permeating food chains and accelerating their circulation[44]. Given our limited ability to remove many of these heavy metals from our bodies, substantial or repeated exposure to these toxic substances can result in long-lasting health issues, encompassing skin diseases, kidney disorders, gastrointestinal and hepatic problems, hypertension, and even the development of cancer, among other health concerns.

1.3.1. Application of Nanomaterials in Water Remediation.

Nanomaterials are structures characterized by their dimensions, typically less than 100 nanometers. They exhibit a multitude of exceptional properties, notably their high surface-to-volume ratio and significant activity as a catalyst. Nanomaterials have found applications in various fields due to their unique properties. They have been employed in pharmaceuticals, cosmetics, electronics, energy-related technologies, and, more recently, in environmental applications. The emerging field of environmental nanotechnology has gained substantial attention, despite concerns about potential environmental contamination from engineered nanomaterials[45]. These nano-sized materials are now being harnessed as innovative tools in various environmental applications, such as environmental sensing and biomonitoring, capturing pathogenic bacteria, and wastewater treatment, among other uses. This marks a growing and dynamic area of research and development with the potential to address critical environmental challenges.

The treatment of wastewater is a crucial endeavor, particularly as water sources become contaminated with a variety of pollutants, including metal ions, radionuclides, organic and inorganic compounds, pathogenic bacteria, and viruses[46]. This necessity has been exacerbated by factors such as prolonged droughts, population growth, and increasingly stringent health-based regulations. As a result, there is a growing demand for clean water, making wastewater purification a pressing issue.

Nanomaterials play a pivotal role in addressing these water treatment challenges. They have found diverse applications in this field, with innovations aimed at developing novel technologies for water desalination standing out as particularly exciting and promising. Water treatment processes typically involve the adsorption and photocatalytic degradation of contaminants, often facilitated by nanoparticles (NPs). Additionally, bioremediation methods are employed to transform pollutants in water and soil from toxic forms to less harmful substances, contributing to the overall goal of environmental remediation.

Nanoscale materials offer significant potential to enhance water quality through various applications. These include the use of nanosorbents, nanocatalysts, and bioactive nanoparticles (NPs) to effectively remove contaminants. Additionally, the development of nanostructured catalytic membranes and NP-enhanced filtration methods has opened up innovative approaches to water purification. Emerging strategies in water treatment, such as dendrimer-enhanced ultrafiltration, are continually being explored, with nanomaterials at the forefront of these developments[47,48,49]. For instance, nanoporous activated carbon fibers, with an average pore size of 1.16 nm, have demonstrated the ability to adsorb harmful compounds like benzene, toluene, xylene, and ethylbenzene[50]. Moreover, certain nanomaterials exhibit intrinsic antibacterial properties, further expanding their utility in water treatment[51]. A particularly noteworthy characteristic of nanomaterials, especially NPs, is their significantly higher surface area compared to bulk materials. This feature allows for the functionalization of nanomaterials with various chemical groups, enabling enhanced target-specificity and customization of these materials for specific water treatment applications.

Traditional water treatment techniques, including reverse osmosis, distillation, bio-sand filtration, coagulation-flocculation, and standard filtration methods, face challenges in efficiently eliminating heavy metal ions from water. Consequently, there is a growing demand for more robust methods and advanced membranes in water purification.

Nanomaterials offer a promising solution for treating various types of contaminated water, including inorganic pollutants, dye wastewater, papermaking wastewater, pesticide wastewater, and oily wastewater. One of the primary functions of nanomaterials in water treatment is as sorbents, where they effectively capture and separate pollutants from the contaminated water. Additionally, certain nanomaterials exhibit outstanding reductive capabilities, making them valuable for reducing the toxicity of pollutants. An excellent example is zero-valent iron, which has seen extensive use in chemically reducing organic pollutants in situ or aboveground in contaminated water. Notably, zero-valent iron provides the advantage of not generating intermediate by-products typically observed when using commercial iron powders, enhancing its environmental applicability[52].

In environmental studies, it's crucial to consider six key characteristics of nanomaterials for discrimination. These include size, dissolution/solubility, surface area, surface charge, surface chemical composition, and additional factors like size distribution, crystal structure, morphology, agglomeration/dispersion. These characteristics significantly influence how nanomaterials behave, react, and perform in various environmental applications[53]. For example, nanomaterials with hierarchical structures often possess a high surface area and increased surface functional groups, making them well-suited for the removal of heavy metal ions like arsenic (As(V)) and chromium (Cr(VI))[54].

Nanotechnology has seamlessly integrated with various biologic and biomedical systems and applications, extending its reach to environmental risk assessment, monitoring, and water treatment. While the potential of nanomaterials in these applications is promising, the availability of substantial quantities of nanomaterials at economically feasible prices for large-scale water treatment remains a significant challenge for industrial implementation.

However, with proper assurance of efficacy and safety, nanomaterials hold the key to addressing several critical issues in water purification. These include desalination of brackish water, facilitating the recovery of valuable and toxic metals to aid brine disposal, contributing to the development of novel chlorine-free biocides, and eliminating a wide range of water contaminants. In the near future, nanomaterials are expected to become indispensable components of water purification and treatment systems and facilities, playing a vital role in addressing pressing global water quality and scarcity challenges.

1.4. Application of Nanomaterials for Electrocatalysis.

Since the dawn of the first and second industrial revolutions, technological innovations have played a pivotal role in shaping modern society, offering unprecedented levels of convenience and progress. However, many of these technological marvels have been powered by carbon-based fuels, including coal, natural gas, and petroleum[55]. While these fuels have undoubtedly fueled human progress, their consumption has led to resource depletion and dire environmental consequences. These challenges have prompted a diverse and dedicated group of researchers to explore alternative energy sources and technologies[56,57,58].

This pursuit of sustainable energy solutions has given rise to a wide array of innovative ideas and concepts. Researchers and engineers are focused on achieving more efficient energy conversion and storage systems[59,60]. Notable examples include alkaline water electrolysis, fuel cells, and metal-air batteries, among others. While the designs of these systems can be quite complex, at their core, they all function as two-electrode systems[61,62]. The cathode plays a crucial role in enabling essential reactions, such as the hydrogen evolution reaction (HER) or oxygen reduction reaction (ORR), while the anode is tasked with driving processes like the oxygen evolution reaction (OER) or the oxidation of various chemical fuels[63,64]. These energy technologies hold the promise of reshaping our world and steering it towards a more sustainable future[65].

The practical utilization of various energy conversion and storage systems has been hindered by a significant challenge: the sluggish kinetics of the oxygen evolution reaction (OER). OER is a four-electron-proton coupled reaction, while the hydrogen evolution reaction (HER) involves only a two-electron transfer. As a result, OER inherently demands a higher energy input, manifesting as a higher overpotential, to surmount the kinetic barrier and proceed. This kinetic hurdle has been a focal point of research due to its impact on the overall efficiency of these energy systems[66].

Electrochemical water splitting stands out as a highly promising technology for the clean production of hydrogen fuel. Unlike conventional methods that rely on fossil fuels, water splitting is free from carbon emissions and boasts an impressive thermodynamic efficiency of around 80% [67]. The process consists of two main half-reactions: the hydrogen evolution reaction

(HER) occurring at the cathode and the oxygen evolution reaction (OER) happening at the anode[68]. Electrocatalysts play a pivotal role in this context, and they must perform several crucial functions. First, they stabilize electrons and holes to prevent their recombination. Second, they provide active sites for the adsorption of hydrogen and oxygen molecules. Lastly, they lower the activation energy required for the oxidation of water at the anode and the reduction of protons at the cathode[69]. To be effective, electrocatalysts should exhibit large surface areas, high electrical conductivity, and exceptional stability in the electrolyte medium. These attributes collectively enhance the sustainability of HER and OER activities in diverse electrolyte environments, thus making electrocatalysts pivotal for advancing water splitting technology[70].

Nanomaterials have gained significant attention in recent years as electrode materials due to their exceptional mechanical and electrical properties[71,72]. One key advantage of nanomaterials is their large surface area, which lowers the energy barrier for electrochemical reactions and reduces charge transfer resistance by facilitating electron transfer at electrode surfaces[73,74]. Traditionally, noble metals like Pt have been considered benchmark electrode materials for the hydrogen evolution reaction (HER), and materials like IrO2 and RuO2 for the oxygen evolution reaction (OER)[75,76]. However, the limited availability of noble metals, their high cost, and their tendency to agglomerate in electrolytes make them less suitable for large-scale applications. Additionally, Pt exhibits slow reaction kinetics in basic solutions, and Ru-based catalysts are not universally effective across different pH conditions[77,78].

Therefore, there's a pressing need to develop electrocatalysts that are cost-effective, highly active, and stable for HER and OER. Over the past few decades, scientists have extensively investigated various transition metal-based derivatives, including alloys, oxides, hydroxides, sulfides, phosphides, and selenides, as potential electrocatalysts for HER and OER in both acidic and basic environments[79,80,81,82]. However, transition metal derivatives often come with limitations[83]. For instance, Co, Ni and metal sulfides may not perform well in alkaline media for OER [84]. Furthermore, differences in catalytic mechanisms mean that electrocatalysts effective for HER may not work as well for OER. To address these challenges and develop next-generation, highly active electrocatalysts with broad applications, nanomaterials are being explored as a crucial avenue of research.

Electrocatalytic water splitting has traditionally involved considering a range of materials, including both noble metals (e.g., Pt, Ru, Ir) and non-precious metals (e.g., Fe, Co, Ni). However, relying solely on noble metal-based electrocatalysts for this purpose is currently viewed as less promising due to several factors[85]. These include the high cost, limited availability in nature, agglomeration tendencies, and their susceptibility to electrocatalysis poisoning.

Conversely, using only non-precious metals as electrocatalysts may not yield efficient results for industrial applications. A promising strategy has emerged, which involves supporting one of these metals or creating alloys by combining noble metals with non-precious metals, or vice versa. This approach has proven effective for water splitting reactions, offering several advantages. It not only reduces the need for precious noble metals but also enhances electrocatalyst performance by improving electrical conductivity, stability, creating synergistic effects, tuning the d-band structure, and optimizing the energy required for oxygen adsorption on the catalyst's surface[86].

1.4.1. Carbon-based materials and MOF as solid support for OER.

In the realm of electrocatalysis, carbon materials are emerging as highly promising candidates due to their exceptional attributes. These materials possess a potent combination of high electrical conductivity and a customizable porous structure, making them well-suited for the development of efficient oxygen and hydrogen electrocatalysts.

Traditionally, precious metals and their compounds have held the spotlight as active materials for critical electrochemical processes, such as the use of platinum (Pt) for oxygen reduction reactions (ORR) and hydrogen evolution reactions (HER), and iridium dioxide (IrO2) for oxygen evolution reactions (OER). However, the limited availability and high cost of these precious metals have prompted extensive exploration of non-precious metal-based alternatives for electrocatalysis. This quest for sustainable solutions has led researchers to investigate a class of materials where carbon materials play a pivotal role.

Carbon materials, with their multifunctional capabilities, serve as excellent supports for the active sites, enhancing charge and mass transport in the electrocatalytic processes. Over the past decade, carbon materials have also demonstrated their intrinsic activity as electrocatalysts in their own right, proving to be proficient materials for a range of functions, including ORR, OER, HER, and multifunctional electrocatalysis. Their versatile structural features and inherent reactivity have sparked widespread interest and investigation, positioning them as key players in the ongoing pursuit of efficient and sustainable electrochemical technologies.

Extensive research into the active centers and nanostructures of carbon-based materials has driven the rapid exploration of innovative electrocatalysts that are free from metals or noble metals. These materials exhibit well-defined electronic structures in their active sites and encompass diverse classes such as metal-organic frameworks (MOFs), covalent organic frameworks (COFs), diyne, conjugated porous polymers, and atomic-metal-doped carbons. Remarkably, metal-free and noble metal-free carbon electrocatalysts have demonstrated outstanding activity in the oxygen reduction reaction (ORR), surpassing the performance of Pt/C in basic solutions. However, their electrocatalytic activity in acidic electrolytes still lags behind that of existing metal-based inorganic catalysts and cannot rival noble-metal-based systems.

Nonetheless, carbon-rich electrocatalysts provide an ideal platform for studying the intrinsic activity of active centers at the atomic or molecular level. They facilitate the exploration of kinetic reaction processes taking place on the catalyst's surface and the understanding of mass transfer between the liquid electrolyte and the solid catalyst. Therefore, the in-depth investigation of these new materials has the potential to substantially increase the progress in electrocatalyst specially for hydrogen and oxygen generation process.

The synthesis of carbon materials encompasses various approaches, with commonly employed methods including the exfoliation of graphite and graphite-like materials, the polymerization of small molecules, and the pyrolysis of carbon-containing substances. A relatively recent and highly effective avenue involves utilizing metal-organic frameworks (MOFs), Metal-organic frameworks (MOFs) denote a unique category of materials characterized by their intricate structure, which involves the linkage of metal ions or clusters with organic molecules serving as linkers. These materials are renowned for their open crystalline structure, which imparts them with exceptional porosity. The structure of MOFs is further distinguished by its inherent structural flexibility and tunable functionality, allowing for a diverse range of applications and adaptability.

The pyrolysis of MOFs, first introduced as a precursor/template for porous carbons in 2008, has gained considerable traction as a valuable means of producing carbon-based materials with diverse morphologies and compositions. These carbon materials, derived from MOFs, offer several notable advantages when applied to oxygen reduction reactions (ORR), oxygen evolution reactions (OER), and hydrogen evolution reactions (HER) electrocatalysis:

1. Controlled Morphology and Porosity: The morphology and porosity of these carbon-based materials can be finely tuned to expose active sites and facilitate efficient mass transport during electrocatalytic reactions.

2. Uniform Dispersion of Metal Species: MOF-derived carbon materials can achieve well-dispersed metal species, enhancing their utilization efficiency. This even distribution occurs at the atomic level within MOF precursors.

3. Heteroatom Incorporation: The inclusion of heteroatoms in MOF linkers facilitates the doping of carbon materials, resulting in precisely defined heteroatom functional groups. This imparts tailored polarity and intrinsic redox-active sites to the materials.

4. Pore Encapsulation: MOFs are advantageous for encapsulating precursors within their pores, enabling the well-dispersed incorporation of various species into the resulting carbon-based materials. This includes single-atom metal sites and heteroatom species coordinated to them.

While it's important to acknowledge that MOF synthesis may sometimes involve expensive organic ligands, the remarkable benefits of MOF-derived carbon materials make them a compelling subject of investigation for the development of new functional carbon materials. Additionally, ongoing efforts are directed toward reducing the cost of MOFs and facilitating their widespread practical applications.

1.5. Research Objectives.

This research thesis is fundamentally concerned with the development of experimental procedures designed to create nanoparticles, both metallic and metal oxide, for application in sustainable water treatment technologies. The materials synthesized include a range of nanoparticles, encompassing noble metals such as gold and palladium, transition metals like cobalt, iron, and copper, metal oxide nanoparticles, and polymeric material. The synthesis methodologies employed are not only facile but also amenable to large-scale production and environmentally friendly to the ecosystem.

These nanoparticles find utility in various processes, including catalysis, electrocatalysis, and adsorption, with a central goal of degrading and eliminating organic pollutants from water. In doing so, they contribute to the advancement of water remediation methods. Additionally, these nanoparticles hold promise in the realm of energy-related applications, particularly in the context of the oxygen evolution reaction, which is a key component of sustainable energy production. A pivotal component of this thesis involved the meticulous encapsulation of nanoparticles through the utilization of solid supports. This process necessitated the exploration of various methodologies designed to synthesize and engineer a diverse set of solid supports, each of which played an indispensable role in the stabilization of the nanomaterials.

The primary objectives were to achieve monodispersion of nanoparticles within the supports and to circumvent any potential leaching of nanomaterials into the environment. This was accomplished by effectively trapping or encapsulating the nanoparticles within a well-structured porous matrix, ensuring their integrity, and preventing their unintended release. To fulfill these objectives, the research focused on the development of three distinct categories of solid supports:

1. Metal-Organic Frameworks (MOFs): MOFs, known for their crystalline structure and high porosity, offered an excellent platform for immobilizing and stabilizing nanoparticles. Their well-defined pores and versatile chemistry enabled precise control over nanoparticle dispersion.

2. Covalent Organic Frameworks (COFs): COFs, with their robust covalent bonds and tunable properties, provided another avenue for encapsulating nanoparticles. Their unique structural attributes contributed to nanoparticle stabilization and ensured the prevention of leaching.

3. Porous Biocarbon Frameworks: The development of porous biocarbon frameworks represented a novel approach to nanoparticle encapsulation. These frameworks, derived from biologically sourced materials, offered exceptional porosity and an environmentally friendly aspect, thus aligning with sustainable practices.

Furthermore, the solid supports exhibited high electrical conductivity, a feature of paramount importance in electrocatalytic applications. This exceptional conductivity expanded their utility to include a wide spectrum of electrochemical processes, making them highly versatile and valuable in various applications, particularly in the context of water treatment and the oxygen evolution reaction process. The combination of nanoparticle encapsulation and enhanced electrical conductivity is a key factor in the multifaceted approach to sustainable and efficient water treatment technologies.

The research delves into the intricate processes of nanoparticle synthesis, their structural and compositional analysis, and the examination of their performance in the context of water treatment and energy conversion. The thesis seeks to contribute to the development of eco-friendly and efficient solutions for addressing water pollution challenges and harnessing sustainable energy sources.

NANOPARTICLES IN WATER REMEDIATION

Chapter 2: Catalytic reduction of organic pollutants carried out by Al@C NPs using MOF as a template.

2.1. Introduction

The separation and purification of water and wastewater streams have gained considerable prominence due to their crucial role in meeting stringent regulatory standards, particularly from an environmental standpoint[87]. Recent years have witnessed an unprecedented surge in industrialization and urbanization, reaching unprecedented levels. While freshwater sources constitute one of the most heavily exploited resources, they are also among the most severely impacted by both industrial and communal activities[88],[89]. Alarming statistics indicate that approximately 4 billion tons of industrial and communal waste are generated globally each year[90]. This relentless increase in water body contamination, coupled with the growing scarcity of fresh and potable water resources, has emerged as a paramount concern for humanity. The root of this issue lies in the widespread and severe pollution resulting from untreated wastewater discharges[91],[92]. A multitude of industries, spanning textiles, tanneries, food processing, pulp and paper manufacturing, distilleries, and more, routinely release untreated waste into water bodies, exacerbating the contamination of these vital resources[93],.

Wastewater discharge contains a plethora of contaminants, many of which have known adverse health effects. Notably, these contaminants include pesticides, textile dyes, and plasticizers, among others, each posing a significant risk to both the environment and public health[94]. As the demand for freshwater continues to escalate, there has been a pressing need for rapid advancements in wastewater management strategies, with an emphasis on water recycling and reuse[95,96]. The process of recycling wastewater and rendering it safe for consumption has necessitated the development of effective methods for the removal of emerging contaminants[97]. However, achieving the complete decomposition of organic pollutants present in wastewater, such as organic dyes like methylene blue or methyl orange, nitro compounds, and phenols, has proven to be exceedingly challenging[98]. To address this formidable challenge, a common approach involves the reductive degradation of these pollutants, resulting in the formation of more environmentally friendly and easily removable compounds. This strategy marks a significant stride in addressing the negative impacts of these pollutants on both the environment and human health[99,100,101].

The catalytic reduction of these pollutants using noble metals such as platinum (Pt) and palladium (Pd) is indeed an effective alternative. However, the high cost associated with these noble metals, coupled with the challenge of separating the homogeneous catalyst from the reaction products, has limited their widespread commercial application. In response to these limitations, the scientific community has been motivated to explore new alternatives based on more affordable, abundant, and environmentally friendly metals or metal oxide compounds[102],[103],[104],[105],[106]. Examples include aluminum (Al) and aluminum oxide (Al2O3), zinc (Zn) and zinc oxide (ZnO), as well as nickel (Ni) and nickel oxide (NiO). These earth-abundant materials hold promise for catalytic applications, offering a more cost-effective and sustainable solution for the reduction of pollutants in wastewater and other environmental remediation processes[107,108,109].

Metal-Organic Frameworks (MOFs) represent an exciting and innovative class of nanoporous materials that combine inorganic metal ions or clusters with organic ligands to form structures with one-dimensional, two-dimensional, or three-dimensional topological arrangements[110,111,112]. These hybrid materials have garnered significant attention for their remarkable properties and versatile applications[113,114,115]. MOFs are considered highly promising functional nanomaterials and exhibit superior potential in a wide range of fields, including liquid separation, luminescence sensing, gas storage, drug delivery, catalysis, and environmental remediation. Their numerous advantages make them particularly well-suited for addressing challenges in environmental management[116,117]. MOFs are characterized by their solid nature with exceptional crystallinity. This crystalline structure facilitates the precise determination of their spatial arrangement through techniques like single-crystal or poly-crystal diffraction. Additionally, MOFs possess remarkable porosity and specific surface area, setting them apart from other porous materials. They can exhibit specific surface areas as high as approximately 7140 square meters per gram (m2/g) and exceptionally high porosity, reaching around 94%. One of the key features of MOFs is their structural diversity and adjustability[118]. MOFs can be constructed by combining different metal ions or clusters with various bridging ligands and coordination structures through coordination bonds. This versatility results in a wide array of MOF structures with distinct properties and functions[119]. Researchers can even design and synthesize MOF-based composites with specific frame structures through rational monomer design and synthetic assembly, offering tailor-made solutions for various applications[120]. The organic ligands that form MOFs are typically long and characterized by σ-bonds. Similarly, the coordination bonds within MOFs also exhibit characteristics like reversibility and deformability[121]. This flexibility in their structure and bonds endows MOFs with unique functionality and enables them to adapt to various conditions and applications, making them highly valuable materials in the field of materials science and beyond[122].

MOFs exhibit a remarkable degree of flexibility, a characteristic that distinguishes them from traditional porous materials like inorganic molecular sieves. This flexibility is a key feature that imparts unique properties and functions to MOFs, making them highly versatile materials:

- **Physicochemical Changes**: The flexibility of MOFs allows them to undergo particular physicochemical changes in response to external conditions. This property can be harnessed for various applications, including controlled release of molecules, adsorption, and catalysis.
- **Multi-Step Adsorption/Desorption Processes**: MOFs can engage in multi-step adsorption and desorption processes due to their flexibility. This behavior is particularly valuable in applications where selective and sequential adsorption or release of molecules is required.
- **Rich in Physical and Chemical Functions**: The porous nature of MOFs, whether composed of pure organic or organic-inorganic hybrid materials, results in surfaces with multifarious physical and chemical functions. These functions make MOFs highly adaptable to a wide range of applications, from gas separation to drug delivery.
- 4. **Easy Modifiability**: MOFs are amenable to easy modification. Their modular synthesis approach enables the incorporation of various functionalities as constituent building blocks. Additionally, the reversibility of MOFs' coordination bonds and the possibility of functionalizing organic ligands provide avenues for altering their structure and functional properties. This flexibility in design and modification enhances the versatility of MOFs for diverse applications.

Overall, MOFs' combination of flexibility, diverse functions, and ease of modification positions them as promising materials for addressing complex challenges in fields such as environmental remediation, catalysis, and materials science[123]. Their adaptability to changing conditions and precise tunability make them valuable tools for researchers and engineers seeking innovative solutions[124].

Despite the numerous advantages of MOFs outlined above, some challenges persist in their applications as powdered materials for environmental governance. The nanoscale size of powdered MOFs can lead to aggregation, resulting in blockages in water treatment systems, reduced adsorption efficiency, and even secondary pollution. Additionally, powdered MOFs are prone to consumption or erosion during practical applications, diminishing their service life and increasing operating costs. The synthesis of multifunctional MOFs with controllable size and shape, along with excellent selectivity, can be complex, and large-scale production of cost-effective MOFs for industrial applications remains a significant endeavor. Furthermore, the use of MOFs in large-scale industrial applications is hampered by immature production methods, uncertainty about cycle life, and concerns about unstable biocompatibility. To fully leverage MOFs' excellent characteristics while addressing these practical challenges, MOFs are often incorporated into polymer matrices to form membranes, mitigating issues related to regeneration and potential safety concerns, such as undesirable leakage. Despite these challenges, MOFs have found applications in a wide range of fields, including reversible gas storage, sensing, catalysis, ion conductivity, biomedical imaging, and drug delivery, demonstrating their adaptability and unique properties for addressing complex problems and advancing research and innovation in various domains. Researchers continue to explore ways to optimize MOFs for practical applications and scale up their production for industrial use, further unlocking their potential in environmental governance and beyond[125].

The integration of metal nanoparticles (NPs) with MOFs has become a focal point of research interest, and for good reason. This fusion not only simplifies the development of hybrid materials that incorporate the favorable characteristics of both MOFs and NPs but also frequently triggers functional synergies between these components. These synergistic effects can significantly enhance their individual strengths and help offset their respective drawbacks. Researchers have particularly explored the immobilization and incorporation of various types of metal nanoparticles into MOF networks. This includes noble metals such as platinum (Pt), palladium (Pd), silver (Ag), as well as semi-noble metals like ruthenium (Ru) as guest species within MOFs. These efforts have met with success and have opened up new possibilities for designing and engineering materials with tailored properties and enhanced performance in a wide range of applications[126,127]. To mention few, Kaskel and coworkers incorporated Pd NPs into MOF-5 [{Zn4O (BDC)3}, BDC = 1,4-benzenedicarboxylate] framework via the solution impregnation method[128]. Similarly, synthesis and catalytic performance of a variety of MOF based hybrid catalysts such as Pd/MIL-101 [129] [Cr3F(H2O)2O(BDCNH2) 3 nH2O], (BDC-NH2 = 2-aminoterepthalate), Pd/MIL-101-NH_2 [130], Au/ZIF-L[131], Pt/MIL-101[132], Pd/UiO-66:[133] [Zr6O4(OH)4(BDC)6], Pd/ZIF-8 [(Zn(MeIM)$_2$[134], MeIM = 2-methylimidazole)], Ru/La-BTC [(La(1,3,5-BTC).6H2O)][135] and Pd@Al-MIL- 100 [(Al3O(OH)(H2O)2(BTC)2・nH2O; BTC = benzenetricarboxylate)] has been reported[136]. Immobilization of Au and Pt NPs over pyrolytic products of UiO-66 MOF has also been reported[137,138]. Xu’s group has successfully demonstrated the stabilization of bimetallic core–shell structured NPs mainly on a zeolitic imidazolate framework, ZIF-8[139]. In almost all these NP-MOF related reports, MOFs containing single metal centers have been used as supports for stabilizing metal nanoparticles. There are just very few reports on MOFs with mixed metal centers and mixed linkers as the stabilizing matrices for NP immobilization[140,141,142].

The utilization of metal oxide nanoparticles (MONPs), known for their abundant catalytic centers, has been explored for water treatment applications. However, several challenges have arisen in their practical use. These include the high surface energy and surface area of MONPs, agglomeration issues following the nucleation step in the synthesis process, and the potential leaching of these metal oxide NPs into water bodies, adding to pollution concerns. To address these drawbacks, one effective solution is the immobilization of these NPs within a porous material. This immobilization allows for better control of the active sites and helps mitigate agglomeration issues.

Metal-Organic Frameworks (MOFs) hold significant promise as a support material for immobilizing metal oxide NPs. MOFs offer several advantageous features, including flexibility and tunability, thermal and chemical stability, the ability to modify the inner pore surface, and versatility in shaping and introducing functionalities[143]. Additionally, MOFs facilitate moderate electron interaction between the NPs and the organic linkers, a crucial factor for catalytic processes. This controlled interaction helps overcome agglomeration problems by securely housing the NPs within the porous MOF structure, thus allowing precise control of their size and achieving a highly monodisperse nanomaterial. Consequently, MOFs serve as an excellent platform for addressing the challenges associated with the utilization of MONPs in water treatment applications. Furthermore, the presence of a metal center atom within MOFs offers the advantage of coordination with the organic linker. This coordination enhances the immobilization and fixation of metal oxide nanoparticles (MONPs), thereby improving the recyclability and reutilization of the material in catalytic processes[144]. Constructing the MOF around pre-stabilized NPs synthesized in-situ results in the formation of a material referred to as MO-NPs@MOF. This composite material shows great potential for numerous applications, especially in the heterogeneous catalysis field, where precise regulation of active sites and improved catalytic performance are of paramount importance. The synergy between MOFs and pre-stabilized NPs within MO-NPs@MOF materials opens up new avenues for innovative and efficient catalytic processes[145].

Numerous endeavors have been dedicated to devising efficient methods for the production of carbon-supported metal nanoparticles (MNPs). Existing approaches encompass chemical vapor deposition, explosion, and hard-templating methods, among others. Nevertheless, these procedures commonly involve multi-stage synthesis, high energy use, and the utilization of complex equipment. Consequently, there remains a challenge in devising a cost-effective and straightforward approach for the preparation of carbon-encapsulated metal nanoparticles. In this context, the templating synthesis of carbon-encapsulated metal nanoparticles using Metal-Organic Frameworks (MOFs) emerges as a promising alternative[146]. This technique presents a more streamlined and economical approach for achieving the intended result. Recent research endeavors aimed at fabricating affordable MNP-based catalysts using MOFs as self-sacrificial templates have garnered significant attention within the materials science community[147]. This innovative approach holds great potential for advancing the field and addressing the demand for more sustainable and economically viable catalytic materials[148,149].

The ability to convert 3D-Metal-Organic Frameworks (MOFs) into hierarchically nanostructured functional materials using environmentally friendly methodologies is paving the way for the development of sustainable green energy storage and conversion technologies. One notable achievement in this area is the facile synthesis of carbon-encapsulated metal nanoparticles through the direct carbonization of MOFs under an inert atmosphere, typically using nitrogen (N2) or argon (Ar)[150]. However, it's worth noting that while many MOFs have served as precursors for creating their respective metal-carbon composites, the synthesis process for most MOFs often entails prolonged reaction times, high temperatures, the use of toxic organic solvents, and expensive ligands[151]. These factors present challenges that researchers continue to address in their quest for more eco-friendly and cost-effective methods of producing advanced materials for green energy applications.

Among the various Aluminum-based Metal-Organic Frameworks (Al-MOFs), Al-BDC MOFs offer the advantage of being easily prepared using a readily available and cost-effective ligand, terephthalic acid. The primary objective of this research is to utilize this economical ligand, terephthalic acid, to synthesize Al-BDC MOFs, which can then serve as precursors for the fabrication of Al@C nanocatalysts through direct carbonization. In comparison to costly ligands like trimesic acid or 1,3,5-benzenetricarboxylic acid, which function as tridentate ligands. and have been utilized in a limited number of studies for the synthesis of metal@carbon nanocomposites, the choice of terephthalic acid as the ligand in this study offers a more cost-effective alternative. Additionally, terephthalic acid is a bidentate ligand, which may result in distinct properties of the resulting MOFs, including differences in porosity, geometry, and more. To the best of our knowledge, the method presented in this work, which involves the synthesis of Al/Al2O3 nanoparticles encapsulated within a carbon framework through the direct carbonization of a metal-organic framework serving as a self-sacrificial template, has not been previously published. This innovative approach holds promise for the development of efficient catalysts for the reduction of organic dyes and nitro compounds in water remediation applications.

2.2. Materials and Methods.

2.2.1. Chemicals and Reagents.

All chemicals employed in this study were utilized as received, and no additional purification steps were carried out. The following chemicals were used in the preparation of the magnetic Al@C nanocatalyst. Terephthalic acid or benzene-1,4-dicarboxylic acid (BDC) (synthesis grade), dimethylformamide (DMF) (anhydrous, 99.8%), aluminum nitrate nonahydrate (Al(NO3)3.9H2O) (ACS reagent, ≥98.0%) were purchased from Sigma-Aldrich. Sodium borohydride (NaBH4) (powder, ≥98.0%) methanol (= 99.8%), ethanol (≥99.5%), methylene blue (MB) (dye\ content, ≥82%), Methyl orange (MO) (dye\ content > 98.0%) and 4-nitrophenol were purchased from Sigma-Aldrich. Deionized (DI) water (>18.20 MI cm resistivity) was used from the Milli-Q® instrument (Millipore Corporation).

2.2.2. Synthesis of Al-BDC MOF.

The synthesis of the Al BDC MOF was carried out using a straightforward solvothermal method. Initially, Al(NO3)3·9H2O (775 mg) was dissolved in 10 mL of deionized water in a 20 mL glass vial, aided by 5 minutes of sonication to ensure complete dissolution. Simultaneously, 132 mg of BDC (benzene-1,4-dicarboxylic acid) was weighed and placed in another 20 mL glass vial. To this vial, 10 mL of dimethylformamide (DMF) was added to dissolve the white powder, with an additional 5 minutes of sonication to aid dissolution. Subsequently, the solutions from both vials were combined in a 50 mL round-bottom flask (RBF) and stirred for an additional 15 minutes at room temperature. The resulting solution was then transferred to a metal reactor and tightly sealed. The container was put in an oven and subjected to heating at 100 °C for a duration of 24 hours. After cooling to room temperature, the milky white solid of Al BDC MOF was collected via vacuum filtration. The collected solid was washed three times with DMF and three times with deionized water. Finally, the solid was dried in a vacuum oven at 110 °C for 12 hours and stored in a sealed glass vial for further utilization.

2.2.3. Synthesis of Al@C nanocatalyst.

The synthesis of the Al@C nanocatalyst involved the direct carbonization of the precursor Al BDC MOFs. This process took place in a furnace at 600 °C under an argon gas flow for a duration of 3 hours, with a gradual heating rate of 5 °C per minute. Upon completion of the carbonization process, a distinct black product was obtained, clearly distinguishable from the initial white Al BDC MOFs. This black product was removed from the furnace, allowed to cool to ambient temperature, and subsequently preserved in a glass vial.

2.2.4. Characterization.

The synthesized nanocatalysts underwent several characterization techniques to assess their properties. Powder X-ray diffraction (XRD) patterns were obtained using a Bruker D8 Discover X-ray Diffractometer. To investigate their morphologies, microstructures, and elemental compositions, transmission electron microscopy (TEM) and scanning electron microscopy (SEM) equipped with energy-dispersive X-ray spectroscopy (EDS) instruments were employed. Furthermore, the thermal stability of the prepared materials was assessed using thermogravimetric analysis (TGA) conducted with a Mettler Toledo thermogravimetric instrument. Raman spectra of the nanocatalysts were collected using a DXR Smart Raman instrument equipped with a 532 nm laser. The absorbance of the pollutant solution, as well as the kinetics of the catalytic reduction reaction, were measured using a UV–Vis spectrophotometer (Model: Agilent Cary 50 Conc).

2.2.5. Catalytic degradation test.

Catalytic reduction trials were conducted for methylene blue (MB), 4-nitrophenol (4-NP), and methyl orange (MO) in a quartz cuvette with a path length of 1.0 cm. Each experiment utilized 4 mL of a 20 ppm pollutant solution (MB, 4-NP, or MO), 1 mg of the Al@C nanocatalyst, and 5 mg of NaBH4 as a reducing agent. Initially, the nanocatalyst was introduced into the pollutant solution and exposed to ultrasonic treatment for 2 minutes. Subsequently, NaBH4 was added to the mixture to initiate the catalytic reduction of the pollutants. The reduction reaction proceeded until the solution became colorless. UV–visible spectroscopy was employed to monitor the catalytic reduction of the pollutants at various time intervals across the wavelength range of 200 to 800 nm. The kinetics data for the reduction of 4-NP, MO, and MB were acquired by measuring the absorbance at their corresponding peak wavelengths: 400 nm for 4-NP, 465 nm for MO, and 660 nm for MB. The percentage reduction of each pollutant was calculated using the following equation (2.1).

$$\%\text{Conversion}=(\text{Co}-\text{Ct}/\text{Co})\times 100\% \qquad (2.1)$$

Where Co and Ct are the concentrations of the pollutants at time 0 and t of the catalytic reduction. The assessment of pollutant degradation involved the utilization of the following pseudo-first order kinetic equation. (2).

$$\ln(Ct/Ci)=-Kt \tag{2.2}$$

Where Ci and Ct are the concentrations of the pollutants at time 0 and t, respectively, t is the reaction time and K is the pseudo-first order reaction rate constant.

2.3. Results and Discussion.

2.3.1. Analysis of Crystalline Structure by XRD.

In this study, we successfully synthesized the Al BDC MOF precursor using a novel, environmentally friendly, and straightforward solvothermal method. Following that, we acquired the Al@C nanocatalyst through direct carbonization of the aforementioned Al BDC MOF precursor. During the carbonization process conducted in a furnace under an argon gas atmosphere at 600 degrees Celsius for 2 hours, the initial white milky powder underwent a significant color change, turning black.

To evaluate the crystal structure and purity of both materials the Al BDC MOF precursor and the Al@C nanocatalyst, we conducted X-ray diffraction (XRD) analyses. The XRD pattern of the Al BDC MOF precursor is presented in Figure 1a, clearly demonstrating its crystalline nature and confirming the successful synthesis of the MOF material. The X-ray diffraction (XRD) analysis provided valuable insights into the crystallographic properties of our materials. Figure 2.1a illustrates the XRD pattern of the Al BDC MOF precursor. The pattern exhibits two broad peaks at approximately 2Ө = 18° and 20°, as well as three sharper signals at 2Ө = 27°, 37°, and 45°. These diffraction peaks are characteristic of a monoclinic crystal system, specifically gibbsite (98-018-4003), which corresponds to Al(OH)3. The space group that best describes our system is p1 21c1, with Miller's indices (h, k, l) corresponding to the 0,0,2 space lattice. This close match between our measurement and the reference library confirms the high purity of the synthesized material.

In contrast, Figure 2.1b depicts the XRD pattern of the Al@C nanocatalyst obtained after the carbonization process. The pattern reveals the amorphous nature of the Al@C nanocatalyst. Despite the XRD analysis being conducted for 30 minutes, the obtained spectra consist mainly of broad signals, indicative of low crystallinity samples. The primary signals are located around 2Ɵ = 25° and 37°, aligning with a hexagonal crystal system of Al2O3 (98-009-9783) with a space group of r -3c. The Miller's index suggests the presence of two primary space lattices: (012) and (110). Additionally, around 2Ɵ = 43°, a signal is observed, corresponding to the (113) space lattice. Notably, the XRD pattern also exhibits small signals attributed to Al metallic species with a (104) crystal lattice. These findings conclusively demonstrate the successful transformation of the Al BDC MOF precursor into the Al@C nanocatalyst through the carbonization process.

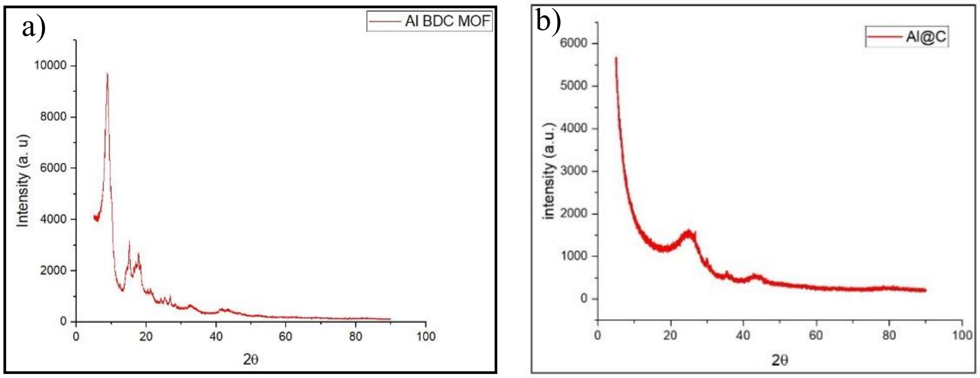

Figure 2.1: XRD pattern of (a) Al BDC MOF precursor; (b) Al@C nanocatalyst.

2.3.2. Morphological analysis by SEM and TEM.

The morphological characteristics of both the synthesized Al BDC MOF precursor and the resulting Al@C nanocatalyst were investigated using scanning electron microscopy (SEM) as well as transmission electron microscopy (TEM). The SEM images, as shown in Figure 2.2a and 2.2b, reveal that the Al BDC MOF precursor exhibits micron-sized particles with a distinct morphology.

Upon subjecting the Al BDC MOF precursor to carbonization at 600°C under an argon atmosphere, a significant transformation in morphology occurs, as depicted in Figure 2.2c and 2.2d. In the resulting Al@C nanocatalyst, the Al nanoparticles appear to decorate the surface of the carbon sheets and are also trapped within the porous carbon framework.

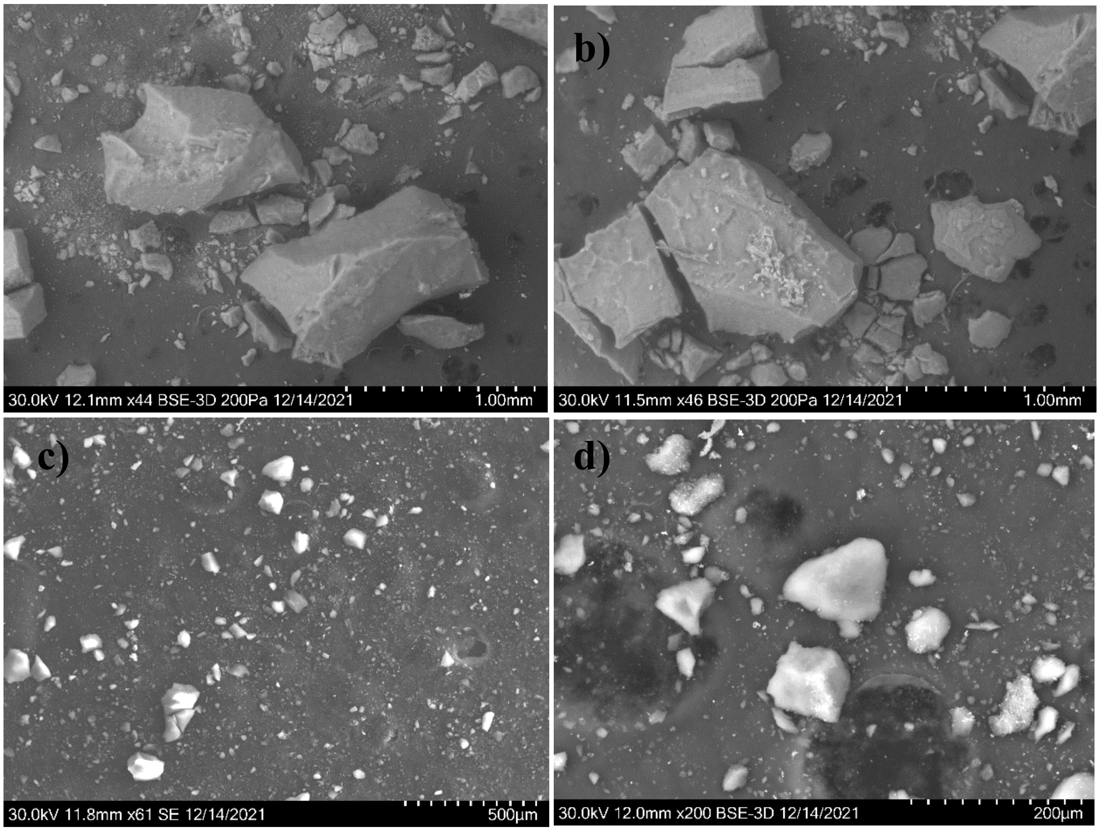

Figure 2.2: SEM images of (a, b) Al BDC MOF precursor and (c, d) Al@C nanocatalyst.

This change in size and shape post-carbonization serves as compelling evidence of the loss of organic material from the MOF precursor and the conversion of a portion of this organic material into porous carbon. Furthermore, it is evident that the collapsed frameworks of the Al BDC MOF during the carbonization process at 600°C in an argon atmosphere led to the formation of the Al@C nanocomposite.

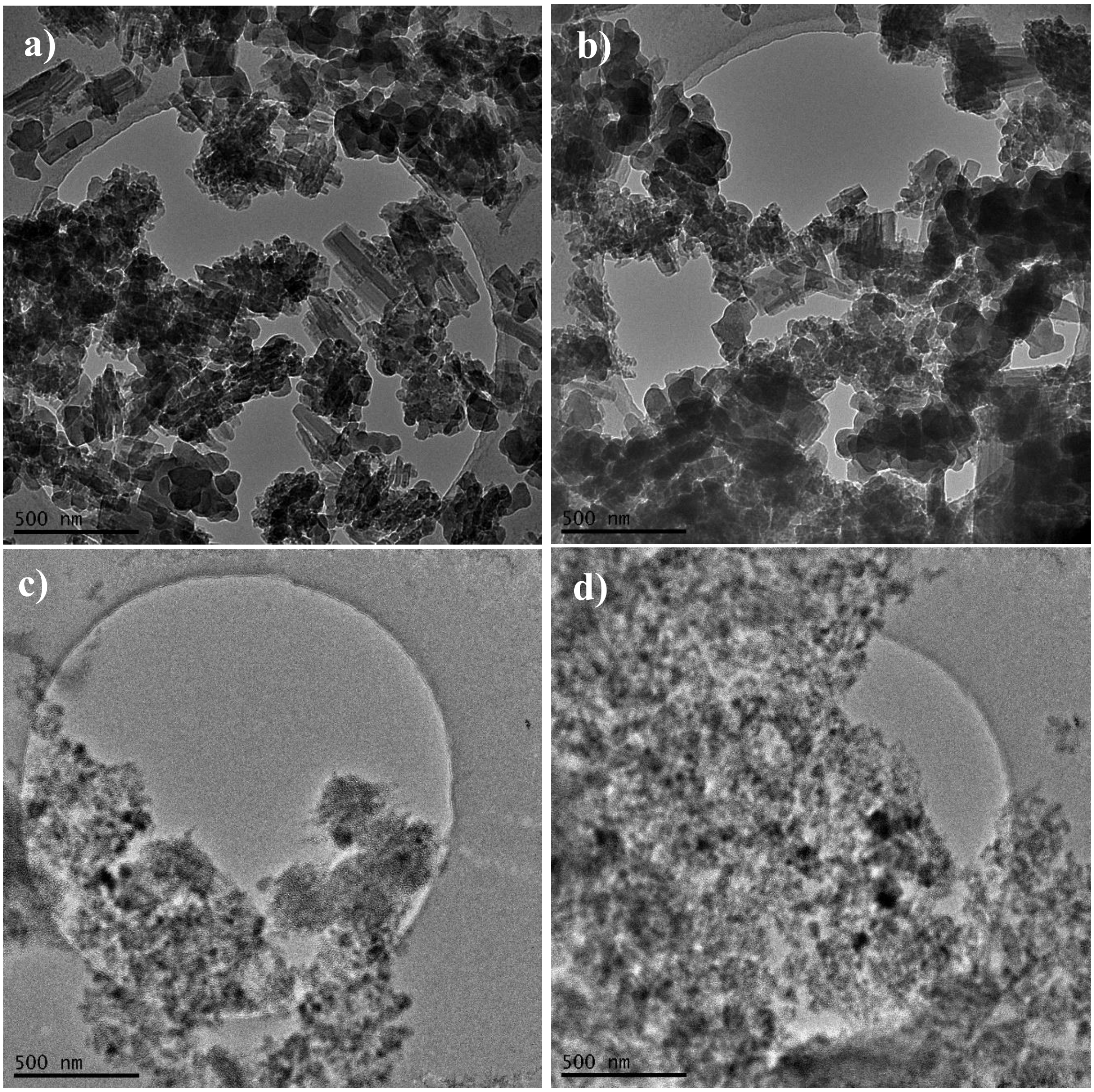

Figure 2.3: TEM images of (a, b) Al BDC MOF precursor and (c, d) Al@C nanocatalyst.

The MOF precursor also plays a significant role in preventing the agglomeration of nanoparticles. Because the precursor MOF material possesses some porosity, the nanoparticles initially formed during the seeding process are already anchored, occupying the spaces within the porous material.

This behavior is advantageous because during the subsequent growth step, when nanoparticles tend to agglomerate, most of the available sites within the porous structure are already occupied. This occupancy of sites within the MOF precursor effectively prevents agglomeration and results in highly monodisperse nanoparticles.

TEM microscopic analysis was conducted to gain a deeper understanding of the morphology of the prepared nanocatalyst and its corresponding parent materials, and Figure 2.3 illustrates these results. In Figure 3a and b, it is evident that the Al BDC MOF precursor exhibits a root-like shape with particle sizes ranging from 100 to 200 nm. The TEM images also reveal the crystalline nature of the material, which is consistent with the XRD pattern and its sharp, well-defined signals.

2.3.3. Chemical Composition Analysis by EDS.

To determine the chemical composition of the synthesized Al@C nanocatalyst, a sample was subjected to EDS (Energy-Dispersive X-ray Spectroscopy) analysis, and the corresponding results are shown in Figure 2.4. Elemental analysis reveals that Al@C is mainly composed of carbon (C), oxygen (O), and aluminum (Al), as seen in Figure 2.4a.

Additionally, elemental color mapping of the synthesized material was performed using EDS to visualize the distribution of elements within the sample. Based on the color mapping results shown in Figure 4b-d, it is evident that the Al@C nanocomposite contains only carbon

(C), oxygen (O), and aluminum (Al) elements, which aligns well with the EDS elemental analysis. These findings provide additional confirmation of the successful conversion of Al BDC MOF into the corresponding Al@C nanocomposite.

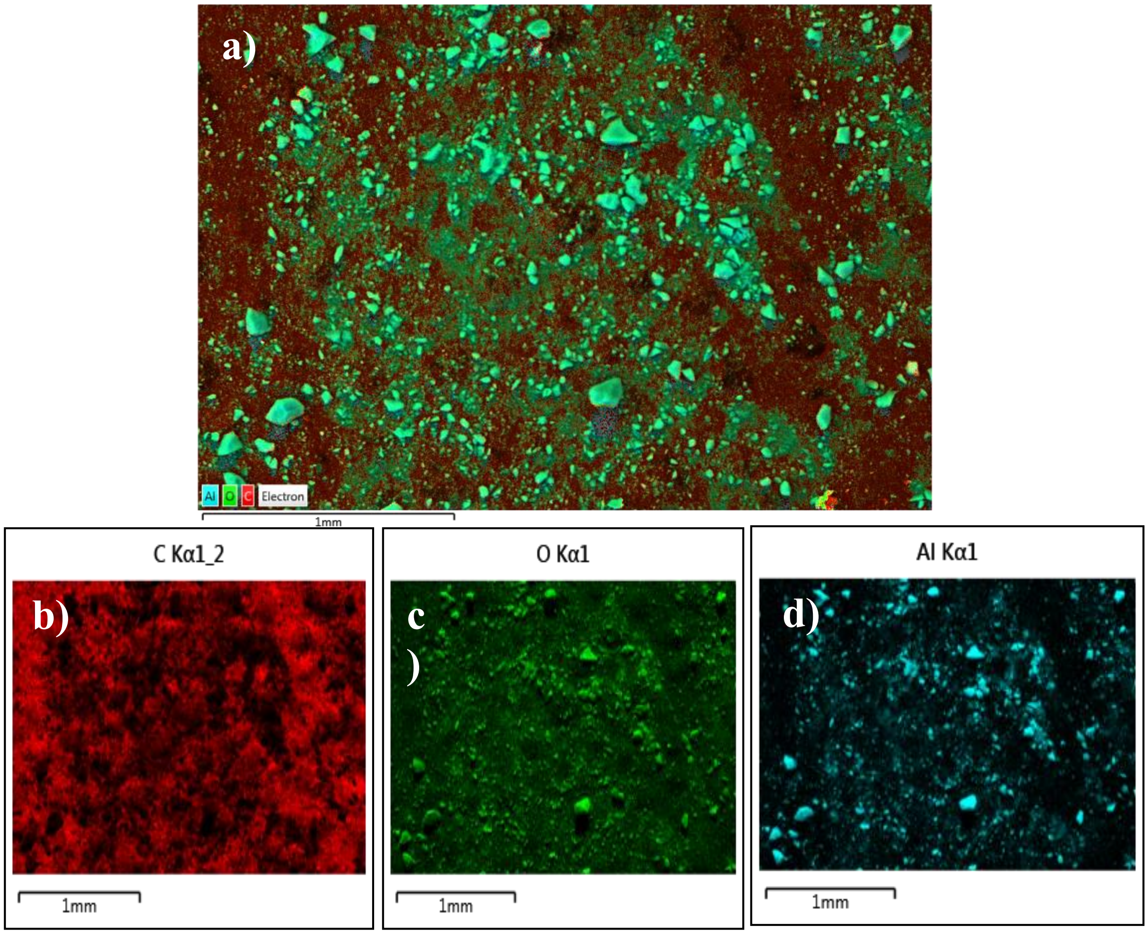

Figure 2.4: EDS elemental color mapping of Al@C nanocatalyst.

Figure 2.5 shows the results of the elemental analysis conducted via Energy Dispersive X-ray Spectroscopy (EDS). The analysis indicates a predominant presence of aluminum, accounting for approximately 41.1% of the sample's weight. Additionally, the EDS results reveal the presence of oxygen, originating from both atmospheric sources and potential aluminum oxide compounds. Furthermore, carbon is detected, likely arising from the carbonization of the MOF material.

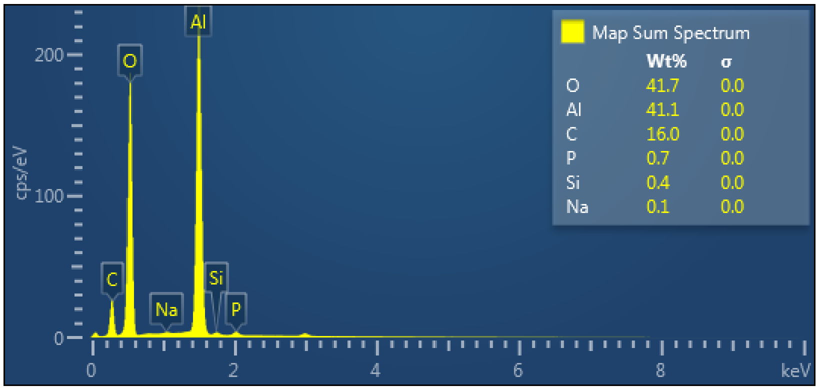

Figure 2.5: EDS elemental analysis of Al@C nanocatalyst.

2.3.4. Raman Analysis.

Raman spectroscopy is a valuable technique for characterizing carbon-based materials like the Al@C nanocatalyst. In the obtained Raman spectra, two distinct peaks are observed.

The G Band (Graphite Band), this prominent peak appears at around 1580 cm^{-1} in the Raman spectrum. This can be attributed to the E2g vibration mode of carbon atoms that are sp2-hybridized. This G band signifies the presence of well-arranged, hexagonal lattice structures of carbon atoms, which is a characteristic feature of graphitic carbon.

The D Band (Disorder or Defect Band), located at approximately 1347 cm^{-1} in the Raman spectrum, this band is associated with disorderly arranged carbon atoms, defects, or the presence of non-hexagonal carbon structures within the material. The D band is often used to assess the degree of disorder or the number of defects in carbon-based materials[152].

The Intensity Ratio (ID/IG) is a critical parameter in Raman spectroscopy. It provides valuable insights into the level of disorder and the presence of defect sites within the carbon material. The ID/IG ratio in Raman spectroscopy provides important information about the carbon-based materials. It serves as an indicator of both the degree of graphitization and the presence of defect sites. The degree of graphitization is inversely proportional to the ID/IG ratio, where a lower ID/IG ratio suggests a higher degree of graphitization. This indicates more ordered and well-structured carbon arrangements, resembling the crystalline structure found in graphite, with hexagonally arranged carbon atoms. Conversely, a higher ID/IG ratio suggests an increased number of defect sites and disorder within the carbon material. Defects can encompass various irregularities, including disordered carbon atom arrangements, the presence of non-hexagonal structures, and other deviations from perfect carbon lattice order. Analyzing the Raman spectrum of the Al@C nanocatalyst allows us to assess the quality of the carbon structure, the presence of defects, and the degree of graphitization. These factors are crucial for evaluating the suitability of carbon-based materials for various applications, including catalysis.

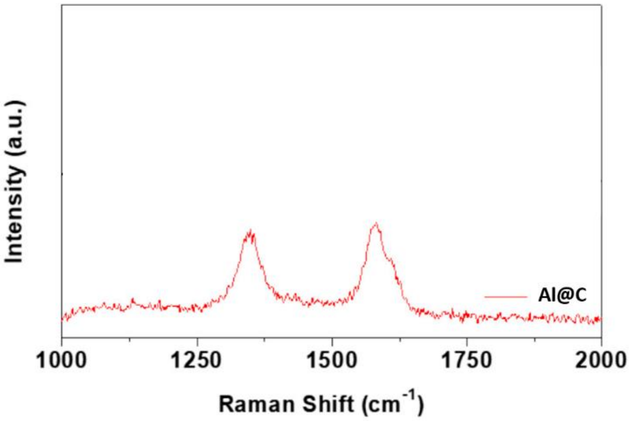

Figure 2.6: Raman spectrum of Al@C nanocatalyst.

The Raman spectra of the nanocatalyst presented in the Figure 2.6 exhibit a reduced intensity of the D band relative to the G band, signifying the presence of sp2 hybridized carbon species with well-structured graphitized pore walls. Specifically, the ID/IG values for the Al@C nanocatalyst fall within the range of approximately 0.88. These observed ID/IG values are similar to those typically found in reduced graphene oxide and graphene oxide, which are also around 1. This similarity in ID/IG values suggests the formation of high-quality three-dimensional graphitic carbon within the Al@C nanocatalyst. This three-dimensional graphitic carbon structure is indicative of well-ordered carbon arrangements and suggests promising catalytic properties for the nanocatalyst in various applications[153].

2.3.5. Thermogravimetric Analysis (TGA).

Thermogravimetric analysis (TGA) was conducted within a temperature range of 25 to 1000 °C to assess the thermal stability of the Al@C nanocatalyst. The TGA results, as depicted in Figure. 2.7, indicates a slight weight loss at approximately 100 °C, which can be caused by the desorption of absorbed water molecules. Subsequently, the nanocatalyst exhibits remarkable stability until it reaches 600 °C, at which point a noticeable weight loss is observed. This decrease in weight can be correlated to the loss of the solid support material leaving behind a weigh mass value close to the 14% that could be attributed to the presence of the metal and metal oxide nanoparticles. The TGA analysis underscores the thermal robustness of the Al@C nanocatalyst, indicating its suitability for various high-temperature catalytic applications.

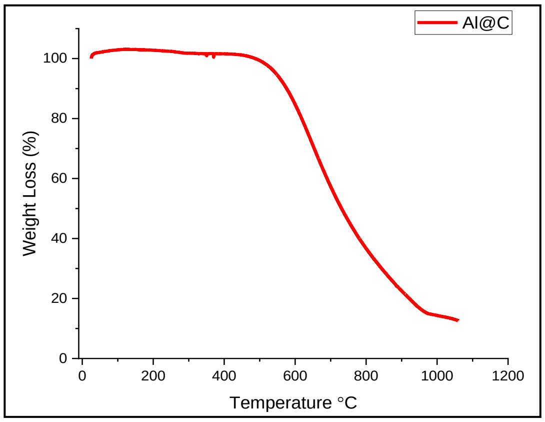

Figure 2.7: TGA curves of Al@C nanocatalyst.

2.3.6. FT-IR Analysis.

Fourier-transform infrared spectroscopy (FTIR) analysis was performed to clarify the functional groups present in both the Al BDC MOF precursor and the derived Al@C nanocatalyst. The outcomes are shown in Figure. 2.8. In the Al BDC MOF sample, distinctive broad peaks are observed at 1419 cm^{-1} and 1597 cm^{-1}, corresponding to the symmetric and asymmetric vibrations of (–COO-) groups, respectively[154]. These peaks are indicative of the presence of dicarboxylate linkers in the MOF material. Notably, the broad signal at 3440 cm^{-1}, typically associated with O-H stretching vibrations in adsorbed water molecules, is absent in this case, affirming the dryness of the sample[155].

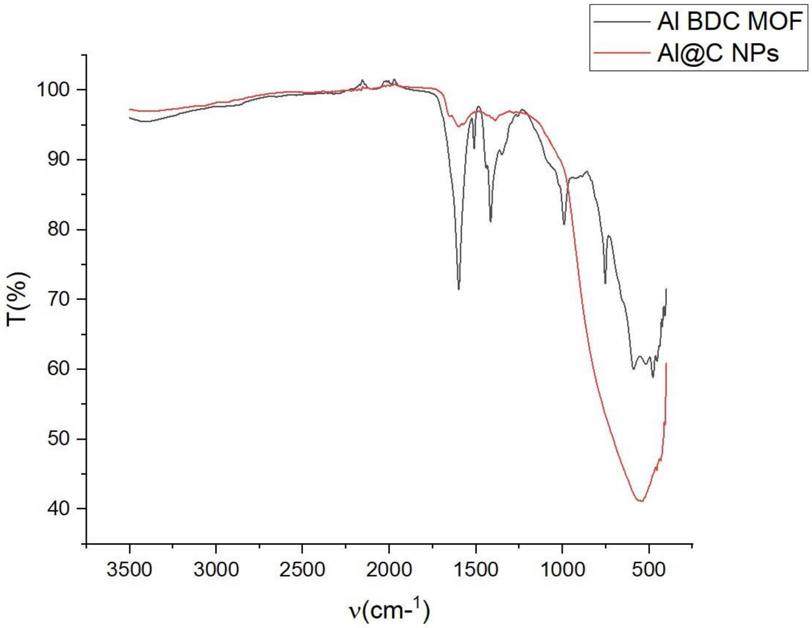

Figure 2.8: FT-IR spectra of Al BDC MOF and Al@C nanocatalyst.

In contrast, the FTIR spectrum of the Al@C nanocatalyst exhibits an absence of characteristic peaks present in the Al BDC MOF sample. This absence indicates that the Al BDC MOF precursor was completely decomposed during the carbonization process to form the Al@C nanocatalyst. Also we have the appearance of new signals close to 1500 cm^{-1} evidencing the presence of C=C and C-C starching vibrations, main component of the porous carbon solid support and finally the signal around 500 cm^{-1} corresponding to the formation of Al-C vibration. The FTIR analysis confirms the transformation of the MOF precursor into the carbon-based nanocatalyst, emphasizing the structural changes that occur during the synthesis process.

2.3.7. Catalytic Reduction of 4-NP, MO, and MB over Al@C nanocatalyst.

The catalytic performance of the synthesized Al@C nanocomposite was evaluated through the reduction reactions of three distinct organic pollutants: 4-Nitrophenol (4NP), Methyl orange (MO), and Methylene Blue (MB). These reduction reactions employed NaBH4 as the reducing agent in the presence of the Al@C nanocatalyst. Scheme 2.1 depicts the catalytic reduction reactions.

UV-Vis absorption experiments conducted over time for the reduction reactions of 4-NP, MO, and MB are displayed in Figure 2.9 (a-c), respectively. This research was carried out through an examination of the catalytic reduction of 4-NP, MB and MO using the Al@C nanocatalyst. The reduction of 4-NP to 4-AP (4-Aminophenol) is a widely used model reaction in catalytic studies, and it provides a means to assess catalytic performance. The 4-NP reduction reaction, which can be accurately followed through UV-Vis spectroscopy, exhibited distinct color changes during the course of the reaction. At first, the solution containing 4-NP exhibited a light-yellow hue; however, upon the addition of the Al@C nanocatalyst, it turned deep yellow. Subsequently, within just 1 minute of introducing NaBH4, the solution's color transitioned to colorless, indicating the formation of 4-AP. Real-time monitoring of the reaction progress was performed using UV-Vis spectroscopy, and the results are presented in Figure 2.9a. As observed in the figure, the reduction of 4-NP started right after the addition of NaBH4 and the nanocatalyst, and UV-Vis spectra were collected at 10-second intervals.

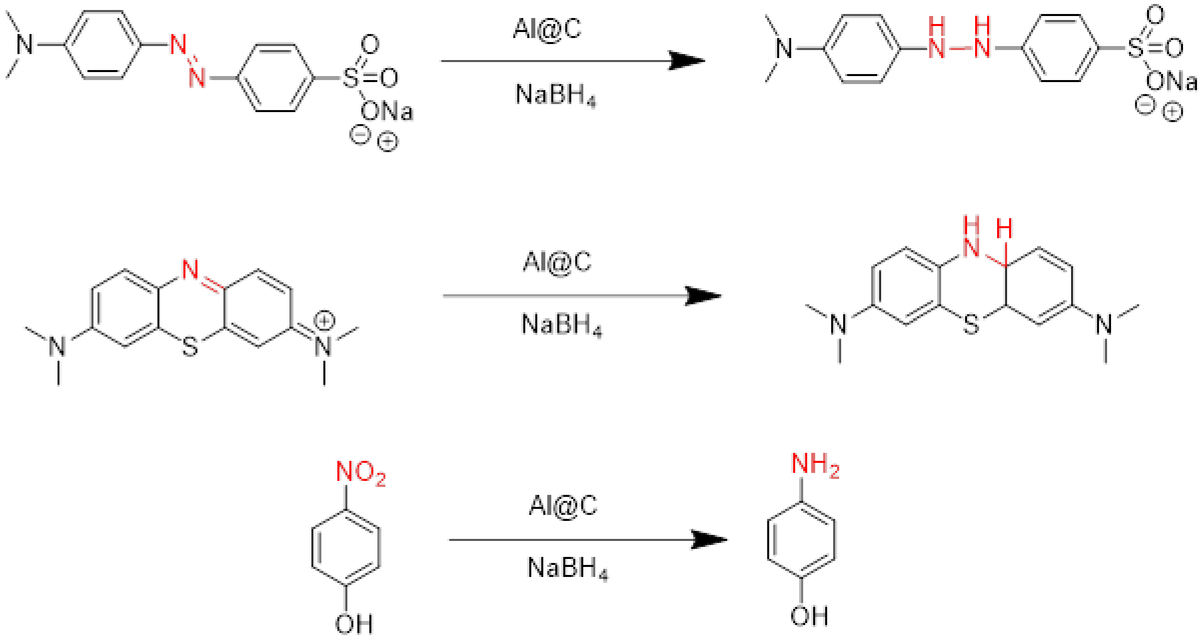

Scheme 2.1: Catalytic reduction of MO, MB and 4-NP over Al@C nanocatalyst in presence of NaBH4.

The reduction of 4-NP was evident from the rapid decrease in intensity of the 4-NP peak at 400 nm in the UV-Vis spectra. No additional peaks were observed in the spectra, indicating no side reactions occurred during the catalytic reduction of 4-NP. The disappearance of the adsorption peak for 4-NP and the change in solution color from dark yellow to colorless evidence the successful completion of the 4-NP catalytic reduction. Similarly, in the cases of MO and MB pollutants, it was clear that their reduction reactions occurred almost instantaneously after the addition of NaBH4 to the pollutant solutions containing the Al@C nanocatalyst, as shown in Figure 2.9 (b-c).

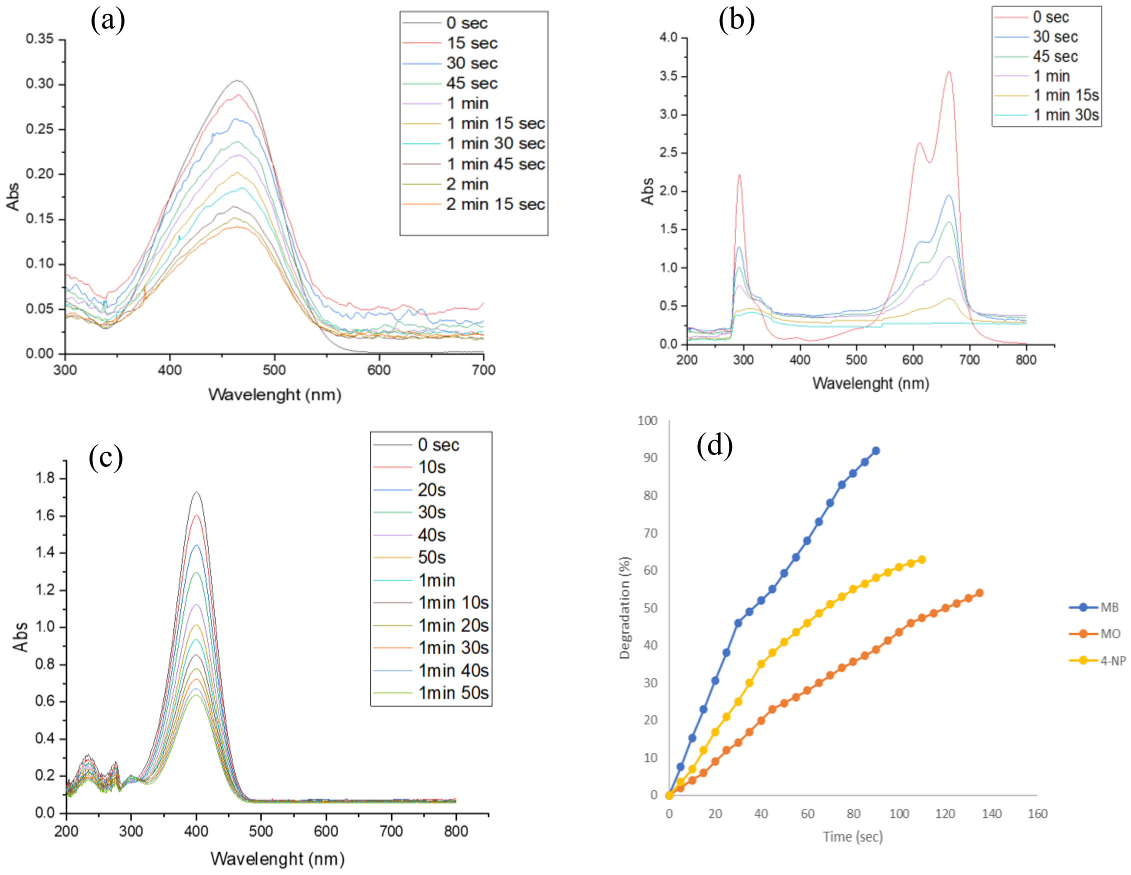

Figure 2.9: Time dependent UV-Vis spectra of (a) 4NP; (b) MB; (c) MO; and (d) degradation in time for the catalytic reduction of the pollutants in presence of the nanocatalyst.

The reaction times for both MO and MB were similar to the previously mentioned 4-NP, with complete discoloration of the orange and blue solutions occurring after 1 minute in contact with NaBH4 and the Al@C nanocatalyst. These results suggest that the newly created nanocatalyst has the potential to break down the chromophore group or N=N double bond found in MO and MB, resulting in the discoloration of the solutions. The absorption maxima were observed at 465 nm and 660 nm for MO and MB, and changes in absorbance over time were monitored during the catalytic experiments based on these values.

The reduction products resulting from each experimental scenario were meticulously analyzed utilizing mass spectrometry to elucidate the molecular fragments present subsequent to the reduction reaction as shown in Fig 2.10. Through comprehensive examination of the mass spectrometry data, a notable finding emerged: the presence of a continuous reduction process instigated by the addition of NaBH4 in conjunction with the catalyst. While the initial direct reduction product was readily identified, further scrutiny of the spectra revealed the presence of additional reduction products, indicative of ongoing reactions occurring within the system.

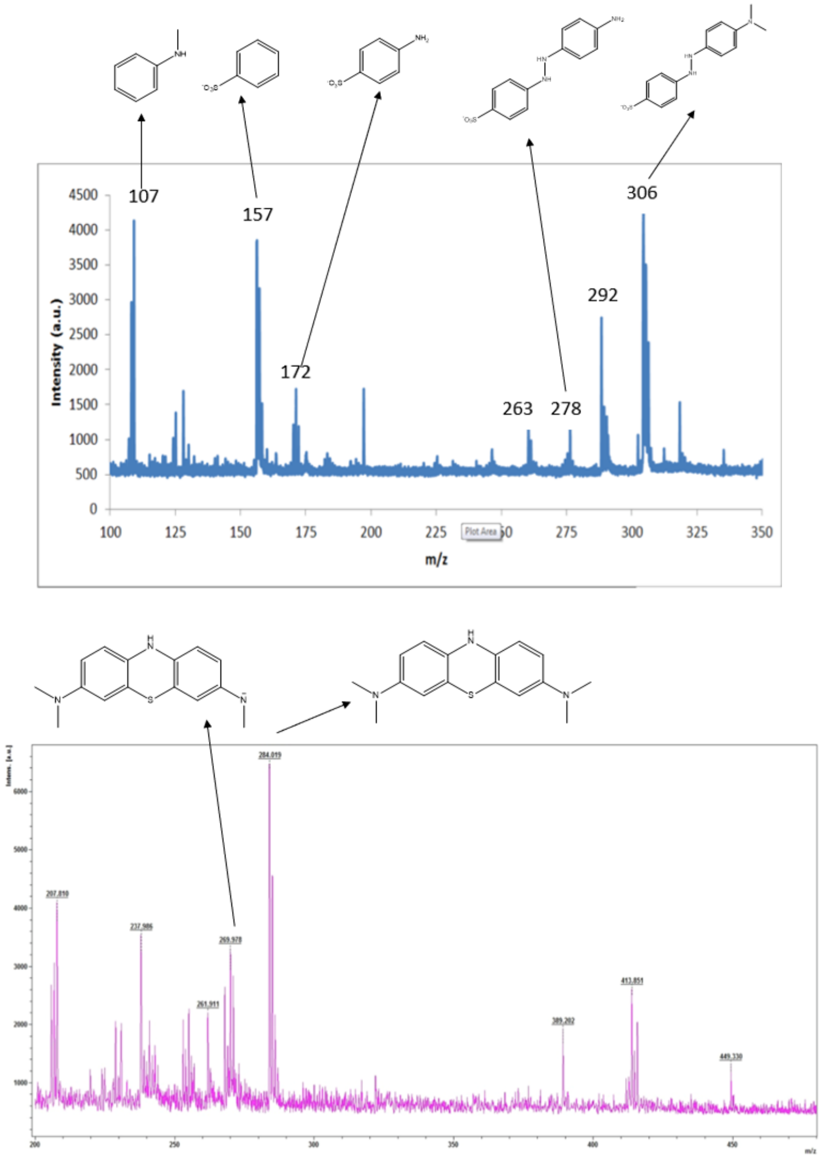

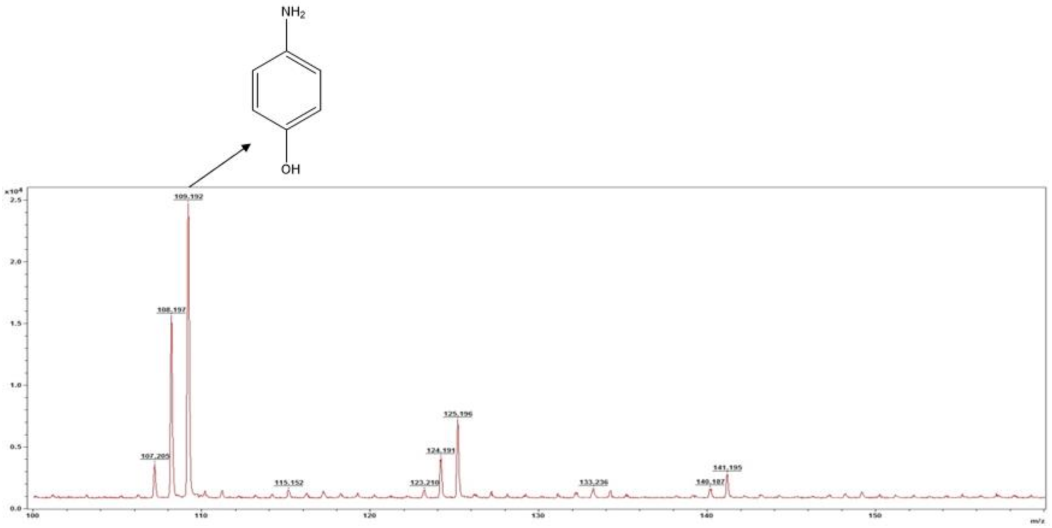

Figure 2.10: Mass Spec of the reduction products for a) Methyl Orange (MO), b) Methylene Blue (MB) and 4-Nitrophenol (4-NP)

This multifaceted observation provided compelling evidence supporting the catalytic activity of our nanocatalyst. Specifically, the ability to facilitate the reduction of organic compounds such as MO (methyl orange), MB (methylene blue), and 4-NP (4-nitrophenol) was demonstrated in the presence of a mild reductive agent like NaBH4. Importantly, the detection of successive reduction products beyond the primary reduction product underscored the robust and continuous nature of the reduction process catalyzed by our nanocatalyst, thus affirming its potential utility in diverse reduction reactions.

Additionally, an analysis of the catalytic reduction reaction kinetics was conducted to obtain further insights into the performance of the freshly synthesized Al@C nanocatalyst. The results are presented in Figure 2.9d and Table 2.1. Within the scope of these examined catalytic reduction reactions, the NaBH4 concentration was higher than that of the pollutants and remained relatively constant over the reaction time. Hence, the apparent rate constant in these reactions was determined using the pseudo-first-order kinetic model, as described by the following equation:

$$\ln(Ct/C0) = -kt \tag{2.3}$$

The apparent rate constant (k) was calculated using the concentrations of the pollutant solution at the initial (C_0) and current (C_t) times and the time (t). The determined rate constants for the catalytic reduction of 4-NP, MO, and MB were notably high, with values of 0.00947 s^{-1}, 0.00587 s^{-1}, and 0.02696 s^{-1}, respectively. These values surpass those reported for many other catalysts in the literature[156].

Table 2.1: Kinetics of catalytic reduction of 4-NP, MO and MB by Al@C nanocatalyst.

Catalyst	*Pollutants*	*catalyst*	*Reaction time*	*Rate constant*
Al@C	4-NP	1mg	150s	0.00947 s^{-1}
	MO	1mg	120s	0.00587 s^{-1}
	MB	1mg	90s	0.02696 s^{-1}

The rate constant values obtained in our study are notably higher than those reported for many other previously studied catalysts[157],[158],[159],[160],[161]. This observation underscores the highly efficient catalytic nature of the developed Al@C nanocatalyst, suggesting its potential for various practical applications in pollutant reduction and remediation.

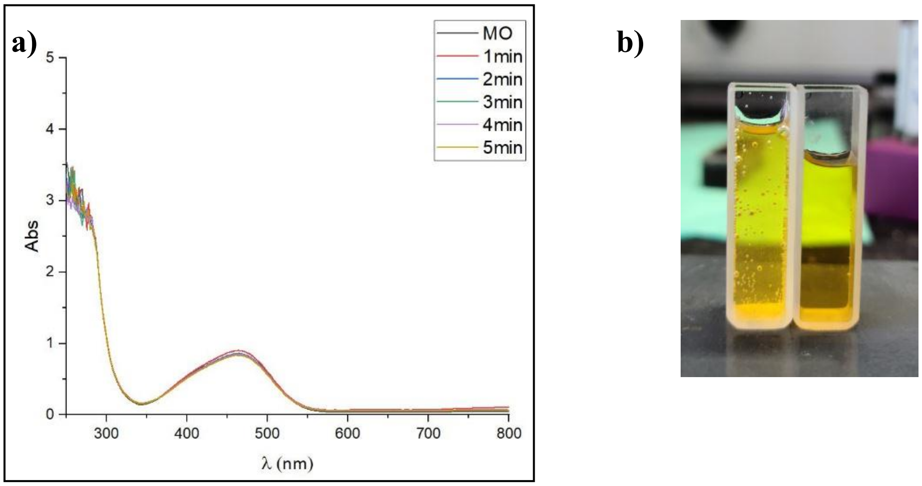

Figure 2.11: Control experiment adding $NaBH_4$ without nanocatalyst (a) time dependent UV-Vis spectra and (b) color comparison MO and MO+$NaBH_4$.

As part of this study, we conducted the reduction reactions of 4-NP, MO, and MB using NaBH4 alone, serving as a control experiment, without the involvement of any nanocatalyst. It is evident, as shown in Figure 2.11 (a-b), that NaBH4 alone has no significant effect on the catalytic reduction of all the studied pollutants, as there were no observable changes in the color of the samples or degradation, as evidenced by the absorbance values in the UV-Vis spectra. Additionally, the pollutants were also treated with the catalyst alone to assess any catalytic activity or degradation in the absence of the reducing agent. Similar to the previous control experiment, no significant changes were detected in the samples, and there were no appreciable alterations in the absorbance values in the UV-Vis spectra. A comparison of various nanocatalysts used for the reduction of 4-NP, MO, and MB is summarized in Table 2. Upon reviewing Table 2.2. Upon comparison, it becomes clear that our synthesized Al@C nanocatalyst outperforms previously reported nanocatalysts in the catalytic reduction of 4-NP, MO, and MB. Many of the other nanocatalysts rely on precious noble metals, making them costly, or they necessitate more time to complete the reduction reactions. Additionally, our reduction reaction conditions are remarkably convenient, straightforward, and exceptionally fast, resulting in high percentage yields.

Table 2.2: Comparison of the catalytic performance of different nanocatalysts for the catalytic reduction of 4-NP, MO and MB with $NaBH_4$.

Catalyst	**Pollutants**	**$k(s^{-1})$**	**Time**	**Reference**
Au@C particles	4-NP	$0.6x10^{-3}$	8 min	73
Pt/NPC-900	4-NP	$1.1x10^{-2}$	6 min	74
Ni-NPC-900	4-NP	$1.0x10^{-2}$	6 min	74
Fe_3O_4@SiO_2-Ag	4-NP	$7.67x10^{-3}$	8 min	75
Ni NPs	4-NP	$2.7x10^{-3}$	10 min	76
Cu@SBA-15	4-NP	$1.73x10^{-2}$	4 min	77
Ni-RGO hybrids	4-NP	$1.8x10^{-3}$	8 min	72
Al@C	**4-NP**	**$9.47x10^{-3}$**	**3 min**	**Present Study**
Fe_3Pt-Ag	MO	$7.2x10^{-2}$	18 min	78
NiGCN	MO	$1.1x10^{-2}$	4 min	79
Cu NRds	MO	$5.6x10^{-2}$	1 min 20 s	80
Cu NPs	MO	$3.2x10^{-2}$	2 min	87
Cu@SBA-15	MO	$1.53x10^{-2}$	5 min	77
Al@C	**MO**	**$5.87x10^{-3}$**	**3 min**	**Present Study**
Biosynthesized Au NPs	MB	$2.19x10^{-3}$	20 min	81
Biosynthesized Ag NPs	MB	$2.5x10^{-3}$	20 min	81
Cu@SBA-15	MB	$8.5x10^{-3}$	8 min	77
NiNTAs	MB	$3.7x10^{-4}$	1 min	82
Ni/CPM-1	MB	$9.51x10^{-3}$	13 min	83
Al@C	**MB**	**$2.69x10^{-2}$**	**1 min 30 s**	**Present Study**

2.4. Conclusions

In this research endeavor, we have successfully devised a straightforward and eco-friendly methodology for the synthesis of the Al@C nanocatalyst. This process involved subjecting the Al BDC MOF precursor to annealing at a temperature of 600°C under an argon atmosphere. A comprehensive analysis using X-ray diffraction (XRD) confirmed the transformation of characteristic peaks associated with the Al BDC MOF into those indicative of the Al@C nanocatalyst.

Further investigations of the synthesized materials' morphology were carried out through scanning electron microscopy (SEM) and transmission electron microscopy (TEM). These analyses revealed the formation of nanoscale metallic aluminum (Al) and aluminum oxide (Al2O3) particles distributed over a porous carbon matrix. Importantly, the nanoparticles exhibited a high degree of dispersion with minimal agglomeration, a critical characteristic for catalytic applications. Additionally, these nanoparticles were either encapsulated within the porous carbon framework or trapped on its surface. To analyze the chemical composition of the Al@C nanocatalyst, energy-dispersive X-ray spectroscopy (EDS) elemental analysis was performed. This analysis demonstrated the presence of only carbon (C), oxygen (O), and aluminum (Al), reinforcing the purity of the synthesized material. Furthermore, EDS elemental mapping confirmed the exclusive presence of these elements within the sample.

The catalytic performance of the developed Al@C nanocatalyst was evaluated through its application in the reduction of three model organic compounds: 4-nitrophenol (4-NP), methylene blue (MB), and methyl orange (MO), utilizing sodium borohydride (NaBH4) as the reducing agent. Remarkably, the Al@C nanocatalyst proved highly effective in mediating these reduction reactions, leading to the rapid conversion of 4-NP, MO, and MB into their respective organic products in less than 2 minutes. This underscores the exceptional catalytic activity of the synthesized Al@C nanocatalyst.

In conclusion, this study has introduced a straightforward and eco-friendly method for the synthesis of the Al@C nanocatalyst, showcasing its remarkable efficacy in catalytic applications, especially in the decomposition of diverse organic contaminants. This method represents a promising avenue for addressing environmental challenges related to the removal of organic contaminants from aqueous solutions.

Chapter 3: Catalytic degradation of Methyl Orange and Methylene Blue performed by Al-Fe@C bimetallic nano-system.

3.1. Introduction

Nanocatalysts have gained substantial attention as a pivotal area of research due to their numerous advantages in catalytic processes. These advantages primarily stem from the nanoscale properties of these materials. One of the most significant benefits is the substantially increased surface area of nanocatalysts compared to their bulk counterparts. This larger surface area offers a greater number of active sites for catalytic reactions, resulting in heightened efficiency and reactivity. Additionally, nanocatalysts often exhibit unique electronic and structural properties that increase their activity as a catalyst. This improved reactivity facilitates faster reaction kinetics and lowers the activation energy required for chemical transformations.

Another advantage of nanocatalysts is their resource efficiency. They can reduce the usage of precious and expensive metals, such as platinum and palladium, which are commonly employed in catalysis. This is achieved by maximizing the exposure of active sites and minimizing the use of costly materials. Moreover, nanocatalysts offer tailored properties, allowing researchers to fine-tune their size, shape, composition, and surface chemistry. This tunability enables the design of catalysts optimized for specific reactions, further enhancing their performance. Furthermore, nanocatalysts are versatile and can be applied across a wide range of catalytic processes, spanning environmental remediation and energy production to pharmaceutical synthesis and materials fabrication. To address the cost and resource limitations associated with noble metals like platinum and palladium, scientists have explored various strategies. These include anchoring noble metal nanoparticles onto solid supports, such as carbon nanotubes or porous oxides, to enhance their stability and reduce overall metal usage. The use of porous materials, such as metal-organic frameworks (MOFs) and zeolites, as catalyst supports offers high surface areas and tunable pore structures, enabling efficient reactant diffusion and catalytic activity. Core@shell nanoparticles, comprising a core made of a less expensive material encased by a shell of a noble metal, maintain catalytic performance while conserving costly metals. Additionally, bimetallic nanoparticles, which combine two different metals in a single nanoparticle, often with complementary catalytic properties, can lead to synergistic effects, enhancing catalytic activity and selectivity. Nano-catalysis presents a promising avenue for advancing catalytic processes by harnessing the unique properties of nanoparticles. Researchers continue to explore innovative approaches to develop efficient and cost-effective nanocatalysts capable of addressing critical challenges across various fields, from green energy production to environmental protection and beyond.

Over the past decade, nanotechnology has emerged as a transformative field with the potential to revolutionize various industries by altering the structure and properties of materials at the nanoscale. This technology holds immense promise for society, offering opportunities for advanced materials, enhanced product functionalities, and novel applications. However, as nanomaterials become increasingly integrated into products and manufacturing processes, concerns about potential health and environmental impacts have arisen. According to the U.S. Bureau of Labor Statistics and the National Institute for Occupational Safety and Health (NIOSH), by the year 2000, approximately 2.0 million individuals were employed in occupations involving nanomaterial products[162]. These workers may face exposure to nanoparticles during the production of various goods. Additionally, emissions and liquid waste from industries utilizing nanomaterials may contain nanoparticles that can disperse into the air and water, potentially affecting the general population. This raises concerns about a global health hazard.

Nanoparticles are particles characterized by their size, with dimensions below 100 nanometers in at least one axis. They can originate from diverse sources, including natural processes and human activities. Epidemiological studies conducted on ultrafine particles, which fall within the same size range as nanoparticles, have demonstrated acute and chronic health effects associated with exposure to such particles. While acute toxicity studies involving animals have shown immediate adverse effects on various organs, research into chronic effects remains limited[163]. The limited toxicological studies available suggest that, for the same mass of material, nanoparticles within the nanometric size range are generally more toxic than their micro-metric counterparts[164],[165]. This underscores the importance of continued research to better understand the potential risks associated with nanoparticles and to develop strategies for their safe and responsible use in nanotechnology and industrial applications.

The toxicity of nanoparticles is influenced by several key factors, including their larger surface area and higher number concentration[166],[167]. These factors play significant roles in enhancing the potential harm associated with nanoparticles. The increased surface area results in greater surface reactivity, which, in turn, can influence the toxicity of nanoparticles due to the presence of a larger number of molecules on their surface[168],[169]. Moreover, the toxicity of nanoparticles can also be influenced by various physicochemical factors. These factors include the crystal structure of the nanoparticles, their potential for aggregation, and the presence of surface coatings or modifications. Each of these characteristics can impact how nanoparticles interact with biological systems and the environment, potentially affecting their toxicity[170].

Understanding the interplay of these factors is crucial for assessing and mitigating the potential risks associated with nanoparticles, especially in applications where they are widely used, such as nanotechnology and industrial processes. Research in this area continues to evolve to ensure the safe and responsible utilization of nanomaterials in various fields.

The issue of nanoparticle toxicity has garnered considerable focus because of its possible consequences on human well-being and the ecosystem[171]. The presence of nanoparticles in various industrial processes and consumer products has raised concerns about exposure and contamination of natural resources, including water supplies[172],[173],[174]. Unlike organic molecules, nanoparticles do not readily degrade on their own or with the assistance of photocatalysts, making their removal from water sources challenging. To address this problem, there has been a concerted effort to develop materials capable of capturing and encapsulating nanoparticles efficiently.

In this context, the development of porous carbon materials with the ability to trap and immobilize nanoparticles within their framework has emerged as a promising solution. These materials can be used in water treatment processes and easily removed through filtration techniques. However, the potential applications of trapped nanoparticles go beyond mere removal. Researchers have explored the idea of utilizing these trapped nanoparticles for beneficial purposes, such as catalytic reactions.

Magnetic nanoparticles are crucial in various fields due to their unique magnetic properties, particularly their ability to respond to external magnetic fields and their ease of recovery. These properties make magnetic nanoparticles valuable in numerous applications, especially in separation processes and environmental remediation. One key aspect of magnetic nanoparticles is their responsiveness to external magnetic fields. When placed in a magnetic field, these nanoparticles become magnetized, allowing them to be manipulated and controlled. This property is particularly useful in magnetic separation processes, where magnetic nanoparticles can be selectively separated from a mixture using a magnet. This ability enables efficient purification and extraction processes in industries such as pharmaceuticals, biotechnology, and wastewater treatment. Moreover, the ease of recovery associated with magnetic nanoparticles is highly advantageous. Once the desired process is complete, the magnetic field is simply removed, causing the nanoparticles to return to their dispersed state. This allows for straightforward recovery and reuse of the nanoparticles, reducing waste and improving process efficiency. Additionally, magnetic nanoparticles can be functionalized with specific ligands or coatings to enhance their performance and selectivity in various applications. Overall, the magnetic properties of nanoparticles play a crucial role in their utility and versatility. Their ability to respond to external magnetic fields and their ease of recovery make them invaluable in a wide range of fields, including biomedicine, environmental science, and materials engineering.

In this study, we propose a straightforward and environmentally friendly approach for synthesizing porous carbon-encased bimetallic Al-Fe nanoparticles with catalytic properties. We assessed the catalytic performance of these nanoparticles through two distinct catalytic reactions. These reactions involved the catalytic process of reducing MB and MO organic dyes. Additionally, to assess the recyclability and reusability of the synthesized nanomaterials, a recovery study was conducted. The results revealed that there was a decrease of less than 10% in the catalytic activity of the nanocatalyst after 10 cycles of experimentation under identical conditions.

3.2. Materials and Methods.

3.2.1. Chemicals and Reagents.

All the chemicals utilized in this study were used as provided, requiring no supplementary purification. The following chemicals were utilized in the preparation of the bimetallic Al-Fe@C nanoparticles. Aluminum nitrate nonahydrate ($Al(NO_3)_3.9H_2O$) (ACS reagent, ≥98.0%), Iron nitrate nonahydrate ($Fe(NO_3)_3.9H_2O$) (≥99.95% traces metals basis), sodium hydroxide (NaOH ≥ 98%), and Urea (NH_2CONH_2) (ACS reagent, 99.0-100.5%), ethanol (≥99.5%), Methyl orange (MO) (dye\ content > 98.0%) and Methylene Blue (MB) (dye\ content > 98.0%) were purchased from Sigma-Aldrich. Deionized (DI) water (>18.20 MI cm resistivity) was used from the Milli-Q® instrument (Millipore Corporation).

3.2.2. Synthesis of Al-Fe@C nanoparticles.

A straightforward and environmentally friendly synthesis method was employed to obtain the bimetallic Al-Fe@C nanoparticles. For this typical synthesis, 1.5 g of Al(NO3)3·9H2O and 1.5 g of Fe(NO3)3·9H2O were added into a 200 mL beaker and dissolved in 70 mL of deionized water. Subsequently, 3 g of urea was introduced into the solution, followed by 10 minutes of ultrasonication to ensure complete dissolution of the solid materials. The transparent solution was left to stir at room temperature for 24 hours. Afterward, the beaker with the solution was placed in a vacuum oven and dried at 100 °C for 12 hours, resulting in an orange-brown colored solid. The solid was then carbonized in a furnace at 600 °C under a continuous flow of ultrapure argon for 3 hours, with a heating rate of 5 °C/min. Once cooled to room temperature, the black powder obtained was collected and stored in a 20 mL glass vial for further use in subsequent experiments.

3.2.3. Characterization of the nanocatalyst.

The characterization of the synthesized nanocatalyst involved several analytical techniques. Powder X-ray diffraction (XRD) patterns were obtained using a Bruker D8 Discover X-ray Diffractometer. To study the morphologies, microstructures, and elemental compositions of the prepared nanocatalyst, both transmission electron microscopy (TEM, Model: Hitachi H-7650) and scanning electron microscopy (SEM, Model: Hitachi S-4800) equipped with energy-dispersive X-ray spectroscopy (EDS) instruments were utilized. Additionally, a UV–Vis spectrophotometer (Model: Agilent Cary 50 Conc) was employed for measuring the absorbance of various solutions.

3.2.4. Catalytic reduction of organic pollutant.

The catalytic reduction of the organic pollutants Methyl Orange (MO) and Methylene Blue (MB) was carried out in a quartz cuvette with a path length of 1.0 cm. In this reaction, 4 mL of a previously prepared 20 ppm methyl orange (MO) or methylene blue (MB) solution in each case was combined with 1 mg of Al-Fe@C nanocatalyst and 5 mg of $NaBH_4$ as reducing agent. The resulting solution, initially colored, turned transparent upon the addition of the reducing agent. The progress of the catalytic reduction of the pollutants was monitored using UV–visible spectroscopy at various time intervals within the range of 200 to 800 nm.

3.2.5. Recovery experiment.

Following the initial reduction experiment, once the resulting solution achieved complete transparency, the magnetic black powder (Al-Fe@C nanomaterial) was separated using an external magnet. Subsequently, it was thoroughly washed with water and reused to conduct a similar experiment as described in section 3.2.4 on the catalytic reduction of organic pollutants.

3.3. Results and Discussion.

The synthesis of bimetallic Al-Fe@C nanoparticles involved a two-step methodology. Firstly, a thorough mixture of metal ions derived from salt precursors and urea was performed. Subsequently, a high-temperature carbonization process was carried out. During the carbonization step, urea served as both the carbon source and the metallic ions acted as the source of metal components. This process ultimately resulted in the formation of Al and Fe nanoparticles encapsulated within a porous carbon framework.

The carbonization process served a dual purpose: it transformed urea into the porous carbon matrix while simultaneously reducing the metal ions into Al-Fe nanoparticles. This reduction process was facilitated by the generation of oxidative and reductive conditions that occurred in situ during carbonization. As a result of this templated carbonization process, we successfully generated a nanocomposite characterized by the uniform dispersion of clean-surfaced Al-Fe nanoparticles enclosed within a hierarchically porous carbon matrix.

3.3.1. Analysis of Crystalline Structure by XRD.

The crystalline structure of this nanomaterial was characterized using X-ray diffraction (XRD). The X-ray diffraction (XRD) spectrum of the Al-Fe@C nanocomposite, synthesized using urea as the carbon source, is shown in Figure 3.1. This spectrum exhibits distinct characteristic peaks located at approximately 2θ values of 30°, 36°, 58°, and 64°. These peaks closely match the indexed crystal planes associated with the cubic system of hercynite

(Al2FeO4), specifically with the crystallographic space group Fd-3m. The corresponding Miller indices (h, k, l) for these peaks correspond to (022), (113), (115), and (044) planes within the space lattice, respectively.

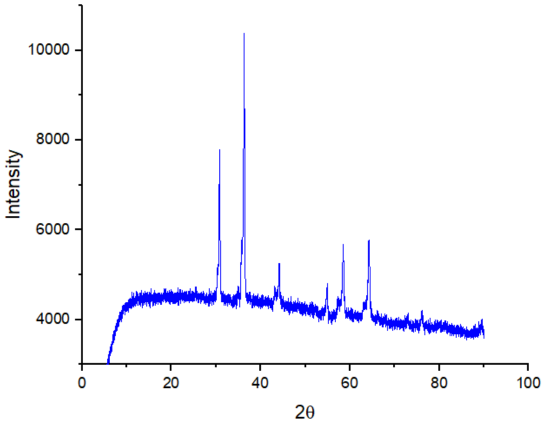

Figure 3.1: XRD pattern of Al-Fe@C nanocomposite

In addition to the prominent peaks corresponding to hercynite (Al2FeO4), smaller signals were also detected upon analyzing the spectrum in Figure 3.1. These smaller peaks are indicative of the presence of other crystal phases. Specifically, they correspond to the tetragonal iron (III) oxide, known as Gamma (Fe2O3), identified by reference code 98-017-2906, as well as the orthorhombic aluminum oxide (Al2O3), represented by reference code 98-016-1061. Overall, the XRD analysis provides strong evidence supporting the successful synthesis of bimetallic Al-Fe nanoparticles encapsulated within a porous carbon framework.

3.3.2. Morphological analysis by SEM and TEM.

SEM analysis of the synthesized Al-Fe@C nanocomposite, as shown in Figure 3.2, reveals several important morphological features. The carbon particles in which the Al-Fe nanoparticles are encapsulated appear to be in the micron-size particle range. Additionally, small pores can be observed on the surface of the carbon structure, which is characteristic of this type of porous carbon material.

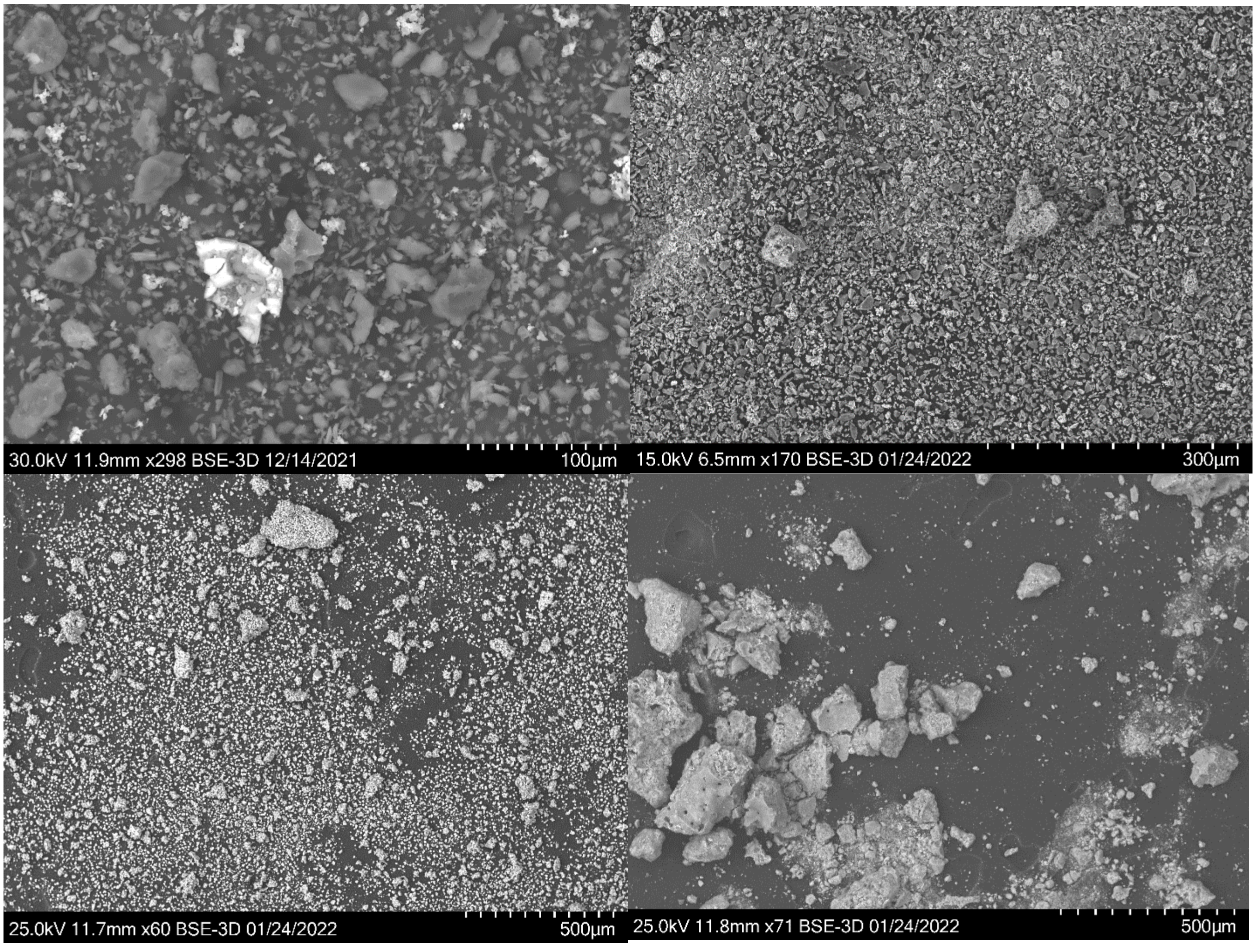

Figure 3.2: SEM images of Al-Fe@C nanocomposite

The TEM analysis of the Al-Fe@C nanocomposite, as depicted in Figure 3.3, provides valuable insights into its microstructure and morphology. The nanocomposite exhibits a spherical geometry with particle sizes ranging from 20 to 50 nm. Importantly, there is minimal agglomeration of particles, which can be attributed to the highly porous nature of the carbon material formed during the carbonization process.

Furthermore, the TEM images clearly reveal that all of the Al-Fe nanoparticles are encapsulated within the carbon framework. Notably, the use of a carbon grid for TEM measurements allows for a clear distinction between the grid's carbon and the carbon constituting the nanocomposite. This distinction demonstrates that none of the Al-Fe nanoparticles exist in isolation outside of the carbon matrix. This observation is significant as it confirms that all metallic nanoparticles are effectively trapped within the porous carbon framework, preventing their release into the surrounding environment.

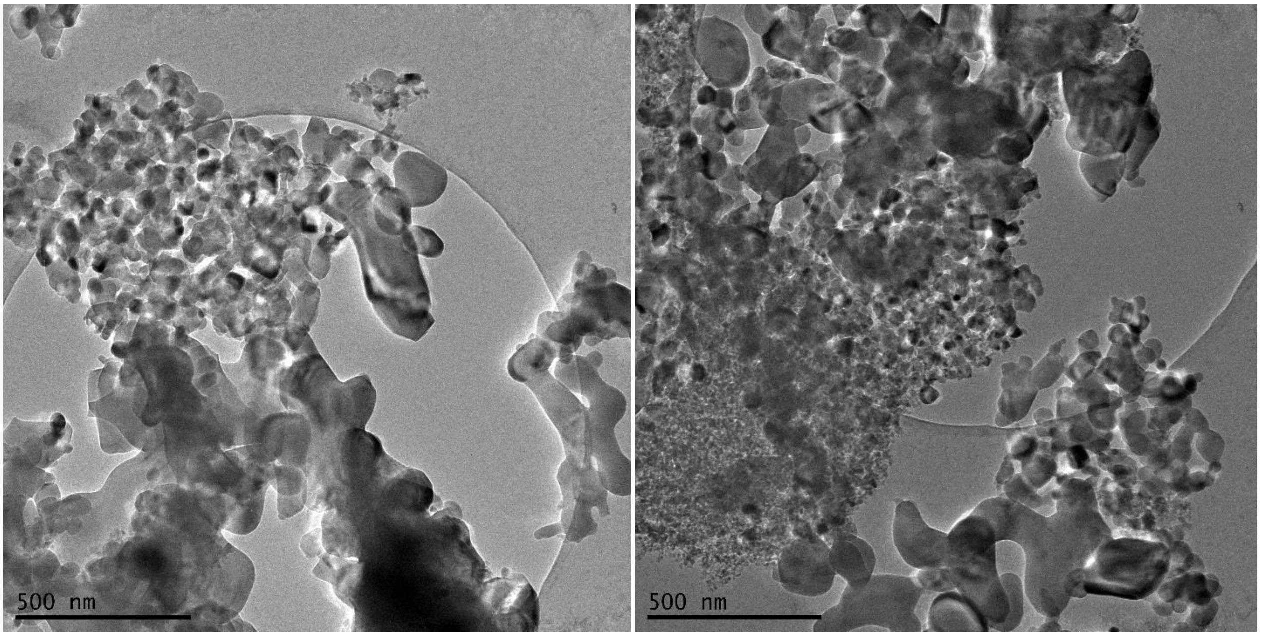

Figure 3.3: TEM images of Al-Fe@C nanocomposite.

3.3.3. Raman Analysis.

The Raman spectra of the as-synthesized nanoparticles are presented in Figure 3.4. In the spectra, two characteristic peaks were observed at approximately 1349 cm^-1 and 1576 cm^-1, corresponding to the D and G bands of the porous carbon matrix, respectively. These bands are significant in characterizing carbon-based materials.

The D band typically represents disordered sp3 carbon structures, while the G band reflects the presence of sp2 type graphitic carbon. The intensity ratio (ID/IG) of these two bands is often used to estimate the degree of graphitization and defect density in carbon-based materials. In the case of the Al-Fe@C nanomaterial, the calculated ID/IG value was found to be 0.71. This value suggests a certain degree of disorder in the carbon structure, which can be attributed to the carbonization process.

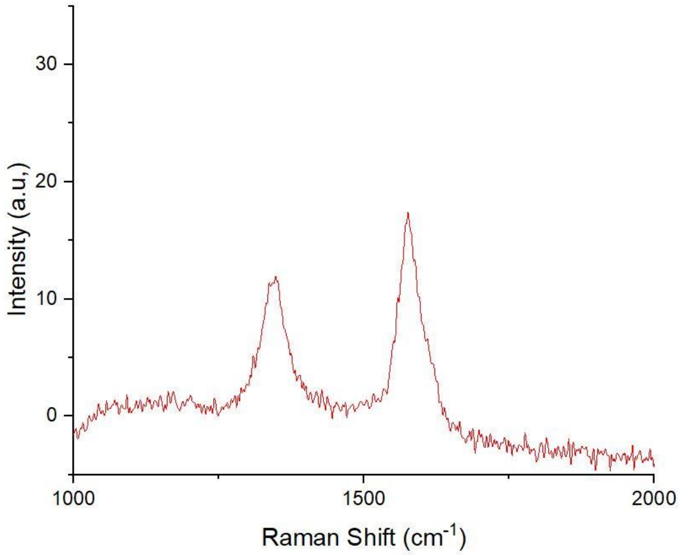

Figure 3.4: Raman spectra for Al-Fe@C nanocomposite.

During carbonization, urea serves as a carbon source, and simultaneously, the metal ions (iron and aluminum) are reduced. Iron can also act as a catalyst during this process, promoting the graphitization of the porous carbon matrix[175]. The presence of iron likely contributes to the observed Raman spectra and the calculated ID/IG ratio, indicating the formation of the porous carbon matrix with graphitic and disordered carbon structures.

3.3.4. EDS analysis and elemental color mapping.

Energy-dispersive X-ray spectroscopy (EDS) analysis, along with elemental mapping, was performed to confirm the elemental composition of the Al-Fe@C nanocomposite. The results are shown in Figure 3.5.

The EDS spectrum confirmed the presence of elements such as Al, Fe, O, and C in the bimetallic sample. This analysis provides further evidence of the successful synthesis of the Al-Fe@C nanocomposite. Elemental color mapping revealed the presence of three different types of particles within the sample: Al nanoparticles, Fe nanoparticles, and an alloy consisting of both Al and Fe nanoparticles (Al-Fe nanoparticles).

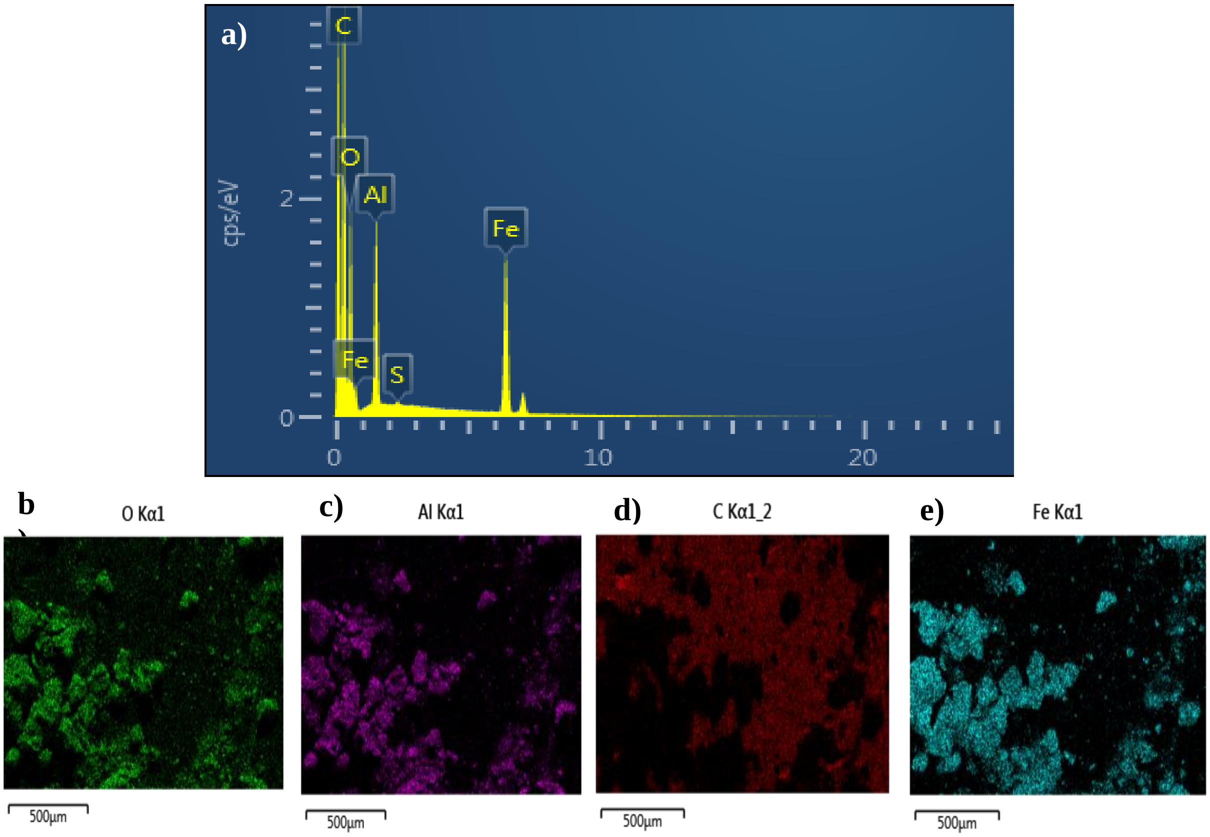

Figure 3.5: Energy dispersive X-ray spectroscopy (EDS) a) and elemental analysis graphs and b)-e) elemental color mapping from the Al-Fe@C nanocomposite.

These findings align with the information obtained from the XRD analysis, which also indicated the presence of these three different chemical environments. Carbon (C) was found to be the most abundant element in the nanocomposite, as all the metallic nanoparticles are encapsulated within the carbon framework generated during the carbonization process from the urea precursor. After the nanomaterial was washed with nitric acid, some iron was still detected in the sample. The acid washing step is known to effectively remove nanoparticles that were not fully encapsulated within the carbon matrix, leaving behind voids or holes.

3.3.5. Catalytic reduction of MO and MB carried by Al-Fe@C.

The catalytic reduction efficiency of the Al-Fe@C nanocomposite was evaluated using a solution of Methyl Orange (MO) and Methylene Blue (MB) as a model pollutant. In this unique catalytic system, we use sodium borohydride (NaBH4) as a reducing agent. The experimental procedure commenced by carefully mixing the MO or MB solution in each case with the black powder nanocatalyst of Al-Fe@C, then the addition of the $NaBH_4$ was done very carefully. Upon the addition of the reducing agent, small bubbles began to emerge within the darkened solution, signifying an intriguing chemical reaction. These bubbles were a clear indication that the nanocomposite was catalyzing the reduction of the organic pollutant, a process that led to the generation of hydrogen gas because of the use of the $NaBH_4$ as reducing agent. The interaction between the generated nanocatalyst, the reducing agent and the dyes molecules resulted in the degradation of the pollutant, transforming it into less harmful byproducts. Immediately, after the addition the sample was analyzed by UV-Vis to study the kinetic of the catalytic reaction.

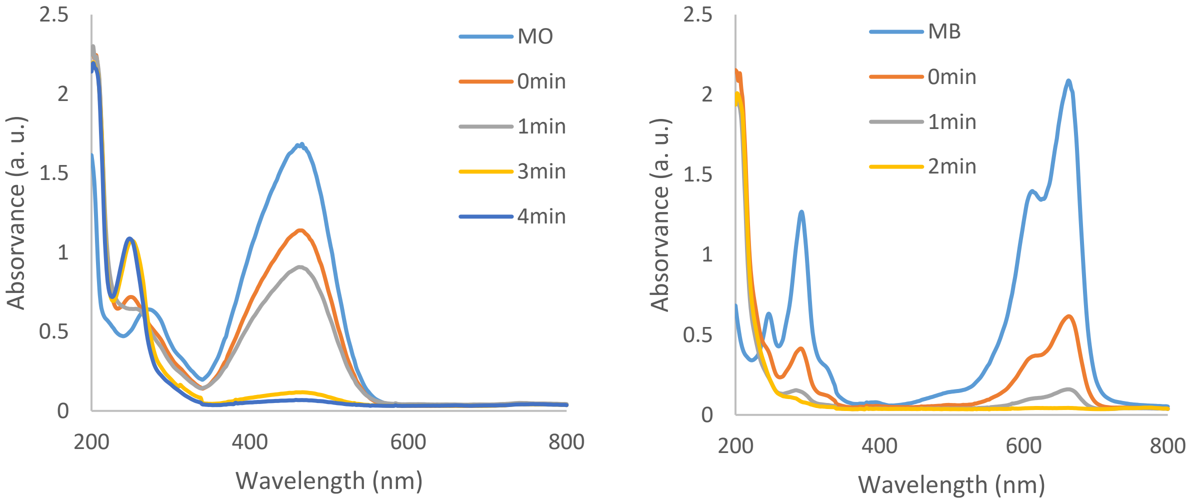

Figure 3.6: UV–Vis spectrum of catalytic degradation treatment of MO a) and MB b) carried by Al-Fe@C nanocomposite.

The UV-Vis absorbance spectra, as depicted in Figure 3.6, illustrates the catalytic reduction of MO and MB using the Al-Fe@C nanocomposite. Initially, a distinct MO signal at around 510 nm is observed. Within just 4 minutes of exposure to the nanocomposite, this MO signal vanishes completely, leaving a clear solution. In the case of the MB, the nanocatalyst present even faster degradation times, completely bleaching the colored solution in less than 2 minutes. This rapid transformation underscores the nanocomposite's remarkable catalytic efficiency in reducing MO and MB, emphasizing its potential for practical applications in pollutant degradation.

3.3.6. Recovery study of the Al-Fe-@C nanocomposite in MO and MB solutions.

To investigate the reusability properties of the synthesized nanocomposite, a recovery study was conducted. Leveraging the magnetic properties exhibited by the Al-Fe@C nanocatalyst, the black powder was recovered post the initial catalytic reduction process using an external magnet. Subsequently, the black powder was rinsed with water to eliminate any potential traces of the dye solution before being utilized in a new preparation of organic dye solution and NaBH4 mixture. Similar to the initial experiment, the solution of methyl orange (MO) started transitioning from orange to colorless, and methylene blue (MB) from blue to colorless after a few minutes. Employing the same methodology, the nanocatalyst was recovered and reused in subsequent experiments.

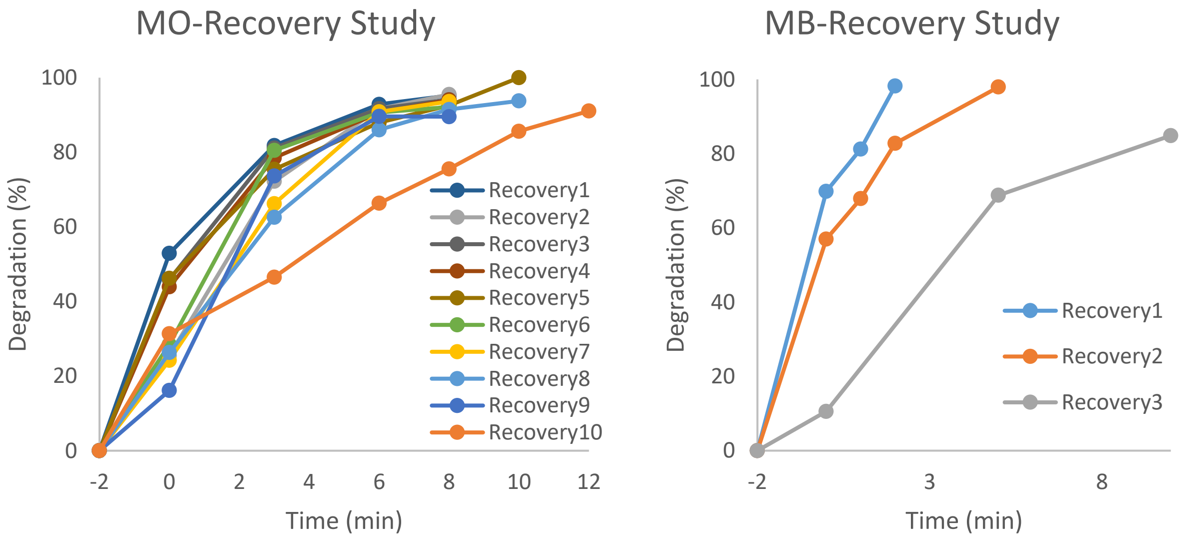

Figure 3.7: UV–Vis spectrum of recovery study of MO and MB catalytic degradation by Al-Fe@C nanocomposite.

Kinetic degradation in each experiment was analyzed via UV-Vis. the Figure 3.7 is revealing slight variations in both the percentage degradation and the time required to completely bleach the dye reaction with each recovery experiment. Notably, for the MO solution, the Al-Fe@C nanocatalyst demonstrated the ability to be reused up to 10 times, with less than a 20% decrease in initial activity. However, in the case of the MB solution, the percentage degradation was already nearing 80% after just three uses of the nanocomposite. These results underscore the successful reusability of the synthesized nanocomposite and its capacity to maintain high efficiency even after 10 cycles of degradation reaction. Furthermore, this highlights a significant economic advantage in the practical application of this nanocomposite for catalytic degradation in water contaminated by organic pollutants.

3.4. Conclusions

In this study, a novel and environmentally friendly method for creating a catalytic system has been developed to efficiently reduce organic pollutants, such as methyl orange (MO) and Methylene Blue (MB) assisted by the presence of $NaBH_4$ as reducing agent. The synthesis process involved the careful combination of two metal precursors with urea. This mixture was subjected to a controlled carbonization process in a furnace under an argon atmosphere at a precise temperature of 600 °C for a duration of three hours. During this carbonization step, two key transformations occurred simultaneously: the reduction of metal ions and the creation of a porous carbon framework. Significantly, this porous biocarbon encapsulated the metal nanoparticles, ensuring their stability and preventing their release into the environment.

Detailed characterization of the resulting nanocomposite was conducted using various techniques. X-ray diffraction (XRD) analysis provided insights into the crystalline structure of the material, revealing the presence of three distinct chemical environments within the sample: aluminum nanoparticles, iron nanoparticles, and an alloy formed from a combination of these two metals. These findings were further validated by energy-dispersive X-ray spectroscopy (EDS) and elemental color mapping, confirming the elemental composition of the nanocomposite, which consisted primarily of aluminum, iron, oxygen, and carbon. This composition was consistent with the synthesis process and the expected properties of the material. Morphological studies were performed using scanning electron microscopy (SEM) and transmission electron microscopy (TEM). These analyses revealed a highly dispersed distribution of metallic nanoparticles with minimal agglomeration. The nanoparticles were found to be uniformly distributed, both on the surface and inside the porous carbon framework. This morphology was critical for the material's catalytic properties.

Raman spectroscopy was employed to investigate the graphitic characteristics of carbon material. The analysis focused on two key bands, the D band (associated with disordered sp3 carbon) and the G band (reflecting sp2 type graphitic carbon). The intensity ratio (ID/IG) of these bands was calculated and found to be 0.71, indicating the presence of graphitic carbon in the material. This information suggested that the carbonization process was successful in creating a porous carbon framework with graphitic properties, further enhancing the material's catalytic potential.

The catalytic capabilities of the Al-Fe@C nanocomposite were evaluated with MO and MB solutions. Upon introducing the nanocomposite to a solution of MO in presence of $NaBH_4$, the initial-colored solution rapidly turned colorless, and bubbles started to appear, signifying the initiation of the catalytic process. After five minutes, the solution was completely clear and transparent. UV-Vis spectroscopy was used to study the kinetic degradation of each pollutants, exhibiting very good degradation times in each case, besides a recovery experiment was performed taking advantage of the magnetic properties of the synthesized nanoparticles, in which it could be appreciate than the nanocomposite is still presenting close to 80% of its initial catalytic activity even after 10 reaction cycles with MO solution.

In summary, this work has yielded a multifunctional nanocomposite, Al-Fe@C, with remarkable catalytic properties. The synthesis process was carefully designed to create a stable and efficient material with a well-defined structure. Its potential applications in catalysis and water remediation treatments make it a promising candidate for addressing environmental challenges.

Chapter 4: Saccharide-Derived Zinc Oxide Nanoparticles with High Photocatalytic Activity for Water Decontamination and Sanitation.

4.1. Introduction

Nanomaterials have unique physical[176], chemical[177], and biological properties[178] that make them valuable for addressing important scientific and engineering challenges today. They are being widely explored in various fields, such as chemical catalysis[179], optics[180], solar energy [181], energy storage[182], sensors[183], electronics[184], biological and medical applications[185], and environmental cleanup[186]. Among different nanomaterials, zinc oxide (ZnO) is particularly popular due to its specific characteristics like stability, abundance, safety, and affordability[187,188]. When it comes to breaking down organic pollutants in water, nanoscale ZnO particles (1–100 nm) are more effective as photocatalysts compared to larger particles. This is because they offer a larger surface area, higher surface energy, and an appropriate bandgap for separating electron-hole pairs, creating more active sites for pollutant degradation[189,190]. The degradation process occurs on the surface of zinc oxide nanoparticles through redox reactions triggered by electronic excitation between the valence and conduction bands[191]. Photocatalytic degradation is advantageous over conventional chemical methods as it doesn't require additional chemicals and doesn't lead to secondary pollution.

Various methods have been explored to create photocatalytic ZnO nanoparticles (NPs) with diverse shapes, including nanorods[192], nanotubes[193], nanobelts, nanowires[194], and nanomushrooms[195]. Common techniques for synthesizing ZnO NPs include ball milling[196], combustion synthesis[197,198], the sol-gel process[199], hydrothermal[200,201], and chemical vapor deposition[202,203]. However, many of these methods require expensive chemicals, intricate procedures, and extended processing times. There is a growing need for approaches that utilize readily available materials from biomass and employ simple, cost-effective techniques. Such methods could empower local manufacturing industries, particularly if the resulting products demonstrate strong catalytic activity.

Prior research has documented the calcination synthesis of metal oxide nanoparticles in citric acid[204]. This process entails heating a combination of the metal salt and the organic compound, which serves as a reducing agent, at elevated temperatures (500°C) in the presence of air. We have employed a comparable approach, utilizing zinc nitrate as the oxidizing agent and sawdust as the organic compound[205].

Contemporary dyes find widespread application in textile dyeing, cosmetics, pharmaceuticals, papermaking, food industries, and various other sectors[206,207]. However, many of these dyes and their breakdown byproducts pose a toxicity risk and can lead to serious health issues, including respiratory tract infections, vomiting, pain, hemorrhaging, and other diseases[208,209]. Moreover, most of these dyes resist degradation by natural elements such as light, heat, and biological agents[210,211]. Therefore, it is imperative to remove these dyes from water bodies before their discharge into the environment.

Methyl orange (MO) is a positively charged dye extensively utilized in food, cosmetic, textile, medicinal, and leather industries[212],[213]. However, the discharge of MO into aquatic ecosystems from various sources poses significant risks to living organisms, as this dye is genotoxic, carcinogenic, mutagenic, and resistant to degradation[214]. The persistent contamination of water bodies by MO poses a grave threat to environmental equilibrium, necessitating the development of strategies for its elimination[215,216]. Consequently, the degradation or removal of MO is crucial to mitigate its adverse impacts. Recent efforts have employed various physical, chemical, and biological methods to eliminate MO from water[217],[218]. Nonetheless, photocatalytic advanced oxidation processes (AOPs) have garnered considerable attention for effectively degrading organic pollutants in aqueous environments, offering advantages over alternative techniques such as adsorption, coagulation, precipitation, filtration, etc.[219]. Photocatalytic oxidative degradation is considered a good chemical tool for water remediation, without generating additional impurities. This process can degrade organic contaminants to mineralization, contrasting with other methods that merely displace pollution from one location to another[220].

In this chapter we present a straightforward approach for the synthesis of ZnO nanoparticles (NPs) through the combustion of a saccharide, such as glucose, fructose, dextrin, or starch, with zinc nitrate. Four distinct ZnO NP samples, namely Glucose-ZnO, Fructose-ZnO, Dextrin-ZnO, and Starch-ZnO, were successfully prepared. The photocatalytic efficacy of these ZnO NPs was assessed by their ability to degrade methyl orange (MO) in both deionized water (DIW) and simulated fresh drinking water (FDW) under UV light and sunlight exposure. Additionally, a fluorescence test was conducted to evaluate the generation of photocatalytic hydroxyl radicals (OH•) by the ZnO NPs[221].

4.2. Materials and Methods

4.2.1. Materials.

Glucose (C6H12O6, purity ≥ 99.5%), fructose (C6H12O6, purity ≥ 99%), dextrin ((C6H10O5)n, purity ≥ 99.5%), starch ((C6H10O5)n, purity ≥ 95%), zinc nitrate hexahydrate (Zn(NO3)2•6H2O, purity ≥ 98%), terephthalic acid (C8H6O4, purity = 98%), and sodium hydroxide (NaOH, purity ≥ 98%) were obtained from Sigma Aldrich. Methyl orange

(C14H15N3O3S, purity > 98.0%) was procured from TCI AMERICA. The salts utilized for preparing the simulated fresh drinking water matrices, including sodium bicarbonate (NaHCO3, purity 99.5–100.5%), calcium chloride dihydrate (CaCl2•2H2O, purity ≥ 99.5%), magnesium sulfate heptahydrate (MgSO4•7H2O, purity ≥ 98%), sodium silicate nonahydrate (Na2SiO3•9H2O, purity ≥ 98%), sodium nitrate (NaNO3, purity ≥ 99%), sodium fluoride (NaF, purity ≥ 99%), and sodium phosphate hydrate (NaH2PO4•H2O, purity ≥ 98%), were obtained from Sigma Aldrich.

The ZnO nanoparticles were obtained using an Analogue Hot Plate Stirrer (Fisher Scientific 11-600-49sh Isotemp, Hampton, NH, USA) as the heating source. The photoreactive reaction was analyzed in an ultraviolet box reactor (UVP Ultraviolet Cross-linker, Model CL-1000) equipped with UV-B fluorescent tube lamps was employed. The light intensity was measured using a digital Light Meter LX1330B, the sunlight experiment was performed under 100,000 lux for natural light on the reaction surface. Syringe filters with a pore size of 0.45 μm were purchased from VWR. Water (>18.20 MW•cm resistivity) was taken from the Milli-Q (Advantage A-10) water filter system. The simulated fresh drinking water (FDW) was prepared by dissolving specific amounts of NaHCO3 (252 mg/L), CaCl2•2H2O (147 mg/L), MgSO4•7H2O (124 mg/L), Na2SiO3•9H2O (95 mg/L), NaNO3 (12 mg/L), NaF (2.2 mg/L), and NaH2PO4•H2O (0.18 mg/L) in DIW, as previously described.

4.2.2. Chemical–Physical Characterization of ZnO NPs.

The (SEM) images and (EDX) experiments were conducted using the Hitachi SU3500 microscope, with carbon tape serving as the substrate for sample analysis. Transmission electron microscopy (TEM) experiments were carried out with a Hitachi H-7650 microscope operating at an acceleration voltage of 80 kV. X-ray diffraction (XRD) patterns of the ZnO nanoparticles were obtained using a Bruker D8 Discover X-ray diffractometer equipped with Cu Kα radiation (λ = 1.5418 Å), operating at 40 kV and 30 mA. The diffraction patterns were recorded at room temperature over a detector angle (2θ) range of 10 to 80 degrees. X-ray photoelectron spectroscopy (XPS) analysis was performed using Thermo Scientific™ K-alpha™ equipment with a monochromated Al Kα X-ray source. Survey spectra were acquired with a 130 eV pass energy, while high-resolution analyses for specific core levels were conducted with a 20 eV pass energy. An argon ions flood gun was employed to prevent surface charging, and all binding energies were referenced to carbon 1s at 284.8 eV. UV–visible spectroscopic analysis was carried out using the Agilent Cary 50 Conc UV–visible Spectrophotometer, with a standard quartz cuvette (10 mm path length) used as the sample holder. The determination of ZnO NP crystal size was performed through X-ray diffraction (XRD) data analysis in accordance with the Debye–Scherrer Equation (4.1).

$$d = k\lambda/\cos\theta \tag{4.1}$$

Initially, the XRD pattern underwent meticulous data processing involving nonlinear curve fitting, specifically Gaussian fitting, to extract the full width at half maximum (FWHM) values. Iterative procedures were applied to all data points until convergence was achieved. The obtained FWHM values, expressed in radians, along with the peak position information extracted from the XRD pattern, were subsequently utilized in the Scherrer equation for crystal size determination. The wavelength (λ) utilized by the XRD instrument was consistent with that of a copper source (Cu Kα) at 1.5406 Å. The Scherrer constant (k), applicable to spherical crystalline particles, was determined to be 0.9; where d represents the crystallite size and β is the full width at half maximum of the most intense (101) diffraction peak.

4.2.3. Obtaining the ZnO NPs.

Four distinct ZnO nanoparticle samples (Glucose-ZnO, Fructose-ZnO, Dextrin-ZnO, and Starch-ZnO) were synthesized following a similar experimental procedure. For instance, the synthesis of Glucose-ZnO is described as follows: Glucose (1200 mg, 3.51 mmol), Zn(NO3)2•6H2O (3569.88 mg, 12 mmol), and 2 mL of deionized water (DIW) were thoroughly mixed in a 150 mL glass beaker. The beaker was previously preheated in a hot plate to its maximum capacity of approximately 550°C, with the temperature on the bare surface of the hot plate reaching around 500°C, as measured with an IR temperature gun. Within a minute of heating or combustion, the mixture on the hot plate transformed into a thick/viscous solution and rapidly decomposed into a blackish-brown foam, accompanied by the emission of yellowish-brown gases. The hot plate containing the blackish-brown powder/foam was transferred to a well-ventilated fume hood due to the formation of NO2 and NOx gases resulting from the breakdown of the zinc nitrate salt. Subsequently, the foam transformed into a powder, which was slowly transferred onto the hot plate's surface with minimal spreading. During heating, the blackish powder transitioned into yellowish white ZnO nanoparticles. Upon cooling, the ZnO nanoparticle powder turned white. The white ZnO nanoparticles were collected in a vial using a spatula and utilized for further characterization and photocatalytic studies.

A control ZnO sample was synthesized using the same methodology with the exception of omitting any saccharides from the reaction mixture. Specifically, the ZnO-control was synthesized by combusting a mixture of 3569.88 mg (12 mmol) of Zn(NO3)2•6H2O and 2 mL of deionized water (DIW) without the addition of a saccharide at approximately 500°C in a 150 mL glass beaker on the same hot plate.

4.2.4. Methyl Orange (MO) Photodegradation Reaction Procedure.

The performance of the ZnO NPs in the photodegradation of methyl orange (MO) in deionized water (DIW) and simulated fresh drinking water was investigated under both UV and sunlight illumination conditions. A 5 ppm (mg/L) MO solution was prepared in a 250 mL glass beaker for the photodegradation test. To facilitate effective photodegradation under UV light, 30 mg of the ZnO NPs was added to a 30 mL MO (5 ppm) solution. The mixture underwent bath sonication for 15 minutes in the dark to ensure adsorption–desorption equilibrium between the MO dye and ZnO photocatalyst. Subsequently, the mixture (comprising the MO dye and ZnO photocatalyst) was exposed to UV light in a box reactor for 35 minutes. During the UV irradiation, a 1 mL sample was withdrawn every 5 minutes for analysis. A similar procedure was followed for the study under direct natural sunlight. In this case, 30 mg of the ZnO NPs was added to a 30 mL MO (5 ppm) solution, and the mixture underwent bath sonication for 5 minutes before being placed under natural sunlight for 18 minutes. Following exposure to sunlight, a 1 mL sample was collected every 3 minutes and filtered using a syringe filter (0.45 μm pore size) for UV-visible spectroscopic analysis. The degradation rate of MO was monitored by measuring the absorbance of MO at a wavelength of 464 nm.

4.2.5. Fluorescence Experiment for Detection of Hydroxyl Radicals.

A 5 × 10^-3 M stock solution of sodium terephthalate was prepared by combining terephthalic acid with a stoichiometric amount of sodium hydroxide in deionized water (DIW). From this stock solution, was taken 30 mL of the sodium terephthalate and transferred to a glass beaker and subjected to photoreaction with the ZnO NPs under UV light. During the photocatalysis process, approximately 1 mL of the sample was withdrawn at regular intervals of

5 minutes and filtered using syringe filters with a pore size of 0.45 µm. The fluorescence spectrum was recorded with an excitation wavelength of 315 nm. To qualitatively assess the concentration of hydroxyl radicals in the solution, the fluorescence emission intensity at 425 nm was measured.

4.3. Results and Discussion.

4.3.1. Synthesis of the ZnO NPs.

The ZnO NPs were synthesized by heating Zn(NO3)2•6H2O in the presence of different poly- or monosaccharides at approximately 500°C, as illustrated in Scheme 1. This process closely resembled our previously reported method using sucrose[222]. During the synthetic proccess, the poly- or monosaccharides actively engaged in the reaction alongside dioxygen from the air. While the zinc salt acted as a non-innocent spectator, it potentially formed complexes with the saccharides during the reactions. The saccharides decomposed to produce carbon intermediates and gases, possibly catalyzed by the Zn(II) salt. Initially, the intermediates exhibited a black color, which gradually changed to yellow before eventually reaching a white color. This synthesis route offers a facile and scalable method for producing ZnO nanoparticles derived from various saccharides.

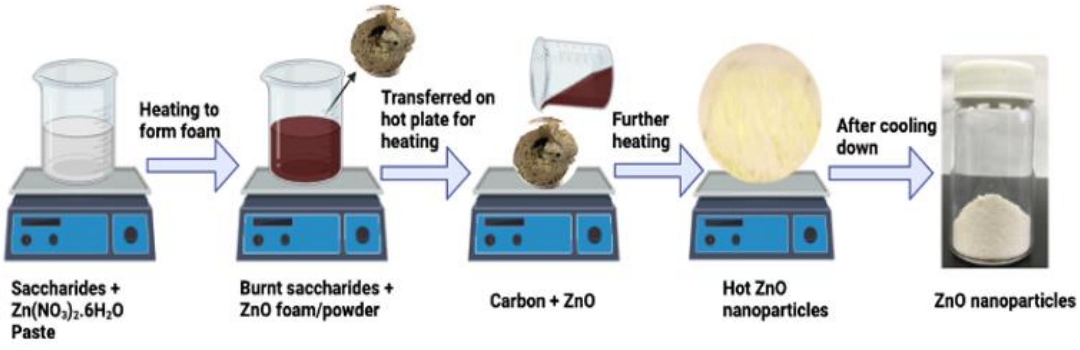

Figure 4.1: Synthesis of ZnO NPs through a saccharide's combustion methodology.

4.3.2. Microscopy analysis of ZnO NPs by TEM.

The results of the TEM images indicated that the ZnO NPs (Dextrin-ZnO, Fructose-ZnO, Glucose-ZnO, and Starch-ZnO) exhibited varying sizes and shapes with smooth surfaces (Figure 4.2 a–d). The TEM images also shows the formation of clusters and aggregates by the overlap connection of particles.

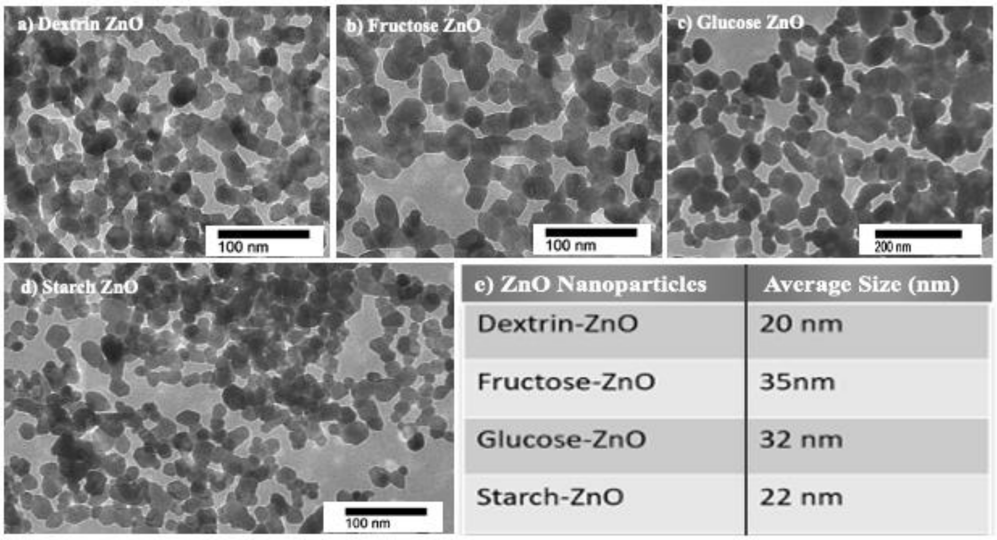

e) ZnO Nanoparticles	Average Size (nm)
Dextrin-ZnO	20 nm
Fructose-ZnO	35nm
Glucose-ZnO	32 nm
Starch-ZnO	22 nm

Figure 4.2: TEM images of the ZnO NPs a) Dextrin-ZnO, b) Fructose-ZnO, c) Glucose-ZnO, d) Starch-ZnO, and e) the average size of the ZnO NPs based on the TEM image.

3.2.2. SEM Image and EDX Spectrum of the ZnO NPs.

This aggregation phenomenon could be attributed to the high surface energy and surface area of the ZnO NPs[223]. Using ImageJ software to measure the sizes of 100 randomly selected nanoparticles, it was determined that the ZnO NPs had an average size in the nanometer range. Specifically, the mean diameter was approximately 20 nm for Dextrin-ZnO, 35 nm for Fructose-ZnO, 32 nm for Glucose-ZnO, and 22 nm for Starch-ZnO (Figure 1e).

4.3.3. SEM Analysis of the ZnO NPs

SEM and EDX images were acquired to examine the bulk morphology and elemental composition of the ZnO NPs, respectively. The SEM images of Dextrin-ZnO, Fructose-ZnO, Glucose-ZnO, and Starch-ZnO are displayed in Figure 4.3. These SEM images reveal submicron granulated ZnO NPs, with no discernible variations observed among the saccharide-derived products. An SEM-EDX analysis was conducted for the Glucose-ZnO, Fructose-ZnO, Dextrin-ZnO, and Starch-ZnO products to determine their elemental composition (Figure 4.4a–d). The EDX spectra of all saccharide-derived ZnO nanoparticles revealed strong and prominent peaks corresponding to Zn and O, indicating the absence of impurities or adulteration in the synthesized product.Tthe successful formation of ZnO nanostructures was confirmed by the information provided by the EDX. While the theoretical mass% ratio of Zn to O is 80.34% to 19.66%, the ratios obtained from the saccharide-derived ZnO NPs were not stoichiometric, as illustrated in Figure 4.4. These deviations from stoichiometry may be attributed to impurities entrapped within the lattice of the ZnO NPs. However, the nature of these impurities was not determined.

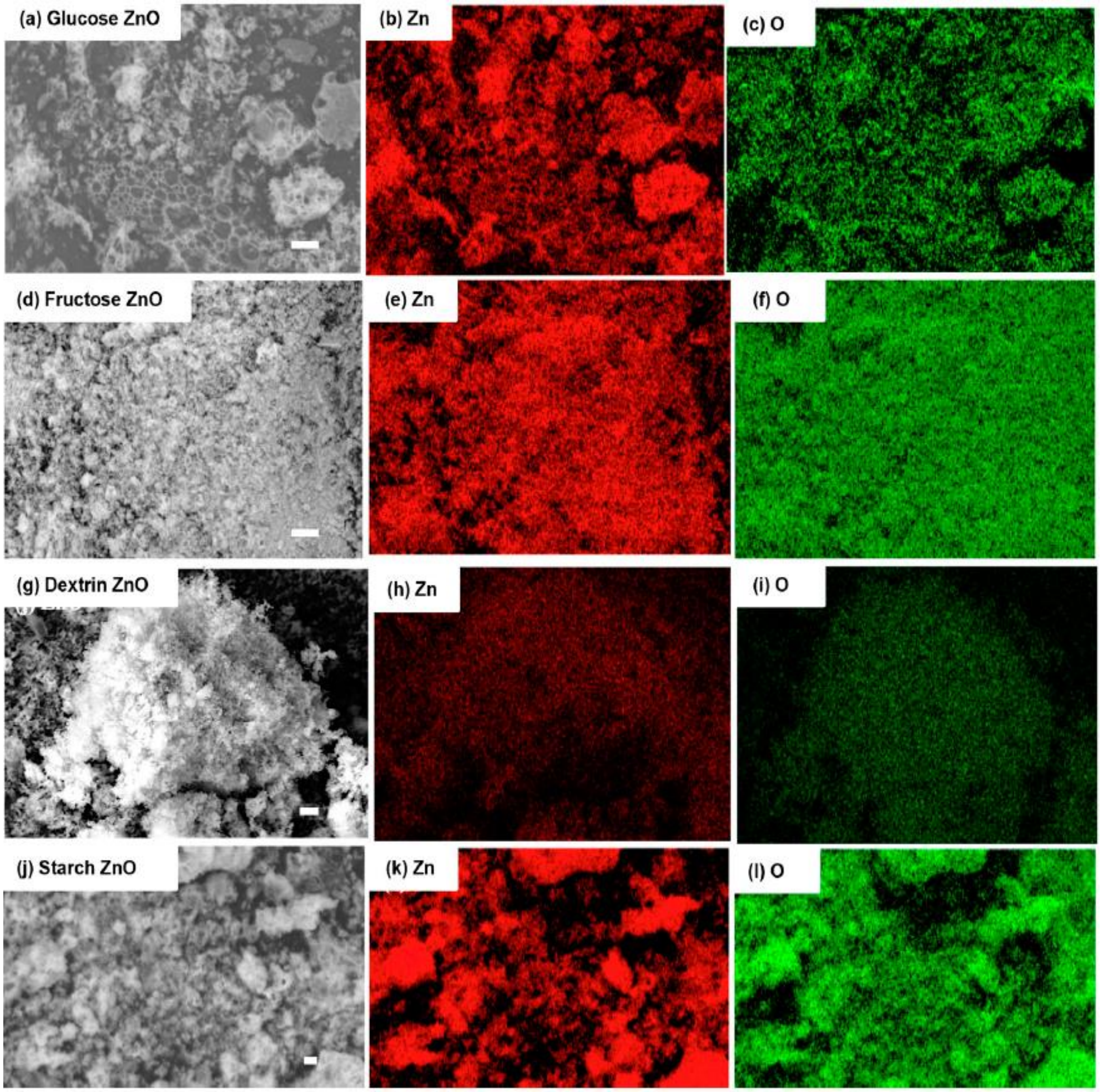

Figure 4.3: a) SEM be images of Glucose-ZnO; b), c) X-ray EDS mapping of zinc and oxygen, respectively; d) SEM be images of Fructose-ZnO; e), f) X-ray EDS mapping of zinc and oxygen, respectively; g) SEM be images of Dextrin-ZnO; h), i) X-ray EDS mapping of zinc and oxygen, respectively; j) SEM be images of Starch-ZnO; k), l) X-ray EDS mapping of zinc and oxygen, respectively. Scale bar = 100um. Colors identify the indicated element.

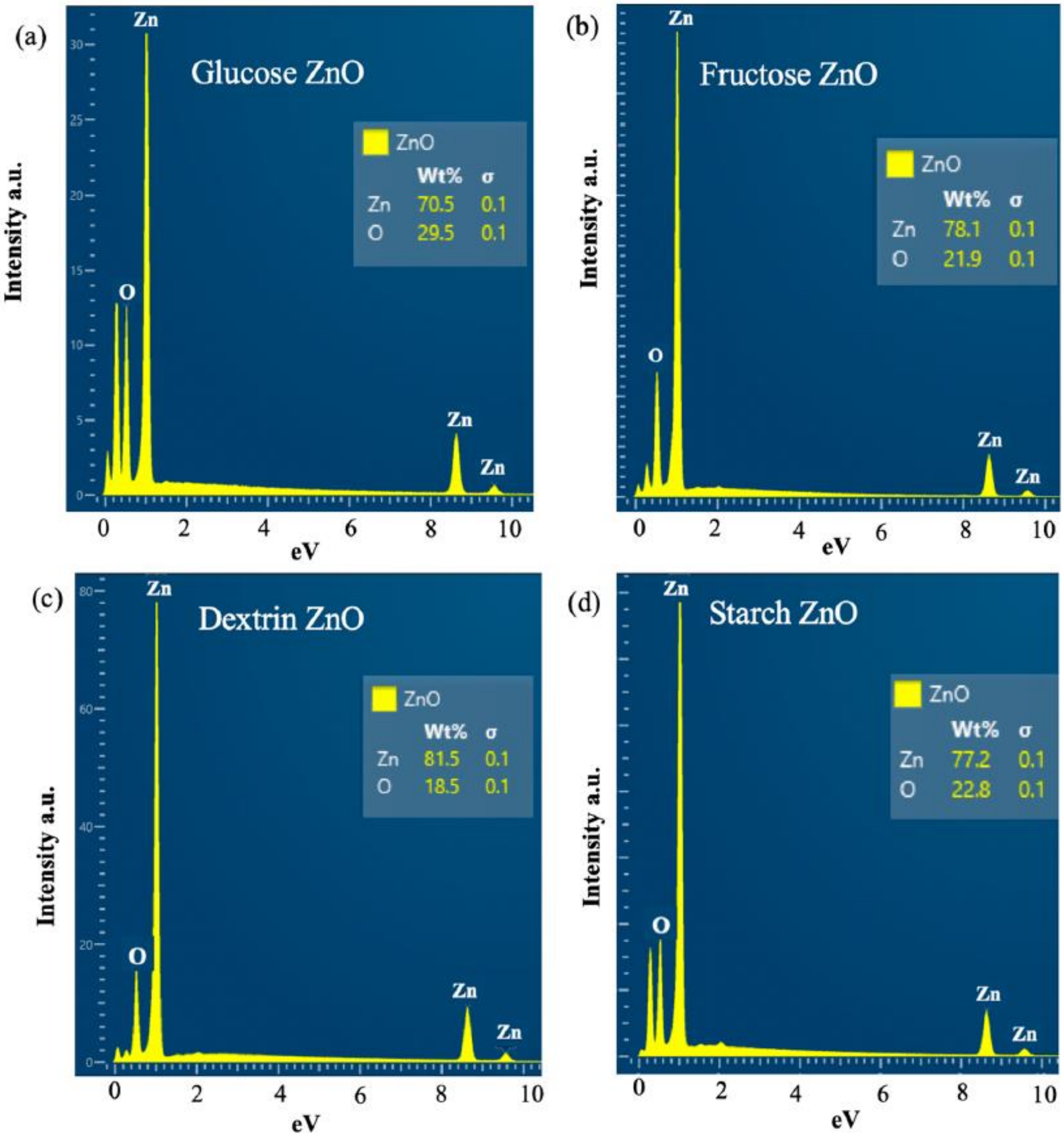

Figure 4.4: EDX spectra showing the elemental composition of a) Glucose-ZnO, b) Fructose-ZnO, c) Dextrin-ZnO, d) Starch-ZnO.

4.3.4. UV–Visible Spectrum of the ZnO NPs.

Ethanol was used to prepare a suspend the ZnO NPs with a 0.125 mg/mL concentration in which the UV–visible spectrum was taken. Figure 4a displays the UV–visible spectrum of the Fructose-ZnO NPs, while the UV–visible spectra of the remaining saccharide-derived ZnO NPs are provided in the supplementary information. All the ZnO NPs exhibited a characteristic UV-visible absorption band centered around 375 nm. This common absorption peak at approximately 375 nm suggests that these samples share a consistent optical property in the UV region. After analyzing the results, it could be concluded that there is no significant differences in the absorbance behavior of these samples at this particular wavelength. The absorption band in the UV region is because of electron excitation from the valence band to the conduction band (O2p → Zn3d). Additionally, it was observed that all the synthesized ZnO nanoparticle samples exhibited high absorbance in the UV region compared to the visible region of the electromagnetic spectrum. This high absorbance in the UV region further supports the notion that all the ZnO NPs used in this study acted as highly active photocatalysts under UV light illumination.

The optical band gap of the ZnO NPs derived from saccharides (Glucose-ZnO, Fructose-ZnO, Dextrin-ZnO, and Starch-ZnO) was estimated using UV–visible absorption spectra and the Tauc equation, as depicted in Figure 4.5 b. The analysis for the remaining saccharide derived ZnO NPs can be found in the supplementary information. The calculated band gap energies for Glucose-ZnO, Fructose-ZnO, Dextrin-ZnO, and Starch-ZnO were determined to be 3.09 eV, 3.09 eV, 3.09 eV, and 3.11 eV, respectively. These results indicate that all the ZnO nanoparticle samples exhibit band gaps lower than that of bulk ZnO (3.37 eV). The decrease in the band gap is likely attributed to the presence of defect levels within that band gap and the incorporation of donor atoms from the valence band into the nanoparticles.

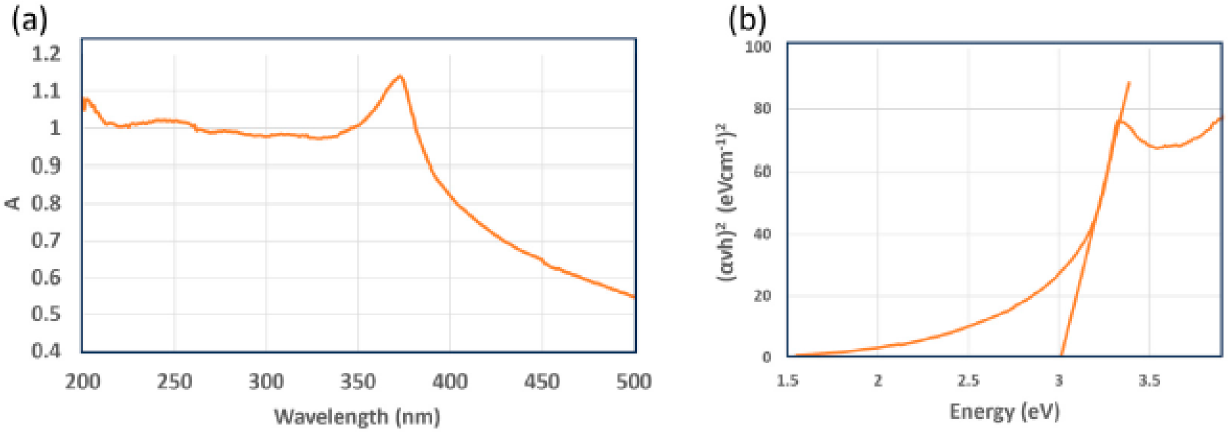

Figure 4.5: a) UV–visible absorption spectrum of Fructose-ZnO NPs' suspension in ethanol; b) Tauc plot for the determination of bandgap of Fructose-ZnO.

4.3.5. XRPD Analysis of the ZnO NPs.

The ZnO NPs underwent further characterization using X-ray powder diffraction (XRPD) to elucidate the sample's crystalline structure and crystallite size. Figure 4.6 displays the diffraction patterns of the Fructose-ZnO NPs and ZnO-control, while the XRD pattern of the remaining saccharide-derived ZnO NPs can be found in the supplementary information. The peaks observed at 2θ = 31.70°, 34.20°, 36.20°, 47.46°, 56.50°, 62.70°, 66.20°, 67.80°, 68.99°, 72.40°, and 77.10° 2 theta are characteristic of the ZnO crystalline hexagonal wurtzite structure (JCPDS 5-0664), consistent with the pattern observed for the ZnO-control[224,225]. However, it is noteworthy that the XRD peaks of the saccharide-derived samples appear much broader compared to those of the ZnO-control. This broadening suggests structural differences within the crystal lattice of the saccharide-derived samples.

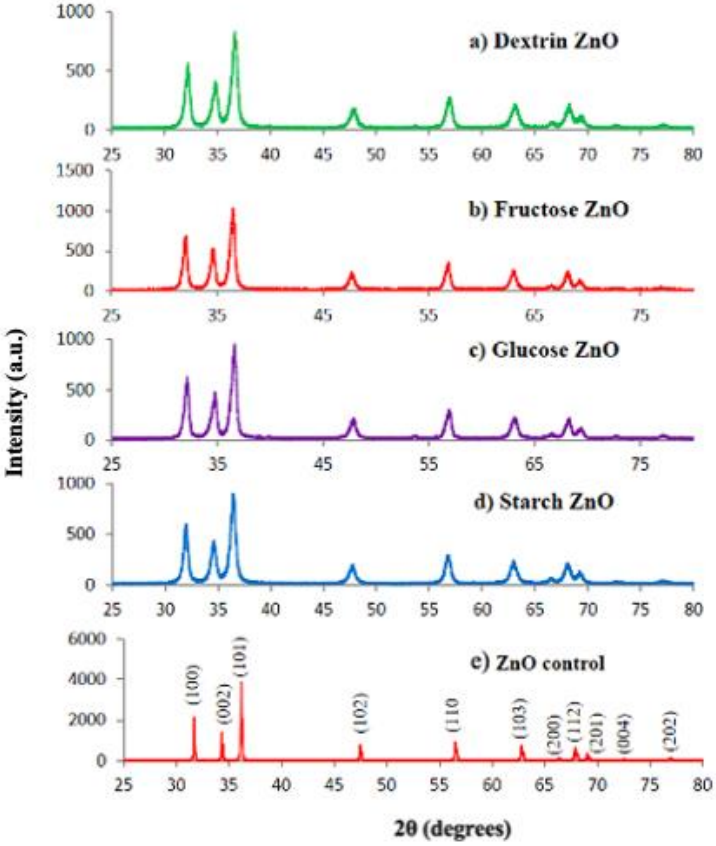

Figure 4.6: XRPD patterns of Sacharides-ZnO NPs.

The determination of the ZnO crystal size was obtained from the XRD data using the Debye–Scherrer equation[226]. The average crystalline sizes of Dextrin-ZnO, Fructose-ZnO, Glucose-ZnO, and Starch-ZnO were calculated to be 20.9 nm, 25.3 nm, 25.3 nm, and 18.2 nm, respectively. These values closely align with the averages obtained from TEM analysis. The XRPD pattern of the ZnO NPs exhibited a consistent trend with the expected pattern observed for other ZnO NPs[227]. However, the diffraction peaks of the saccharide derived ZnO NPs appeared broader compared to the control and other reported ZnO NPs. This broadening suggests significant alterations in the crystal structure, which may be responsible for enhancing the photocatalytic properties of the saccharide derived ZnO NPs.

4.3.6. XPS Analysis of the ZnO NPs.

The assessment via XPS analysis aimed to determine both the chemical state and elemental makeup of ZnO NPs derived from saccharides, alongside verifying the purity of said NPs. The XPS survey spectrum images (Figures 4.6a, d, g, and h) depict the chemical profiles of Glucose-ZnO, Fructose-ZnO, Dextrin-ZnO, and Starch-ZnO, respectively. It emerged from the analysis that ZnO NPs originating from saccharides predominantly consisted of Zn and O elements, with a minor presence of C detected. This minimal C content was presumed to stem from potential instrument contamination.

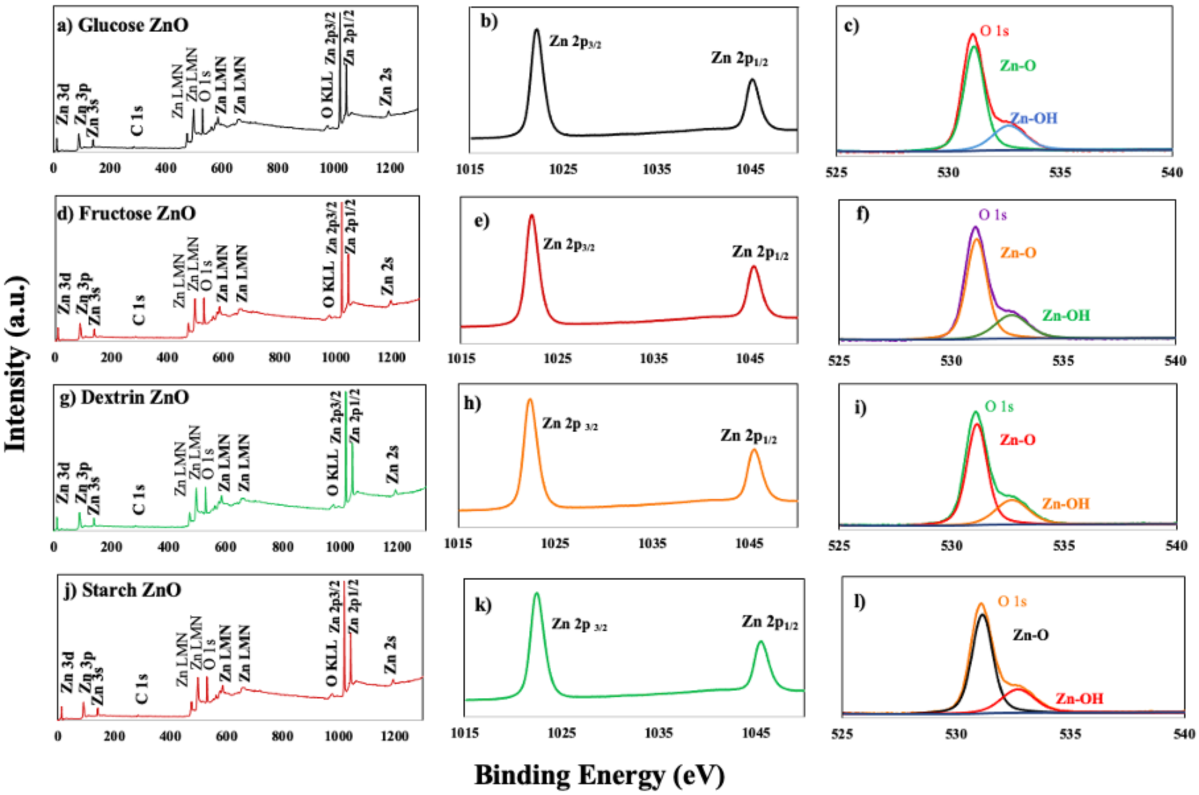

Figure 4.6: XPS patterns of Sacharides-ZnO NPs.

The XPS survey spectra of ZnO NPs also exhibited characteristic binding energies corresponding to various Zn and O states. Figures 4.7 b, e, h, and k represent the Zn 2p3/2 and

Zn 2p1/2 peaks of Glucose-ZnO, Fructose-ZnO, Dextrin-ZnO, and Starch-ZnO, respectively, indicating the presence of Zn in the ZnO NPs. Moreover, Figures 4.7 c, f, I, and j show the O 1s binding energy peaks, revealing the presence of O in the ZnO NPs. Additionally, O 1s exhibited two distinguishable peaks at about 532 eV and 533 eV, attributed to the Zn–O and Zn-OH bonds, respectively, on the surface of all ZnO NPs. The emergence of the OH group likely arose from the disintegration of the Zn-O-Zn bond, followed by the establishment of the Zn-OH bond in the synthesis process. These findings validate the integrity of all ZnO nanoparticles derived from saccharides.

4.3.7. Dyes Degradation of (MO) by Photolysis.

In this study, all four ZnO NP samples and the control ZnO sample underwent degradation of the MO dye in both deionized water (DIW) and simulated fresh drinking water (FDW) under UV light and sunlight irradiation. The photocatalytic efficiency was assessed by calculating the percent degradation of MO using Equation (2). The evaluation of MO degradation was conducted by analyzing its characteristic absorbance at 464 nm using UV-visible spectroscopy.

$$Percent\ degradation = \frac{Co-Ct}{Co} \times 100\% = \frac{Ao-At}{Ao} \times 100\% \tag{4.2}$$

Co represents the initial concentration, Ct denotes the equilibrium concentration or concentration at time t, Ao stands for the initial absorbance, and At represents the absorbance at time t of MO at 464 nm on the absorbance spectra. As an illustration, the time-dependent UV-vis spectrum of the MO solution during its degradation by Fructose-ZnO is depicted in Figure 4.7a. It can be observed that the MO concentration gradually decreased with the progression of photocatalysis time. The absorption maxima decreased to baseline at 464 nm after 20 minutes of reaction, indicating efficient MO photodegradation in water by Fructose-ZnO. Similar UV-vis spectra with a gradual decrease in absorbance at 464 nm were obtained for the other ZnO NP samples.

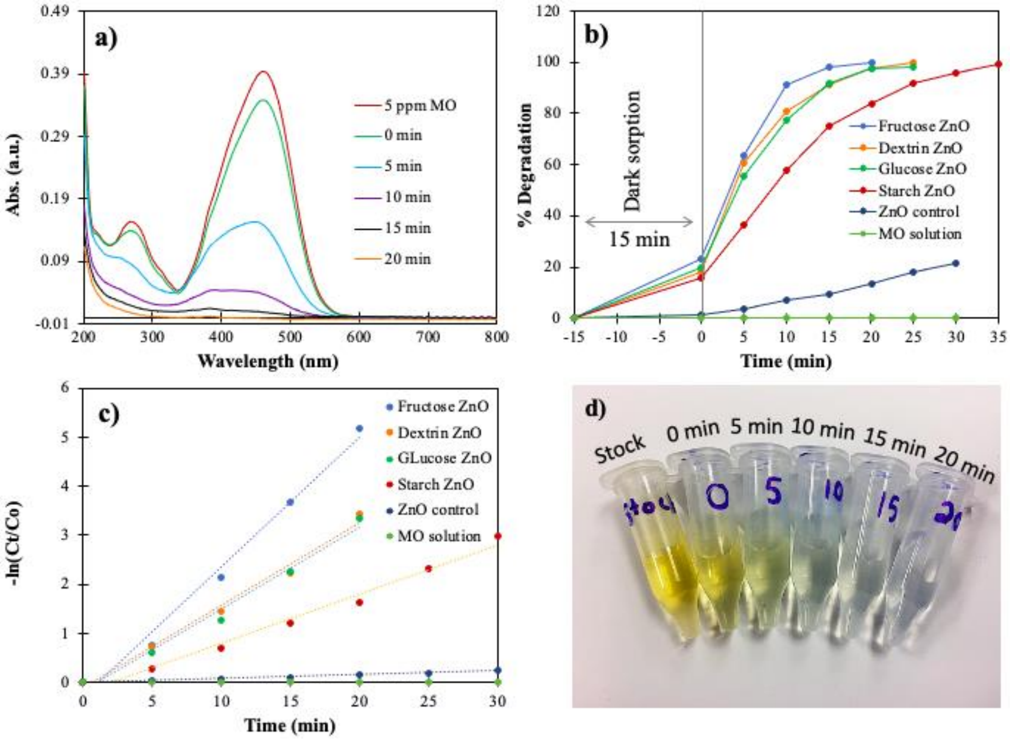

Figure 4.7: a) Time-dependent UV-vis spectra of MO (5 ppm) solution in DIW during photocatalysis by Fructose-ZnO. b) Percent degradation of MO by ZnO NPs and controls. c) Pseudo-first-order kinetics of MO photodegradation. d) A digital photograph MO solution during photocatalysis in presence of Fructose-ZnO.

The percentage of MO degradation over time was calculated and is illustrated in Figure 7b. It was observed that Fructose-ZnO exhibited the highest photocatalytic activity, completely decolorizing the MO solution in approximately 20 minutes. Glucose-ZnO and Dextrin-ZnO achieved complete decolorization in around 25 minutes. Starch-ZnO showed relatively slower activity, reaching complete decolorization of MO after 35 minutes. While the photocatalytic activities of Fructose-ZnO, Glucose-ZnO, and Dextrin-ZnO were similar, Starch-ZnO demonstrated comparatively slower photocatalytic activity. Since starch is a large polysaccharide with an average molecular weight of 59.7 kDa, it is possible that its reaction with the zinc salt generated different intermediates compared to the reactions with the smaller saccharides. It is speculated that the low-molecular-weight saccharides may have produced smaller intermediates that facilitated the formation of ZnO motifs with higher photocatalytic activity. Although direct evidence explaining the variations in photocatalytic activity among the saccharide derived ZnO NPs is lacking, several factors such as differences in surface area and the nature of impurities or intermediates that template the active nanostructures in the ZnO NPs could contribute, warranting further investigation.

After 30 minutes of UV light exposure, the ZnO-control exhibited only about 22% degradation of MO under the same experimental conditions. This limited degradation could be attributed to the more thermodynamically stable state achieved when no saccharide was used during the synthesis. Furthermore, under UV light irradiation alone, there was no observed decolorization of the MO solution. From the SEM images and the photocatalytic performances, it can be inferred that the saccharides aided in the formation of a metastable state of ZnO with nanoscopic size ranges and a high active specific surface area. These characteristics likely contributed to the high photocatalytic performance observed.

The photocatalytic degradation kinetics of MO were studied by the pseudo-first-order kinetic model in Equation (3) [228],[229], which is as follows:

$$kt = -\ln (Ct/Co) \tag{4.3}$$

In Equation (3), k is the photodegradation rate constant (min^{-1}), Co is the initial concentration of MO at the beginning of the reaction, and Ct is the concentration of MO at time t.

Figure 7c illustrates that the photodegradation of MO in DIW adhered to the pseudo-first-order kinetics mechanism. The plot of −ln(Ct/Co) against time (t) displayed linear trends, indicating that the photocatalytic degradation of MO followed the Langmuir–Hinshelwood model[230]. The rate constants for the degradation of MO on different ZnO NPs were determined from the slopes of the linear regression lines. The calculated rate constant values are summarized in Table 1 below. Additionally, Figure 4.7d provides a digital photograph depicting the decolorization of the MO solution during photocatalysis with Fructose-ZnO over time.

Table 4.1: Rate constants of all the photocatalytic reactions performed in this study.

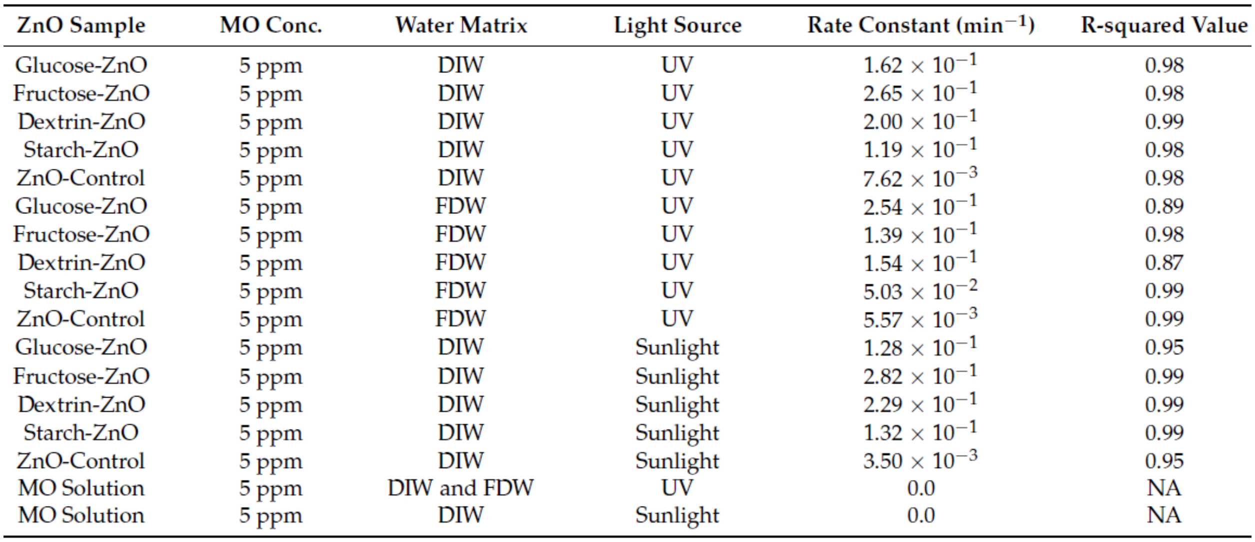

ZnO Sample	MO Conc.	Water Matrix	Light Source	Rate Constant (min^{-1})	R-squared Value
Glucose-ZnO	5 ppm	DIW	UV	1.62×10^{-1}	0.98
Fructose-ZnO	5 ppm	DIW	UV	2.65×10^{-1}	0.98
Dextrin-ZnO	5 ppm	DIW	UV	2.00×10^{-1}	0.99
Starch-ZnO	5 ppm	DIW	UV	1.19×10^{-1}	0.98
ZnO-Control	5 ppm	DIW	UV	7.62×10^{-3}	0.98
Glucose-ZnO	5 ppm	FDW	UV	2.54×10^{-1}	0.89
Fructose-ZnO	5 ppm	FDW	UV	1.39×10^{-1}	0.98
Dextrin-ZnO	5 ppm	FDW	UV	1.54×10^{-1}	0.87
Starch-ZnO	5 ppm	FDW	UV	5.03×10^{-2}	0.99
ZnO-Control	5 ppm	FDW	UV	5.57×10^{-3}	0.99
Glucose-ZnO	5 ppm	DIW	Sunlight	1.28×10^{-1}	0.95
Fructose-ZnO	5 ppm	DIW	Sunlight	2.82×10^{-1}	0.99
Dextrin-ZnO	5 ppm	DIW	Sunlight	2.29×10^{-1}	0.99
Starch-ZnO	5 ppm	DIW	Sunlight	1.32×10^{-1}	0.99
ZnO-Control	5 ppm	DIW	Sunlight	3.50×10^{-3}	0.95
MO Solution	5 ppm	DIW and FDW	UV	0.0	NA
MO Solution	5 ppm	DIW	Sunlight	0.0	NA

The photodegradation of MO was further investigated in a simulated fresh drinking water (FDW) matrix, which contains various dissolved salts commonly found in drinking water. Since the presence of dissolved salts can influence photocatalytic performance, studying MO degradation in simulated FDW validates the efficiency and practical applicability of the ZnO NPs under real-life conditions. Figure 8a displays the UV–visible spectrum of MO photodegradation over time in simulated FDW using Fructose-ZnO as a representative catalyst. Almost complete decolorization of MO was achieved after 30 minutes of UV light exposure, indicating that the photocatalytic performance of ZnO NPs in simulated FDW is comparable to that in DIW. The percent degradation of the MO solution in simulated FDW (Figure 8b) was found to be similar to that in DIW (Figure 7b). Therefore, it can be concluded that the photocatalytic performance of the ZnO NPs synthesized in this study remains consistent across different water matrices, regardless of the presence of dissolved salts.

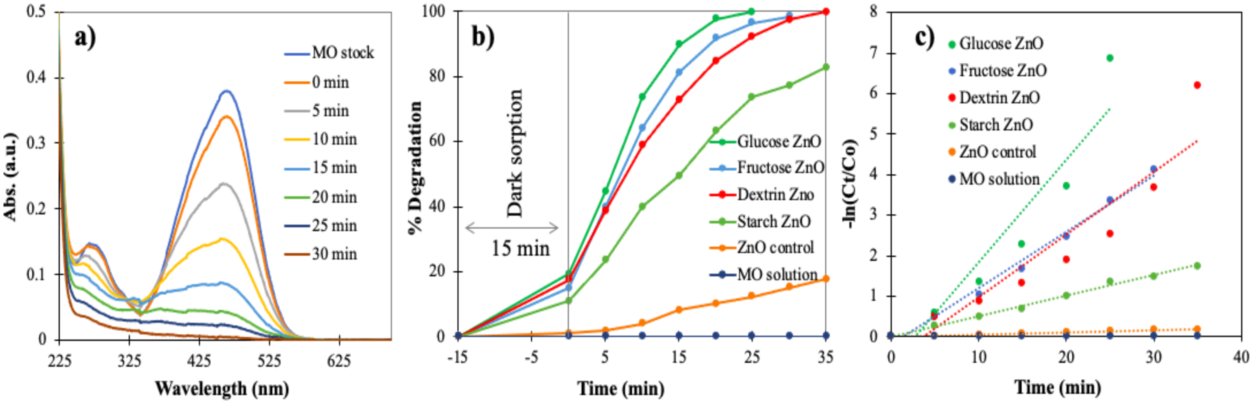

Figure 4.8: a) Time-dependent UV-vis spectra of MO (5 ppm) solution in simulated FDW during photocatalysis by Fructose-ZnO. b) Percent degradation of MO by ZnO NPs and controls. c) Pseudo-first-order kinetics of the MO photodegradation.

The plot of −ln(Ct/Co) versus time (t) exhibited a linear trend for MO degradation in the simulated FDW, similar to the trend observed in DIW (as shown in Figure 8c). However, upon closer examination, it was noted that all saccharide-mediated ZnO NPs and controls displayed nearly identical trends, consistent with Figure 7c, except for Glucose-ZnO and Dextrin-ZnO, which showed slight deviations from the linear trend. Upon removing the last data point for

Glucose-ZnO and Dextrin-ZnO, both datasets conformed to the expected pseudo-first-order kinetics. This suggests that the final data point may not align with the rest of the dataset and significantly deviates when compared to the data mean at shorter time intervals. This deviation could be attributed to changes in the ionic composition of the simulated FDW, which raises the possibility of interference by ions in noncatalytic processes. Consequently, the observed data suggest that the degradation kinetics of MO in both DIW and simulated FDW conformed to the pseudo-first-order reaction mechanism. Moreover, the linear relationship between −ln(Ct/Co) and time (t) for the photodegradation of MO also followed the Langmuir–Hinshelwood (LH) mechanism. The rate constants (kapp) of MO degradation were calculated from the slope of the −ln(Ct/Co) versus time (t) graph, as presented in Table 1.

The assessment of ZnO NPs' efficiency progressed through MO degradation under sunlight exposure. For conducting the MO photodegradation reaction, a sunny day was deliberately chosen to ensure natural sunlight illumination, with an average sunlight intensity measured to be ~100,000 lux during the photodegradation. The percentage of MO degradation over time by different ZnO NPs in DIW under sunlight is depicted in Figure 9a. It was observed that Fructose-ZnO exhibited the highest photocatalytic activity under direct sunlight and UV light, achieving nearly complete decolorization of MO within 12 minutes. In comparison, Dextrin-ZnO achieved almost complete decolorization after 15 minutes, and Glucose-ZnO achieved 92% decolorization after 15 minutes. However, Starch-ZnO demonstrated relatively slower activity, achieving 92% decolorization of MO after 18 minutes.

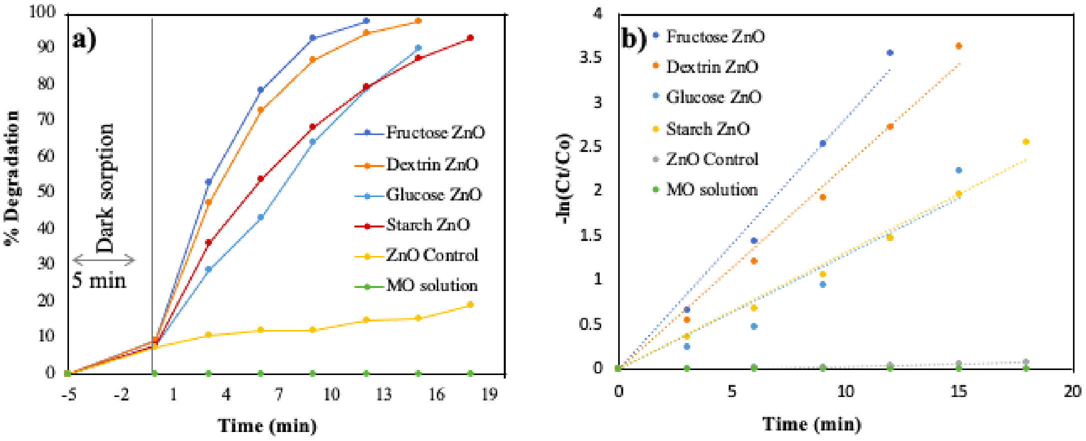

Figure 4.9: (a) Percent degradation of MO in DIW under sunlight irradiation by ZnO NPs and controls. (b) Pseudo-first-order kinetics of the MO degradation under sunlight irradiation.

After 18 minutes of sunlight exposure, the ZnO-control showed approximately 19% MO degradation under the same experimental conditions when no saccharide was used during the synthesis. This indicates that the nanostructured nature of the saccharide-derived ZnO NPs contributes to higher photocatalytic activity compared to the ZnO-control.

Figure 4.9 b illustrates that MO photodegradation in the DIW under sunlight followed the same pseudo-first-order kinetics mechanism, as evidenced by the linear trends observed in the plot of −ln(Ct/Co) versus time (t). This linear relationship suggests that the photocatalytic reaction of MO degradation also adhered to the Langmuir–Hinshelwood model.

Comparing MO degradation under UV light and sunlight irradiation revealed faster degradation under sunlight illumination. This acceleration could be attributed to the higher intensity of sunlight (~100,000 lux) compared to UV light (22,000 lux) in the box reactor. Within the solar spectrum, UV light constitutes approximately 3–5% (λ < 400 nm), while 47% is attributed to visible light (400 > λ < 700 nm), with the remainder in the infrared region. This UV portion of sunlight likely contributed to the photocatalytic activity of the ZnO NPs in MO degradation. Table 1 presents the rate constants for all the photocatalytic reactions conducted within this study.

4.3.8. Analysis of ROS Generated by the ZnO NPs.

The generation of hydroxyl radicals (•OH) was confirmed through photoluminescence (PL) studies using terephthalic acid (TA)[231]. This study operates on the following mechanism: The •OH (photocatalytically generated) on the ZnO NPs reacts with sodium terephthalate, forming 2-hydroxy terephthalate, which exhibits a strong fluorescence emission band centered at 425 nm when excited at 315 nm. Thus, higher fluorescence intensity indicates a greater quantity of •OH generation at the water–catalyst interface.

Figure 4.10 illustrates the results of the TA PL tests. The process of terephthalate reacting with the photocatalytically generated •OH radical to produce 2-hydroxy terephthalate is illustrated in Figure 4.10a. Figure 4.10b displays the fluorescence emission spectra of the 2-hydroxy terephthalate solution over time without the presence of Dextrin-ZnO NPs. The fluorescence intensity of the 2-hydroxy terephthalate solution gradually increases with the duration of UV light exposure, indicating a gradual rise in the production of •OH over time under UV light illumination. The time-dependent fluorescence emission spectra of the 2-hydroxy terephthalate solution photocatalyzed by Dextrin-ZnO are shown in Figure 4.10c. Figure 4.10d compares the production of •OH by the saccharide-derived ZnO NPs. Plotting the duration of light irradiation against the fluorescence intensity of the 2-hydroxy terephthalate solution at 425 nm yields this comparison.

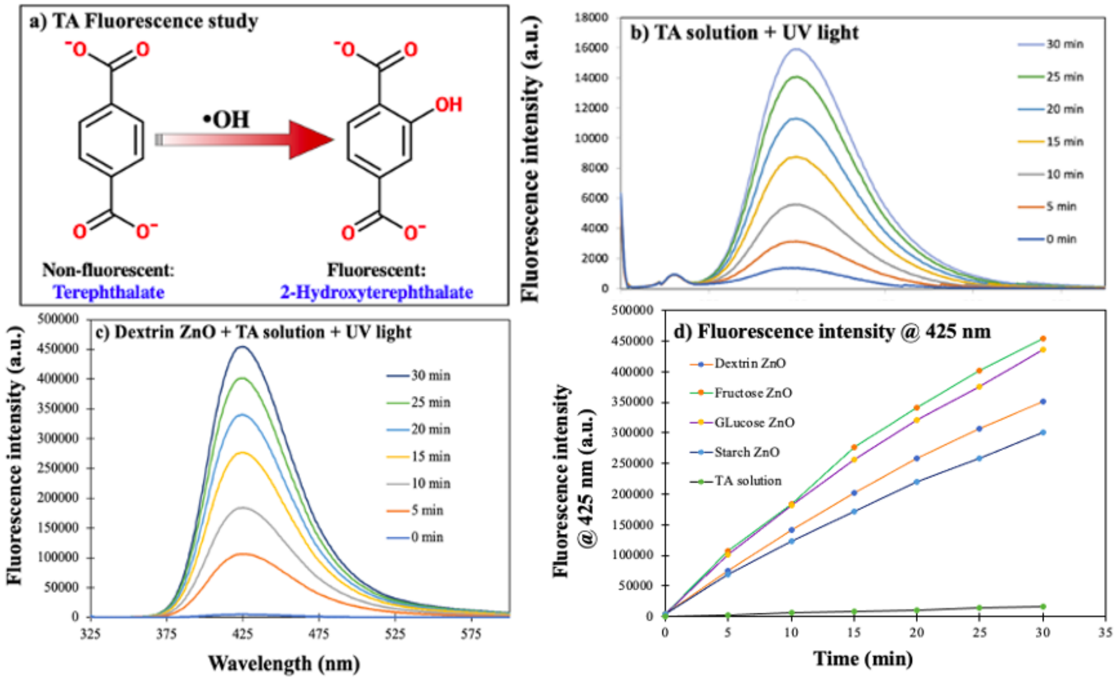

Figure 4.10: (a) Reaction of terephthalate with the photocatalytically generated •OH radical to form 2−hydroxy terephthalate, (b) time-dependent fluorescence emission spectra of 2−hydroxy terephthalate solution without ZnO NPs, (c) fluorescence emission spectra of 2−hydroxy terephthalate solution photocatalyzed by Dextrin-ZnO with respect to time, and (d) fluorescence emission intensity at 425 nm versus time graph for different saccharide-derived ZnO NPs.

The significantly higher PL intensity of the TA solution at 425 nm catalyzed by the ZnO NPs compared to the control TA solution without any ZnO confirms the generation of •OH during UV light irradiation by the ZnO NPs.

Fructose-ZnO and Glucose-ZnO exhibited a higher rate of •OH generation compared to the other ZnO NPs, along with the slower rate observed for Starch-ZnO. This additional evidence solidifies the photocatalytic capabilities of these ZnO NPs in the oxidative breakdown of MO.

These results highlight the potential of ZnO NPs to degrade various organic pollutants in water and contribute to water sanitation efforts.

4.3.9. Stability Experiment for the ZnO NPs.

The repetitive stability test aimed to assess the resilience of the ZnO NPs by assessing their ability to degrade MO over multiple cycles. In this experiment, a solution containing 30 mL of a 5 ppm MO solution and 30 mg of Fructose-ZnO NPs (chosen as a representative) was exposed to UV light for 30 minutes. After exposure, the mixture was centrifuged at 4000 rpm for 10 minutes to obtain a transparent supernatant. The transparency indicated the removal of degraded MO from the solution. The transparent liquid was then analyzed using UV-vis spectroscopy to determine the percentage of MO degradation. For ensuing cycles, the process was reiterated, utilizing the ZnO NPs centrifuged from the prior cycle.

Figure 4.11 presents the performance of the ZnO NPs in photocatalysis across three cycles, showcasing their consistent and dependable efficacy. Across each cycle, over 95% of the MO was degraded by the ZnO NPs. These findings indicate that the saccharide derived ZnO NPs synthesized in this investigation have the capability to serve as robust and efficient photocatalysts for organic pollutant degradation in wastewater.

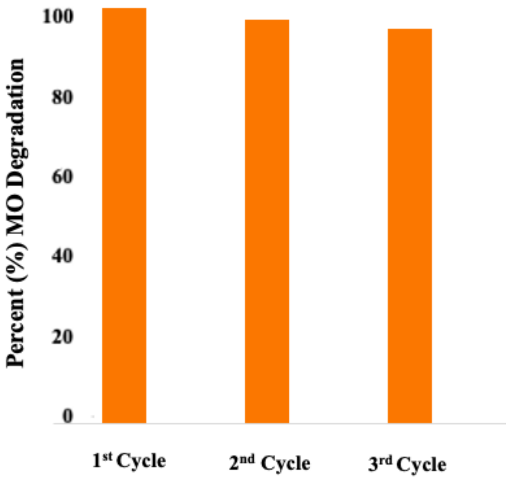

Figure 4.11: Cyclic stability of Fructose-ZnO NPs during MO degradation for 3 cycles.

4.4. Conclusions

This study explores the synthesis, characterization, and photocatalytic activity of zinc oxide nanoparticles (ZnO NPs) derived from saccharides such as glucose, fructose, dextrin, and starch. The synthesis method involves heating Zn (NO3)2•6H2O in the presence of saccharides at approximately 500 ºC, yielding ZnO NPs with high photocatalytic activity. Extensive characterization using X-ray powder diffraction (XRPD), X-ray photoelectron spectroscopy (XPS), UV-visible spectroscopy (UV-vis), scanning electron microscopy-energy-dispersive X-ray spectroscopy (SEM-EDS), and transmission electron microscopy (TEM) elucidates the optical properties, crystal structure, chemical composition, morphology, and size distribution of the ZnO NPs.. Evaluation of photocatalytic activity demonstrates efficient degradation of methyl orange (MO) dye in aqueous solutions under both UV-C and natural sunlight irradiation, with Fructose-ZnO NPs exhibiting the highest activity. Compatibility testing in deionized water and simulated fresh drinking water matrices confirms consistent performance across different water compositions. Terephthalic acid photoluminescence tests confirm the generation of hydroxyl radicals (•OH) by the saccharide derived ZnO NPs, crucial for photocatalytic degradation of organic pollutants. Additionally, cyclic stability tests reveal reliable performance over three cycles, with over 95% MO degradation in each cycle. These findings underscore the potential of saccharide derived ZnO NPs as efficient and durable photocatalysts for wastewater treatment and sanitation applications, offering insights for sustainable water treatment technologies.

NANOPARTICLES IN ELECTROCATALYSIS

Chapter 5: High-performance catalytic oxygen evolution reaction with nanocellulose-derived biocarbon Fe/zeolite/carbon nanotube composites.

5.1. Introduction

Electrocatalytic water splitting presents a promising avenue for harnessing renewable electricity to produce hydrogen, a valuable chemical fuel. The success of this process is intricately linked to the performance of electrocatalysts, making catalytic advancements a central focus for improving the overall energy conversion efficiency of the water-splitting reaction[232]. As a result, significant research endeavors have been devoted to the development of novel catalytic materials and the comprehensive identification of active sites within stable, efficient, and abundant catalysts[233].

One pivotal challenge in the synthesis of hydrogen fuel through water splitting is the intricate four-electron transfer process involved in the Oxygen Evolution Reaction (OER). This reaction, which occurs at the anode, entails the conversion of water into oxygen gas, protons, and electrons. However, this process is marred by substantial efficiency losses and significant material degradation over time[234]. Such drawbacks limit the use of cost-effective catalysts in commercial electrolyzers and hinder the widespread adoption of water splitting for hydrogen production. To overcome these hurdles, there is a pressing need for the development of low-cost OER catalysts. These catalysts must possess the capacity to reduce the overpotential required for the OER, enhance catalytic activity, and minimize the damage incurred during the reaction process. Achieving these goals would not only bolster the efficiency of hydrogen production but also advance the feasibility of renewable energy storage and utilization on a larger scale[235].

Ir-based and Ru-based materials have exhibited remarkable performance as catalysts for the Oxygen Evolution Reaction (OER) under acidic conditions. However, their limited availability and high cost pose significant challenges for their widespread implementation in sustainable energy technologies on a global scale[236]. Consequently, there has been a substantial increase in research efforts aimed at identifying alternative, cost-effective, and readily available catalysts with high activity and long-term durability. This research has predominantly focused on transition metals such as iron (Fe), cobalt (Co), nickel (Ni), and others, as well as their phosphides, oxides, oxyhydrates, perovskites, nitrides, and sulfides derivatives.

Nonprecious transition metals and their various derivatives have emerged as promising candidates for electrocatalytic water oxidation in alkaline solutions, offering viable alternatives to Ir- and Ru-based catalysts[237],[238]. This research has encompassed both monometallic-based catalysts, featuring single elements like Co, Ni, and Fe, and bimetallic-based catalysts, combining elements such as CoFe, FeNi, and FeMn. These studies seek to uncover catalysts that not only match the performance of their precious metal counterparts but also provide a sustainable and economically viable solution for advancing water oxidation technologies in alkaline environments[239].

In a typical electrochemical water-splitting system (2H2O → 2H2 + O2), the Hydrogen Evolution Reaction (HER) occurs at the cathode, while the Oxygen Evolution Reaction (OER) takes place at the anode. The kinetics of these processes are influenced by the specific characteristics of the localized electrolyte environment. During OER, the chemical mechanism involves the transformation of 4OH− ions into O2, 2H2O, and 4e−. In contrast, HER proceeds through the reduction of 2H2O molecules to form H2 and 2OH− ions in an alkaline environment[240],[241].

Electrocatalysis in the context of OER presents unique challenges due to the involved four-electron transfer process, resulting in substantial energy losses. Throughout OER, various intermediates in the form of MO-, MOH-, and MOOH-type species (where M represents the surface metal cation) are commonly generated during the electron transfer events[242],[243].

For the development of high-performance electrocatalysts, a comprehensive understanding of structure-property relationships in the OER is imperative. Accurate characterization of catalyst composition, continuous monitoring of activity trends, and real-time identification of active sites through in situ and operando methods are vital components of this endeavor[244].

An effective catalyst generally possesses a large surface-active area and an adjustable electronic structure. These characteristics enable the provision of a sufficient number of active sites and the attainment of the appropriate adsorption energy for reactants and intermediates. Catalysts with precursor materials exhibiting hollow nanostructures on their surfaces offer distinct advantages. These include significantly increased specific surface areas, abundant active edge sites, and a high density of active sites compared to bulk materials[245],[246],[247].

Moreover, the presence of substantial void space within these hollow nanostructures can markedly alleviate mass transfer limitations. Additionally, the porous internal structure can effectively mitigate structural stresses induced by repetitive ion insertion/extraction processes. Furthermore, it can be employed to modulate potential volume changes that may occur during the electrocatalytic reaction mechanism, contributing to enhanced catalyst stability and efficiency[248],[249].

Crystalline nanocellulose (CNC) is a type of cellulose with remarkable attributes that make it highly advantageous for various applications. These characteristics include a high aspect ratio, a specific surface area, substantial tensile strength, flexibility, hydrophilic surface properties, and biodegradability. Additionally, CNC possesses active functionalities on its surface, rendering it amenable to chemical modification.[250]

The unique combination of these traits' positions CNC as a promising alternative for the production of a diverse range of composites. These composites find relevance in numerous fields, including biomedicine, materials science, and catalysis, among others. In the realm of biomedicine, CNC-based materials can be employed for drug delivery, tissue engineering, and medical device fabrication. In materials science, CNC serves as a reinforcing agent in polymers, enhancing mechanical properties and reducing environmental impact. In catalysis, CNC offers a versatile support for immobilizing catalytic nanoparticles, facilitating various chemical reactions[251],[252].

Furthermore, the distinctive characteristics of nanocellulose make it an excellent candidate for use as a biocarbon source and template for the encapsulation of nanoparticles. This dual capability allows for the development of innovative materials and processes, contributing to advancements in sustainability and technology across multiple disciplines[253].

Cellulose nanomaterials have previously been used as photocatalysts for water splitting and other reactions. Li et al. developed TiO2 fiber nanorods for photoelectrical water splitting by atomic layer deposition of titanium onto cellulose nanofibers followed by heating at 600 °C, calcinating the CNFs, leaving behind porous structures that were found to be efficient catalysts[254],[255]. In other work, Li et al. incorporated platinum nanoparticles into the TiO2 nanofiber to improve the photocatalytic hydrogen production[256]. These processes involve atomic layer deposition and thus specialized equipment to produce. Nair et al. created photocatalysts by low temperature in situ growth of TiO2 nanorods onto CNCs followed by Au nanocrystals[257].

However, they did not evaluate the catalysts for water-splitting reactions. In this work, a straightforward solution-based method of producing electrodes modified Fe-zeolite nanoparticles encapsulated by nanocellulose-derived biocarbon is described.

In this study, we introduce an innovative nanocatalyst by leveraging nanocellulose to fabricate a highly porous material characterized by a substantial surface area, ideally suited for encapsulating metallic iron nanoparticles within its framework. The carbon matrix employed in this catalyst exhibits a graphene-like structure, which enhances electron conductivity, facilitating efficient interactions among the metallic particles. This, in turn, augments the electrocatalytic properties of the nanomaterial.

Our investigation extends to a comparative analysis of two distinct forms of nanocellulose, namely nanocrystals and nanofibrils. Additionally, we explore the impact of incorporating carbon nanotubes into the electrocatalytic process for oxygen evolution. These experiments are conducted within a standard three-electrode system operating under alkaline electrolyte conditions.

The utilization of nanocellulose as a template for metallic iron nanoparticles offers a unique approach to enhance catalytic performance while concurrently addressing environmental and sustainability considerations. Our research findings shed light on the electrochemical nuances associated with different forms of nanocellulose and the potential benefits of incorporating carbon nanotubes in the pursuit of efficient oxygen evolution electrocatalysis.

5.2. Materials and Methods.

5.2.1. Chemicals and Reagents.

All of the chemicals were used as received without any further purification. The following chemicals were used to prepare the Nanocellulose-Zeolite-Fe nanocomposite. The Zeolite ZSM-5 (400m2/g, in a mole ratio of 30:1 SiO2:Al2O3) was purchased from Alfa Aesar, iron sulfate hexahydrate (FeSO4.7H2O) (ACS reagent, ≥99.0%) was purchased from Sigma-Aldrich, the nanocellulose materials were produced at the USDA Forest Service Forest Products Laboratory (FPL), Madison, WI, USA. Deionized (DI) water (>18.20 MI cm resistivity) was used from the Milli-Q® instrument (Millipore Corporation).

5.2.1.1 Production of Cellulose Nanomaterial

Cellulose nanocrystals and cellulose nanofibrils were produced at pilot scale at FPL, and the procedures are described in detail elsewhere[258],[259]. Briefly, CNCs were prepared by sulfuric acid hydrolysis of commercial softwood pre-hydrolysis Kraft dissolving pulp, and the CNFs were produced by TEMPO (2,2,6,6-Tetramethylpiperidin-1-yl)oxyl) oxidization of bleached Kraft Eucalyptus at pH 10 [260].

5.2.2. Synthesis of Fe/Zeolite@C_{CNC} (1)

In a 20 mL beaker, 1.00 g of FeSO4·6H2O was introduced and subsequently dissolved in the minimum volume of deionized (DI) water, approximately 5 mL. To this solution, 1.00 g of Zeolite was added, and the resulting suspension was vigorously stirred for a duration of 5 minutes. Following this, 8.00 g of nanocellulose nanocrystals was introduced into the suspension, and the mixture was stirred manually with a spatula until a homogeneous paste-like consistency was achieved. Subsequently, the prepared mixture underwent a lyophilization process for a period of 24 hours. The outcome of this process yielded a white-green foam-like material. To further process the obtained material, it was subjected to carbonization in a furnace. The carbonization process occurred at 800°C, carried out under a continuous flow of argon gas for a duration of 3 hours. The heating rate applied during this process was set at 5°C per minute. Upon completion of the carbonization step, the resulting product, now black in appearance, was carefully removed from the furnace and allowed to cool down to room temperature. Finally, the product was stored in a glass vial for future use in subsequent experiments or applications.

5.2.3. Synthesis of Fe/Zeolite@C_{CNF} (2)

The preparation of the composite followed a procedure similar to the one described previously in step **(1)**. However, in this instance, nanocellulose nanofibrils were employed instead of nanocellulose nanocrystals. The composite material containing nanocellulose nanofibrils was obtained and stored in a glass vial to be used for further experimentation or applications as needed.

5.2.4. Synthesis of Fe/Zeolite/CNT@C_{CNC} (3)

The black powder obtained in step **(1)** was combined with 500 mg of single carbon nanotubes. This mixing process was conducted meticulously using a mortar and pestle, and it continued for a duration of 1 hour. This step aimed to ensure thorough blending and homogeneity between the two components, creating a composite material suitable for subsequent applications or experiments. The obtained material was stored in a glass vial to be used for further experimentation or applications as needed.

5.2.5. Synthesis of Fe/Zeolite/CNT@C_{CNF} (4)

The black powder obtained in step **(2)** was combined with 500 mg of single carbon nanotubes. This mixing process was conducted meticulously using a mortar and pestle, and it continued for a duration of 1 hour. This step aimed to ensure thorough blending and homogeneity between the two components, creating a composite material suitable for subsequent applications or experiments. The obtained material was stored in a glass vial to be used for further experimentation or applications as needed.

5.2.6. Characterization of the materials.

The synthesized nanomaterial underwent an extensive characterization process using a range of analytical techniques to comprehensively assess its properties. First, Powder X-ray Diffraction (PXRD) patterns were obtained using a Bruker D8 Discover X-ray Diffractometer, allowing for the examination of its crystalline structure and chemical composition. Next, the morphologies, microstructures, and elemental composition of the nanocatalyst were scrutinized using Transmission Electron Microscopy (TEM, Model: Hitachi H-7650) and Scanning Electron Microscopy (SEM, Model: Hitachi SU-3500), equipped with energy-dispersive X-ray spectroscopy (EDS) instruments. To gain insights into the distribution of elements within the material, elemental analysis color mapping was carried out using backscattering electron imaging.

Further characterization included X-ray Photoelectron Spectroscopy (XPS), conducted with a Thermo Fisher Scientific instrument, K alpha+, featuring an Al anode. During analysis, charge compensation was achieved using an Argon flood gun, and chamber pressure was carefully maintained within the range of 0.5-1x10-8 mBar. These rigorous analytical techniques collectively provided a comprehensive understanding of the nanomaterial's structural, morphological, and elemental attributes. This multifaceted characterization approach served to inform its potential applications and research implications with greater precision.

5.2.7. OER Experimental Methods.

The catalyst inks, including RuO2, Fe/Zeolite@CCNC(1), Fe/Zeolite@CCNF(2), Fe/Zeolite/CNT@CCNC(3), and Fe/Zeolite/CNT@CCNF(4), were prepared as follows: 1 mg of the respective catalytic material was mixed with a solution consisting of DI water, isopropanol, ethanol, and Nafion® in a ratio of 1:1:3:0.1. These mixtures were then homogenized using ultrasound for a duration of 1 hour.

Subsequently, the prepared catalyst inks were applied to a cleaned glassy carbon electrode, with loadings of approximately 0.3 mg/cm2 for commercial RuO2 and 1 mg/cm2 for the iron-based catalysts. The modified electrodes were allowed to air-dry at room temperature for a period of 30 minutes.

Electrochemical assessment of the Oxygen Evolution Reaction (OER) was carried out by utilizing the inked glassy carbon electrode. The electrode was submerged in a 0.1 M KOH solution that had been purged with N2 for 10 minutes. The electrochemical potential was swept within a range of -200 to 1100 mV vs. 4MKCl/Ag/AgCl/ at a scan rate of 10 mV/s, facilitating the assessment of OER performance under these controlled conditions.

5.3. Results and discussion.

In this study, two distinct sets of materials were synthesized, each incorporating different types of nanocellulose, specifically nanocellulose nanocrystals and nanofibrils. These materials were designed to encapsulate iron nanoparticles within their carbon structures. Subsequently, an additional set of materials was synthesized by incorporating multi-walled carbon nanotubes into the previously mentioned composites.

Previous research has demonstrated that the inclusion of carbon nanotubes can significantly enhance the electrical conductivity of materials, as evidenced in several studies[261],[262],[263],[264]. This increase in conductivity can lead to an improvement in the onset potential for the oxygen evolution reaction (OER), a critical parameter in catalytic OER processes[265],[266].

The primary objective of this study is to thoroughly investigate the electrochemical properties of the resulting nanocellulose-based composite materials. Specifically, the focus is on assessing their potential applicability as catalysts for the OER. The detailed synthesis procedures and characterization techniques presented in this work are intended to provide valuable insights into the feasibility of using earth-abundant metal catalysts for OER, thus contributing to advancements in sustainable energy conversion technologies.

5.3.1. Analysis by XPS.

The comprehensive characterization of the nanocatalyst involved a thorough assessment of its elemental composition and chemical states using X-ray photoelectron spectroscopy (XPS). XPS is a highly sensitive technique capable of providing valuable insights into the surface chemistry of materials. In the XPS analysis, binding energy measurements were conducted, which yielded qualitative information about the presence of specific elements and their chemical states within the synthesized catalyst samples. This analysis served the dual purpose of confirming the presence of the targeted elements while ensuring the absence of any unintended or extraneous elements in the nanocatalyst.

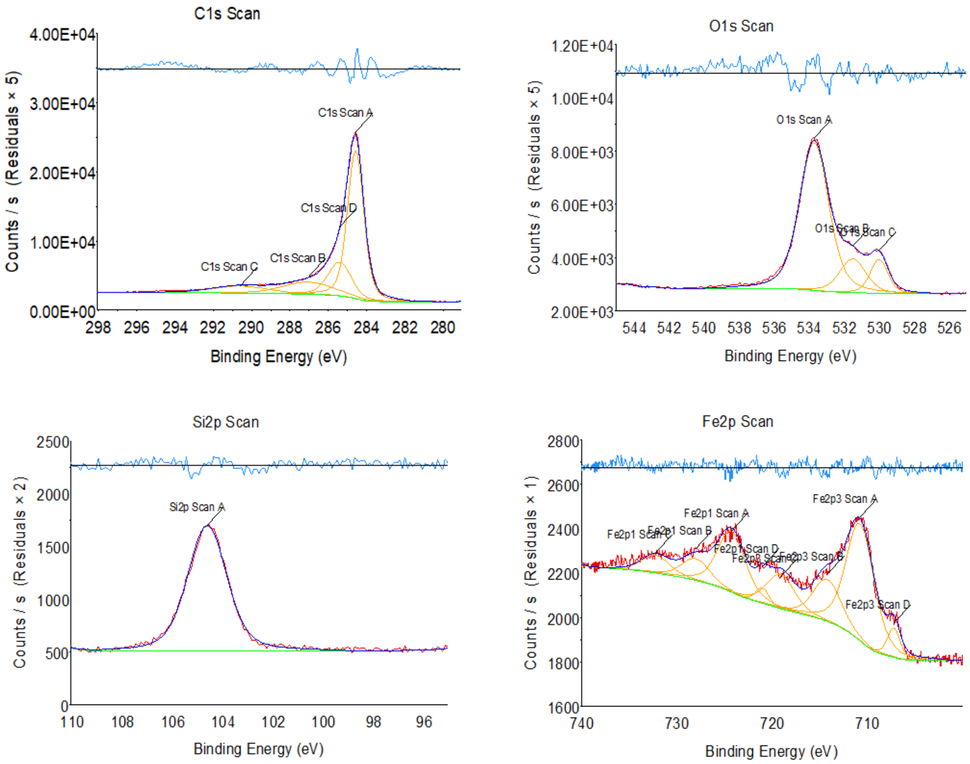

Figure 5.1: X-ray Photoelectron spectroscopy (XPS) of nanomaterial, the binding energy of Fe/Zeolite@CCNC (1)

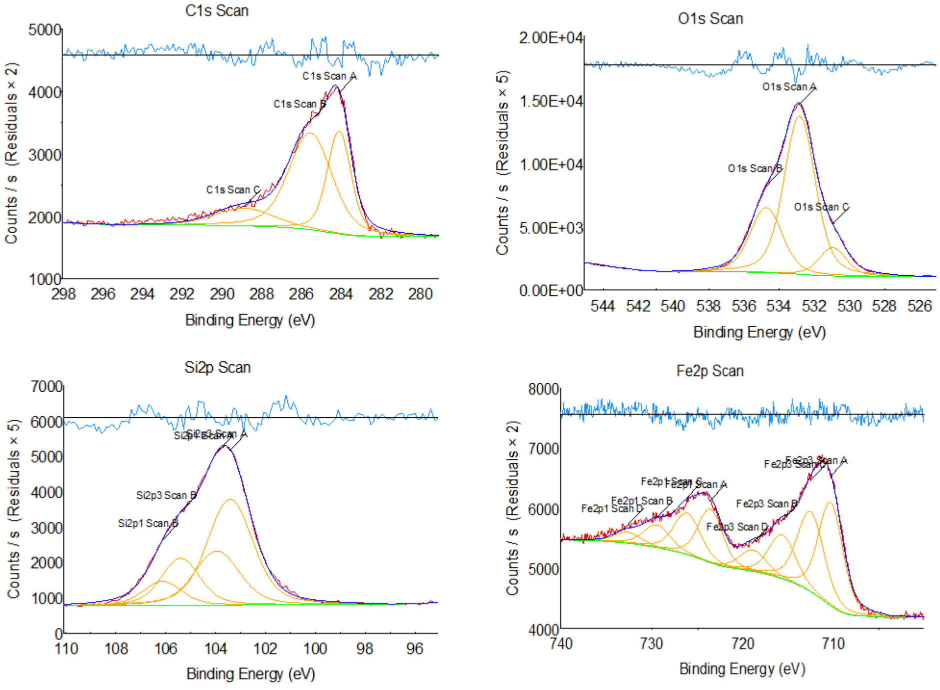

Figure 5.2: X-ray Photoelectron spectroscopy (XPS) of nanomaterial, the binding energy of Fe/Zeolite@CCNF (2).

Figures 5.1 and 5.2, presented herein, showcases the binding energies characteristic of iron and iron oxide, as identified through XPS analysis. These distinct binding energies align with the expected elemental composition of the nanocatalyst, corroborating the successful synthesis of the intended material. This initial characterization step provides a solid foundation for subsequent investigations into the electrocatalytic performance of the nanocatalyst, positioning it as a viable candidate for applications in oxygen evolution reactions and other catalytic processes.

5.3.2. Morphological analysis by TEM.

The nanocatalyst's morphology and nanostructure were subjected to a comprehensive examination using transmission electron microscopy (TEM), a powerful tool for visualizing materials at the nanoscale. In Figure 5.3a, a representative TEM image of the nanocatalyst is presented, revealing spherical metallic nanoparticles with a size distribution ranging from 10 to 20 nm. Of particular significance is the observation that all metallic nanoparticles are fully encapsulated within the carbon matrix. This encapsulation ensures that the nanoparticles remain securely embedded within the structure, mitigating the risk of nanoparticle leaching from the catalyst. The prevention of leaching is a crucial property, as it contributes to the long-term stability and effectiveness of the catalyst.

This observation is further substantiated by the control sample depicted in Figure 5.3c. In this control sample, which lacks metallic nanoparticles, the composition consists solely of zeolite and nanocellulose nanocrystals forming the carbon matrix. The clear absence of unbound nanoparticles in both the TEM image and the control sample underscores the success of the encapsulation process and reinforces the desired property of preventing nanoparticle leaching from the catalyst structure.

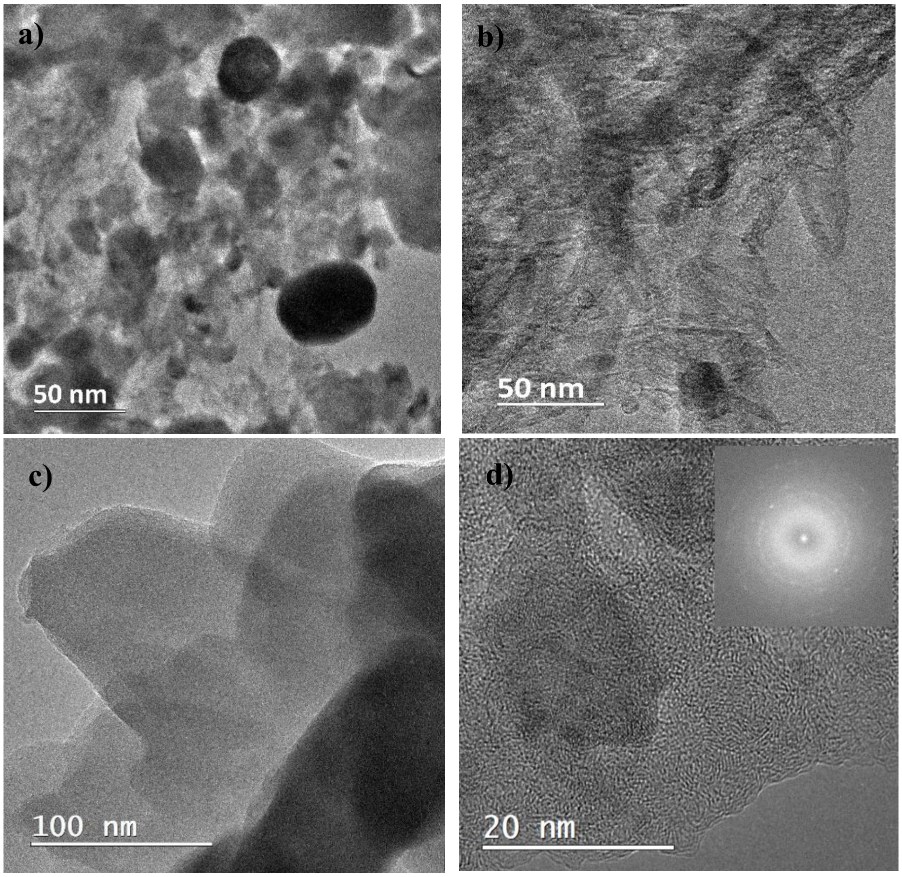

Figure 5.3: Transmission electron microscopy (TEM) of Fe/Zeolite@CCNC (1), Fe/Zeolite/CNT@CCNC (3), control sample (nanocellulose + zeolite), and HRTEM of Fe/Zeolite@CCNC (1) along with its diffraction pattern.

To gain deeper insights into the interconnectivity of the nanocatalyst components, a high-resolution transmission electron microscopy (HRTEM) analysis was conducted. Figure 5.3b showcases the intriguing presence of carbon nanotubes acting as interconnecting structures among the metallic nanoparticles within the carbon matrix. These carbon nanotubes were found to be evenly dispersed throughout the entire nanocatalyst, exhibiting an average size of approximately 2 nm. Furthermore, Figure 5.3d provides a high-resolution TEM representation of the Fe/Zeolite@CCNC(1) sample. In this image, clear diffraction lines corresponding to different planes of Fayalite (Fe2O4Si1) and Fe1Al1 were observed. These observations underscore the robust interconnection between the zeolite, serving as a solid support, and the metallic nanoparticles generated during the baking process. This structural integrity and interconnectivity contribute to the overall stability and functionality of the nanocatalyst, making it a promising candidate for various catalytic applications, particularly in oxygen evolution reactions and other electrocatalytic processes.

Collectively, the TEM and HRTEM observations offer crucial insights into the morphology and nanostructure of the synthesized nanocatalyst. These observations confirm several key features, including the presence of a highly interconnected carbon matrix, the absence of unbound metallic nanoparticles, and the notable presence of carbon nanotubes serving as interconnecting structures among the metallic nanoparticles. These findings not only reinforce the successful encapsulation of metallic nanoparticles within the carbon matrix but also highlight the structural integrity and interconnectivity of the nanocatalyst. These attributes are pivotal for ensuring long-term stability and catalytic efficiency. In conclusion, the TEM and HRTEM analyses provide a solid foundation for further research and underscore the substantial potential of this nanocatalyst for a range of electrocatalytic applications. The observed nanostructural characteristics align with the desired properties for effective and durable catalysis, particularly in applications such as oxygen evolution reactions and other electrochemical processes.

5.3.3. Morphological analysis by SEM.

To gain a more precise understanding of the surface morphology of the synthesized nanomaterial, Scanning Electron Microscopy (SEM) was employed as a characterization technique. Figure 5.4 presents SEM images of the synthesized nanomaterial, captured at a magnification of 50.0 μm, using a backscattering electron beam with a potential energy of 10.0 kV. The SEM images reveal several important features of the nanomaterial's surface. First, both the nanocellulose nanocrystal and nanocellulose nanofibrils-based samples exhibit a porous structure on their surfaces. This porous structure is characteristic of carbon matrices of this type and contributes to the material's high absorbent properties. It is an advantageous feature for various applications, including those requiring efficient absorption of substances.

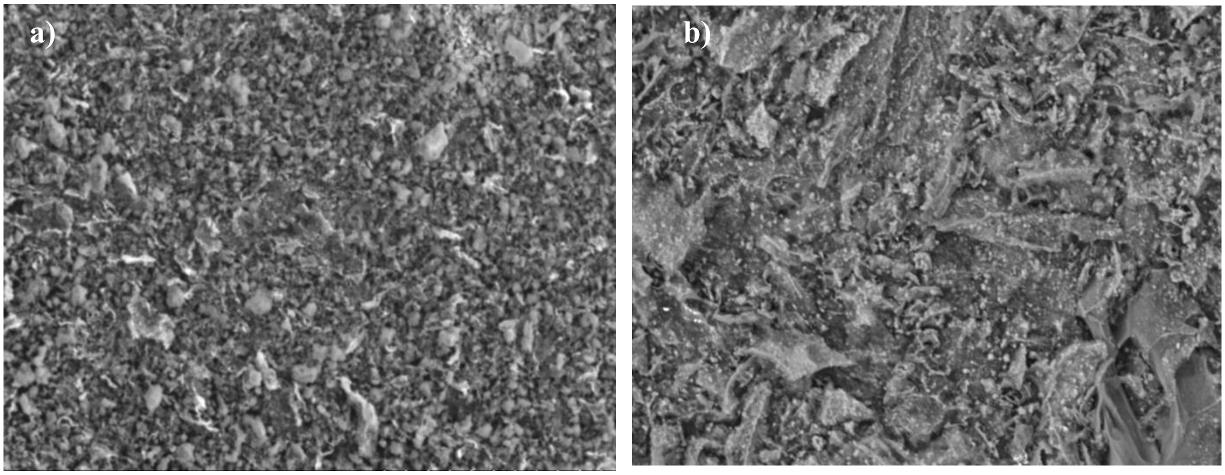

Figure 5.4: Scanning electron microscopy (SEM) of a) Fe/Zeolite@CCNF (2) and b) Fe/Zeolite@CCNC (1).

Additionally, the SEM images suggest that the nanomaterial exhibits a high level of electric conductivity. The observed conductivity is a vital attribute, particularly in electrocatalytic applications, as it enables efficient electron transfer during catalytic reactions. These detailed surface morphology observations provide valuable insights into the nanomaterial's properties and functionality, affirming its potential for various applications, including catalysis and energy-related processes.

5.3.4. EDS elemental analysis and color mapping.

The nanocatalyst's elemental analysis and color mapping were conducted using Energy-dispersed X-ray spectroscopy (EDS). The results obtained from this characterization technique, displayed in Figure 5.5, align with the qualitative elemental composition previously determined by X-ray Photoelectron Spectroscopy (XPS).

Predominantly, the primary element present in the sample was carbon, constituting the entire matrix that enveloped the iron particles. Additionally, the elemental analysis through EDS unveiled the presence of metallic iron and iron oxide, albeit in varying percentages. These findings substantiate the successful encapsulation of iron nanoparticles within the carbon matrix. Furthermore, the EDS analysis detected the presence of silicon and traces of aluminum. These elements are attributed to the original Zeolite material used in the synthesis process of the nanomaterial, demonstrating the incorporation of the solid support into the final composition of the nanocatalyst. In summary, the EDS results provide further evidence of the effective synthesis of the desired nanocatalyst and offer valuable insights into its chemical composition, confirming the presence of essential elements while accounting for the contribution of the initial Zeolite support material.

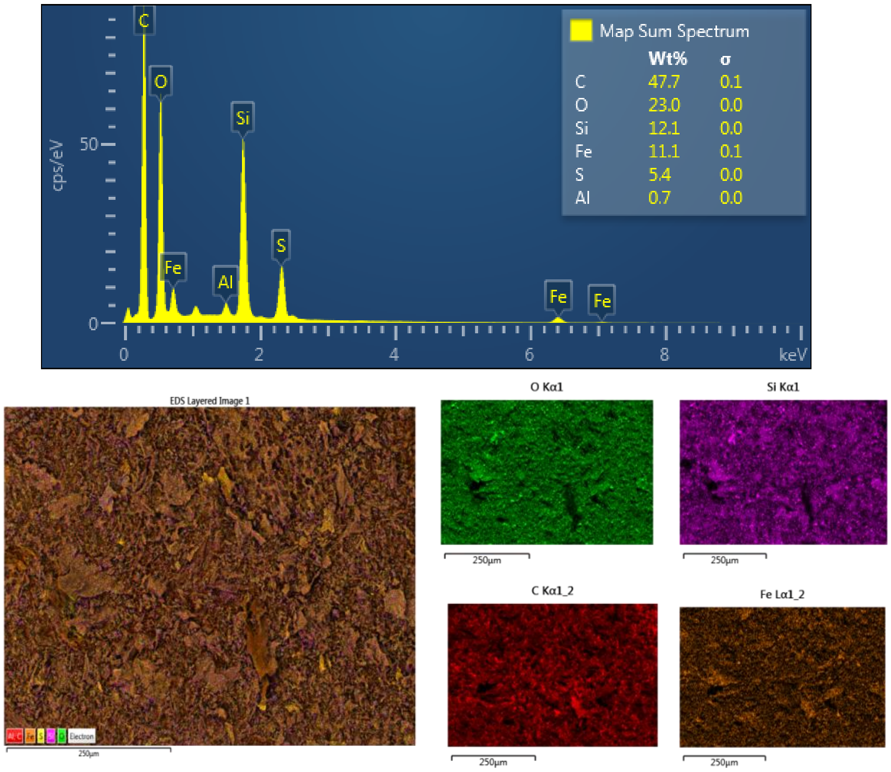

Map Sum Spectrum

	Wt%	σ
C	47.7	0.1
O	23.0	0.0
Si	12.1	0.0
Fe	11.1	0.1
S	5.4	0.0
Al	0.7	0.0

Figure 5.5: Elemental analysis and color mapping using Energy dispersed X-ray spectroscopy of Fe/Zeolite@CCNC (1).

5.3.5. Analysis of Crystalline Structure by XRD.

The PXRD (Powder X-ray Diffraction) results are pivotal in shedding light on the crystal structure of the nanomaterial. In this particular case, the PXRD pattern reveals the presence of zeolite SZM 5, an essential constituent of the Fe/Zeolite@CCNC(1) material. The crystallographic information extracted from the PXRD pattern provides valuable insights into the arrangement of atoms within the material.

Specifically, the identification of the orthorhombic crystal system and the recognition of distinct planes, such as (110) and (511), strongly indicate the presence of well-organized zeolite crystals within the sample. The presence of ordered crystal planes in the PXRD pattern is indicative of the crystalline nature of the zeolite component. Furthermore, a notable signal at 44.9° confirms the existence of metallic iron within the nanomaterial. This signal is associated with a cubic crystal system, with the (011) plane being the most prominent reflection. This observation provides strong evidence for the encapsulation of metallic iron nanoparticles within the carbon matrix, reinforcing the nanomaterial's structural integrity.

Figure 5.6 presents the PXRD (Powder X-ray Diffraction) pattern for the Fe/Zeolite@CCNF(2) nanomaterial, which reveals the presence of zeolite as well as iron oxide, specifically hematite and fayalite. The identified signals at 33.7° and 54.9° are indicative of the presence of hematite, which adopts a hexagonal crystal system. These signals correspond to the (104) and (116) planes, respectively, according to Miller's Index notation. Additionally, the PXRD pattern displays signals at 34.8° and 35.7°, which are attributed to the presence of fayalite. Fayalite exhibits an orthorhombic crystal system, and these signals correspond to the (311) and (121) planes, respectively, as per Miller's Index notation.

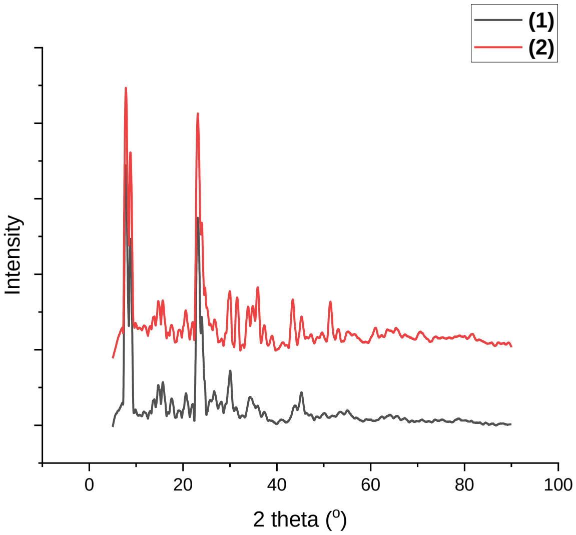

Figure 5.6: Powder X-Ray diffraction of a) Comp #1 (Fe/Zeolite@CCNC(1)) and b) Comp#2 (Fe/Zeolite@CCNF(2)).

These findings provide a comprehensive understanding of the crystallographic characteristics of the Fe/Zeolite@C_{CNF}(2) nanomaterial, highlighting the presence of both zeolite and iron oxide phases with distinct crystal structures. These understandings of the material's composition and crystallography are invaluable for assessing its suitability for various applications, particularly in catalytic and materials science research.

Furthermore, the PXRD analysis detected the presence of iron-aluminum (Fe1Al1) at approximately 43.0°, consistent with its cubic crystal system. These PXRD results align harmoniously with the findings from other characterization techniques employed in this study, notably with the interplanar distances observed in HRTEM images. An intriguing observation is that the two compounds, Fe/Zeolite@CCNC(1) and Fe/Zeolite@CCNF(2), exhibit distinct iron environments. Both compounds contain a notable content of fayalite. However, the Fe/Zeolite@CCNC(1) material displays higher percentages of hematite and iron-aluminum. This variation in iron environments among the two compounds underscores the importance of precise control over synthesis processes to achieve tailored material properties.

In summary, these PXRD results provide valuable information about the crystal structures and phases present in the nanomaterials, corroborating the findings from other characterization methods employed in the study. The differences in iron environments between the two compounds highlight the potential for fine-tuning material compositions to suit specific applications, further emphasizing the versatility and potential of these nanocellulose-based composites in various research fields. Overall, the PXRD results complement the insights gained from XPS and TEM analyses, collectively offering a comprehensive characterization of the nanomaterial's elemental and crystal structure. These combined findings underscore the nanocatalyst's suitability for diverse applications, particularly in the domains of catalysis and energy conversion.

5.3.6. Raman Analysis.

The degree of graphitization and defect level in the synthesized nanomaterial were thoroughly investigated through Raman spectroscopic characterization. The resulting findings are presented in Figure 5.7, displaying two distinctive sets of spectra for the Fe/Zeolite@CCNC(1) and Fe/Zeolite@CCNF(2) nanomaterials. In both cases, the Raman spectra exhibits two prominent peaks. For the Fe/Zeolite@CCNC(1) material, these peaks occur at approximately 1588 cm^{-1} and 1338 cm^{-1}, corresponding to the G (graphite) and D (defects and disorder) bands, respectively. Conversely, the Fe/Zeolite@CCNF(2) nanomaterial shows peaks at around 1590 cm^{-1} and 1371 cm^{-1}, also attributed to the G and D bands, respectively.

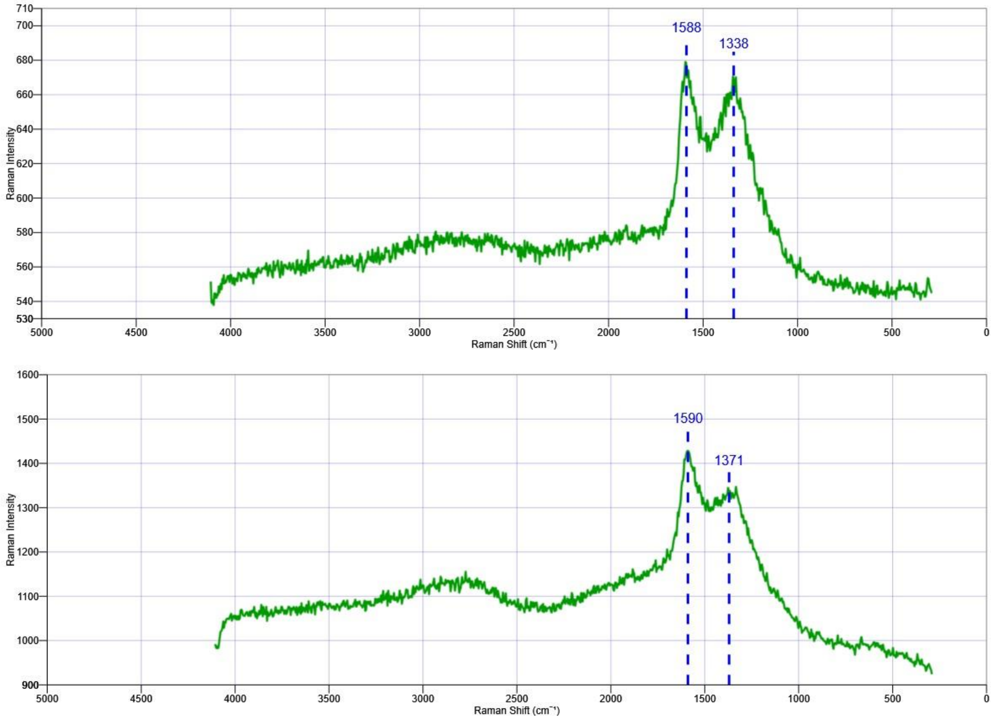

Figure 5.7: Raman spectra for Fe/Zeolite@CCNC(1) a) and for Fe/Zeolite@CCNF(2) b).

These Raman spectroscopic results are indicative of the graphitization degree and defect levels within the nanocatalyst materials. The presence and characteristics of the G and D bands provide insights into the carbon structure, including the arrangement of carbon atoms and the presence of defects and disorder. These findings contribute to a comprehensive understanding of the nanomaterial's structural properties, which are crucial for its performance in various applications, particularly in catalysis and materials science research.

The Raman peaks observed in the nanocatalyst spectra are characteristic of carbon-based composites. Specifically, the G band corresponds to the E2g vibration mode of sp2-hybridized carbon, indicating the presence of graphitic carbon, while the D band signifies structural disorder or defects in the carbon lattice.

The ID/IG ratio is a critical parameter used to assess the degree of crystallization of graphitic carbon in the nanocatalyst. A higher ID/IG ratio implies a greater degree of graphitization, while a lower ratio suggests a higher number of defect sites in the carbon structure. In the nanocatalyst's Raman spectra, the D band's intensity is lower than that of the G band. This observation indicates the presence of sp2-hybridized carbon species within the graphitized pore walls, indicative of a high degree of graphitization.

The ID/IG values for the Fe/Zeolite@CCNC(1) and Fe/Zeolite@CCNF(2) nanomaterials are measured at 0.98 and 0.95, respectively. These values suggest the formation of high-quality three-dimensional graphitic carbon structures, which are comparable to those typically found in reduced graphene oxide (with an ID/IG ratio of approximately 1). Consequently, the nanocatalyst demonstrates a high degree of graphitization with some levels of structural defects. These characteristics have the potential to enhance catalytic activity, making the nanocatalyst a promising candidate for various applications, particularly in catalysis and electrocatalysis, where well-defined carbon structures with defects can significantly influence performance.

5.3.7. Catalytic activity for Oxygen Evolution Reaction (OER).

The Oxygen Evolution Reaction (OER) experiments were conducted using four different nanocatalysts synthesized in this study: Fe/Zeolite@CCNC(1), Fe/Zeolite@CCNF(2), Fe/Zeolite/CNT@CCNC(3), and Fe/Zeolite/CNT@CCNF(4). Linear sweep voltammetry was employed to investigate their OER performance, and Figure 8 presents the corresponding results, alongside a reference catalyst, RuO2.

These experiments were carried out in a 10-minute N2-purged 0.1 M KOH solution at a rotation speed of 1600 rpm. The potential was swept within a range of -200 to 1100 mV vs.

4MKCl/Ag/AgCl/ at a scan rate of 10 mV/s. The obtained voltammetry data provide valuable insights into the catalytic activity of the different nanocatalysts for the OER, enabling a comparison with the benchmark RuO2 catalyst.

The outcomes of these experiments will provide insights into the electrocatalytic performance of the synthesized nanocatalysts, potentially revealing their suitability for various applications, particularly in renewable energy technologies and electrochemical processes. In Table 5.1, a comprehensive overview of the Oxygen Evolution Reaction (OER) performance metrics is provided for each of the tested catalyst materials. This includes OER onset potentials (Eonset), potentials required to reach a current density of 10 mA/cm2, and the corresponding overpotentials. All potentials are standardized to the Reversible Hydrogen Electrode (RHE). For the materials investigated, the following OER onset potentials were observed: RuO2 exhibited an Eonset of 1.578 V vs. RHE, Fe/Zeolite@CCNC(1) 1.671 V, Fe/Zeolite@CCNF(2 1.654 V, Fe/Zeolite/CNT@CCNC(3) 1.757 V, and Fe/Zeolite/CNT@CCNF(4) 1.724 V vs. RHE respectively.

Remarkably, the addition of carbon nanotubes (CNT) to Fe/Zeolite@CCNC(3) and Fe/Zeolite@CCNF(4) led to improved catalytic activity, resulting in lower Eonset values. Particularly noteworthy was the significant reduction in Eonset from 1.757 V vs. RHE for Fe/Zeolite@CCNF(2) to 1.724 V for Fe/Zeolite/CNT@CCNF(4), indicating enhanced performance. Among all the catalysts tested, Fe/Zeolite/CNT@CCNC(3) exhibited the most favorable OER performance with an Eonset of 1.757 V vs. RHE, corresponding to an overpotential of 76 mV relative to the RuO2-Eonset. Additionally, in terms of potentials required to reach a current density of 10 mA/cm2, Fe/Zeolite/CNT@CCNC(3) outperformed RuO2, requiring a lower potential of 1.78 V vs. RHE compared to RuO2's 1.791 V vs. RHE. It's worth noting that Fe/Zeolite@CCNC(1) achieved a similar potential of 1.791 V vs. RHE as the commercial RuO2 catalyst, highlighting its promising electrocatalytic performance.

RuO2 has long been considered a benchmark catalyst for electrochemical water oxidation due to its efficiency. However, it still demands a relatively high overpotential of 213 mV to achieve a current density of 10 mA/cm2, a critical requirement for efficient solar-to-fuels conversion devices operating under AM1.5G illumination conditions. In contrast, both Fe/Zeolite@CCNC(1) and Fe/Zeolite/CNT@CCNC(3) catalysts exhibited significantly lower energy requirements, with overpotentials of only 120 and 127 mV vs. RHE, respectively, to achieve the same 10 mA/cm2 current density. This notable reduction in overpotential suggests that iron-carbon compounds hold great promise as materials for energy conversion and electrochemical applications.

The competitive onset potentials, relative activity, and favorable overpotentials observed for Fe/Zeolite@CCNC(1) and Fe/Zeolite/CNT@CCNC(3) underscore their potential as effective catalysts for the Oxygen Evolution Reaction (OER). These findings indicate that these catalysts may outperform the benchmark RuO2 in specific applications. Additional investigations would evaluate the extended-term stability and robustness of these catalysts and to explore methods for further enhancing their performance. These efforts aim to unlock the full potential of Fe/Zeolite@CCNC(1) and Fe/Zeolite/CNT@CCNC(3) in sustainable energy technologies, making them even more attractive for practical implementation.

Table 5.1: OER Onset potentials, potentials at 10 mA/cm2 and overpotentials to reach 10 mA/cm2 for RuO2, Fe/Zeolite@CCNC(1), Comp2, Fe/Zeolite/CNT@CCNC(3), Fe/Zeolite/CNT@CCNF(4) catalysts.

Catalyst	Onset Potential (±0.001 V vs. RHE)	Potential at 10 mA/cm^2(±0.001 V vs. RHE)	Overpotential at 10 mA/cm^2 (±1 mV vs. RHE)
RuO$_2$	1.578	1.791	213
Fe/Zeolite@C$_{CNC}$**(1)**	1.671	1.791	120
Fe/Zeolite/CNT@C$_{CNC}$**(3)**	1.654	1.781	127
Fe/Zeolite@C$_{CNF}$**(2)**	1.757	2.010	253
Fe/Zeolite/CNT@C$_{CNF}$**(4)**	1.724	1.900	176

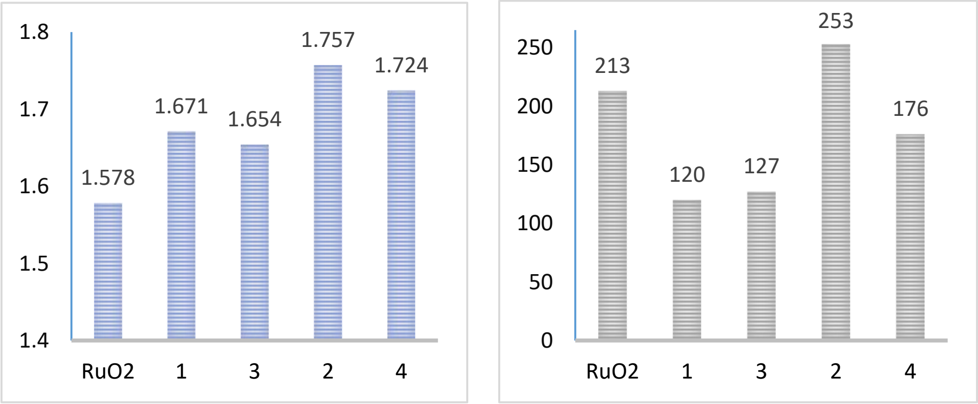

Figure 5.8: Onset Potential (V) of different materials synthesized vs RuO2 (a) and Overpotential (mV) of different materials synthesized vs RuO2 (b).

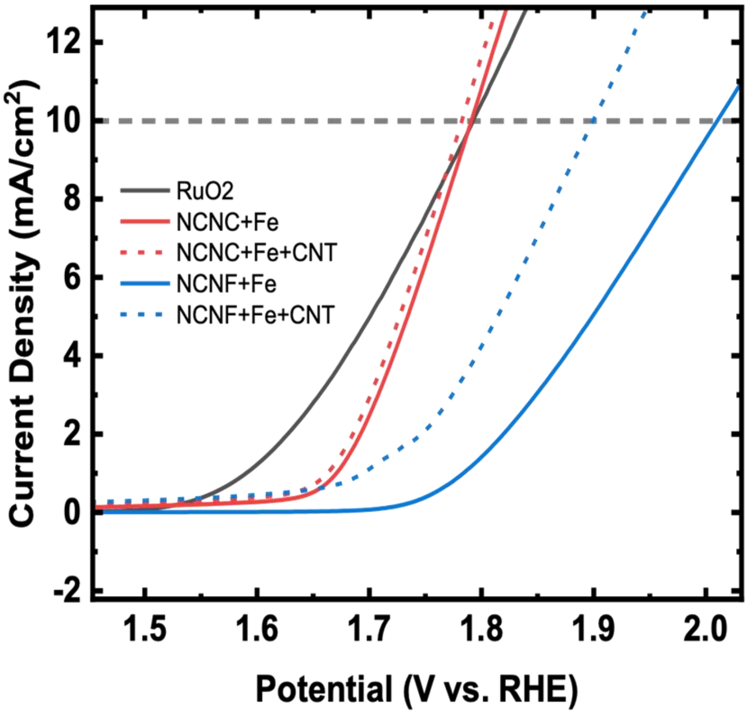

Figure 5.9: OER polarization of commercial powder RuO2, Fe/Zeolite@CCNC(1), Fe/Zeolite@CCNF(2), Fe/Zeolite/CNT@CCNC(3), Fe/Zeolite/CNT@CCNF(4) catalysts in 0.1M KOH at 1600 rpm.

5.4. Conclusions

In summary, this study introduces a novel class of highly efficient nanocatalysts designed specifically for the electrochemical water oxidation reaction (OER). The unique approach of utilizing biocarbon derived from nanocellulose, combined with the strategic incorporation of Fe-zeolite and carbon nanotubes (CNTs) into the composite, has led to substantial enhancements in catalytic activity. Notably, the composite derived from nanocellulose nanocrystals and CNTs has exhibited exceptional OER catalytic performance, characterized by an onset potential nearly matching that of the benchmark material RuO2, while demonstrating an even lower overpotential at 10 mA/cm2.

What makes these nanocatalysts particularly attractive is their synthesis process, which is both straightforward and environmentally friendly. Furthermore, this process relies on the use of abundant and cost-effective iron, distinguishing it from catalysts based on precious metals like Ru, Ir, and Pt. This cost advantage positions the material as a compelling and sustainable alternative for OER applications.

To provide a comprehensive understanding of these nanomaterials, an array of advanced spectroscopic techniques was employed, including TEM, SEM-EDS, PXRD, and XPS. These techniques shed light on the structural and chemical properties of the composite, offering invaluable insights into its outstanding catalytic performance.

The study's results suggest that harnessing biocarbon and incorporating CNTs within the nanocomposite plays a pivotal role in enhancing conductivity and fostering improved connectivity among metallic particles. This synergy ultimately leads to heightened electrocatalytic activity for OER. These findings not only have immediate implications for the development of more efficient and cost-effective OER catalysts but also open up exciting prospects for biocarbon-based nanocatalysts in various energy and electrochemical applications.

In a broader context, this study not only presents a groundbreaking approach to catalysis but also highlights the immense potential inherent in these materials. It emphasizes their effectiveness, affordability, and sustainability, signifying a significant achievement on the path to a long-lasting and environmentally sustainable energy future. These catalysts embody the potential to transform the realm of energy conversion and storage technologies while offering solutions to pressing environmental and economic challenges. As a result, this research serves as a guiding light, illuminating the path towards the development of efficient, accessible, and environmentally friendly catalysts for the oxygen evolution reaction (OER), ultimately making substantial contributions to the advancement of sustainable energy solutions.

Chapter 6: Nanoparticle-templated diyne photopolymerization of a covalent organic framework as a solid support for nanoparticles.

6.1. Introduction

Nanoparticles possess unique properties that are strongly influenced by their size, shape, and chemical composition[267,268]. For example, gold nanoparticles (AuNPs) show unique optical properties that are influenced by their dimensions and morphology[269]. This variability allows for the creation of nanomaterials with tailored properties, making them highly valuable in fields such as biosensing[270,271,272], catalysis[273,274,275] , and drug delivery[276,277,278].

The ability to predict and precisely control the size and morphology of nanoparticles are critical for developing nanomaterials with consistent and desired properties. Among the various methods used to synthesize AuNPs, template-based approaches have shown promise in achieving this control[279,280,281]. Specifically, soft templates like micelles[282,283] and surfactants[284,285] have been explored because of their ability to influence the size of metal and inorganic nanoparticles during synthesis. However, a notable challenge with soft-template methods is ensuring monodispersity, which means achieving nanoparticles with nearly uniform sizes. Monodispersity is essential for many applications because it ensures that the nanoparticles perform consistently and predictably. In summary, while soft templates offer control over nanoparticle size, achieving monodispersity remains a critical goal in nanomaterial synthesis.

In recent years, there has been a surge in research focusing on various types of porous materials, with particular attention given to metal-organic frameworks (MOFs)[286,287,288], covalent organic frameworks (COFs)[289,290,291], and other microporous organic polymers[292]. COFs, in particular, have gained prominence as an exciting category of porous organic materials due to their unique structure and properties. These frameworks are constructed by forming strong covalent bonds between organic building blocks, resulting in well-defined and highly ordered porous structures.

The versatility of COFs has led to their application in a wide range of fields. They have been effectively used for tasks such as selectively removing heavy metals from aqueous solutions, demonstrating their potential in environmental remediation. Additionally, COFs have been employed in the development of sensitive sensing technologies, where their porous nature allows for efficient analyte capture and detection[293,294,295,296]. Furthermore, COFs have shown promise in gas storage applications, offering a means to store and release gases like hydrogen and methane for various industrial and energy-related purposes. Their inherent porosity and stability make them suitable candidates for gas adsorption and storage[297,298].

In the realm of catalysis, COFs have exhibited catalytic activity in a variety of reactions. Their well-defined structures and tunable properties enable researchers to design COFs with specific catalytic functionalities, making them valuable in catalytic processes[299,300,301]. Moreover, COFs have been utilized as nanoreactors, providing confined spaces for chemical reactions to occur with enhanced control and selectivity[302]. This property opens up exciting possibilities for designing and optimizing chemical transformations within the framework's pores. The versatility and unique properties of covalent organic frameworks (COFs) have led to their widespread exploration in diverse scientific and industrial applications, spanning environmental remediation, sensing, gas storage, catalysis, and even as nanoreactors for controlled chemical reactions. These materials continue to be an area of active research with promising potential for addressing various technological challenges.

Covalent organic frameworks (COFs) are synthesized through a series of chemical reactions involving various organic building blocks. These reactions include boronic acid trimerization[303,304], boronate ester formation[305,306], nitrile trimerization[307,308], Schiff base reaction[309,310], and nitroso self-addition[311]. Each of these reactions results in the formation of covalent bonds between the organic building units, leading to the creation of the COF structure.

One of the challenges in COF synthesis is related to the dimensionality of the resulting frameworks. While significant progress has been made in producing two-dimensional (2D) COFs with layered structures, the synthesis of three-dimensional (3D) COFs remains a formidable task. Designing and synthesizing 3D COFs are complex processes that require precise control over reaction conditions and the selection of suitable organic precursors. Additionally, characterizing the 3D COF structures is challenging due to their intricate nature. Despite these challenges, researchers are actively exploring methods to create 3D COFs, as these materials have the potential to exhibit unique properties and find applications in various fields. The development of new synthetic strategies and the structural elucidation of 3D COFs represent exciting avenues of research in the field of porous materials.

Diynes are organic compounds characterized by having two consecutive triple bonds (-C≡C-C≡C-) in their molecular structure. These compounds belong to the class of alkynes, which are hydrocarbons containing carbon-carbon triple bonds. Diynes, with their two triple bonds, are sometimes referred to as "diacetylenes" due to the similarity of their structure to acetylene, which has a single carbon-carbon triple bond. One notable feature of diynes is their linear and rod-like molecular shape, which imparts rigidity and stability to their structure. This rigidity makes diynes thermally and moisture stable, allowing them to withstand harsh environmental conditions.

Among diynes, 1,3-diynes have received significant attention in the field of chemistry. When exposed to ultraviolet (UV) light, 1,3-diynes have the unique ability to undergo polymerization. During this process, covalent bonds form between adjacent carbon atoms within the diyne molecules, leading to crosslinking between different carbon chains. This results in the formation of polydiacetylenes. Polydiacetylenes exhibit fascinating optical and electronic properties, making them valuable in various applications. They are known for their ability to undergo color changes in response to environmental stimuli, such as changes in temperature, pressure, or chemical interactions. This color-changing property has led to their use in sensor technologies[312].

Diynes are characterized by their linear, rigid, and stable structure, with 1,3-diynes having the remarkable ability to polymerize upon UV light exposure, forming polydiacetylenes. These polydiacetylenes possess unique optical properties and find applications in sensors and optoelectronic devices, highlighting the importance of diynes in the development of innovative materials and technologies[313].

The oxygen evolution reaction (OER) is a fundamental process involved in various chemical reactions aimed at producing molecular oxygen. This reaction has significant implications in numerous essential functions, including the oxidation of water during oxygenic photosynthesis, the electrolysis of water to generate oxygen and hydrogen, and the electrocatalytic production of oxygen from oxides and oxoacids. Enhancing the efficiency of catalysts for OER is a crucial objective in advancing various renewable energy technologies. These technologies include the production of solar fuels and the utilization of metal-air batteries.

Traditionally, precious metal oxides like ruthenium and iridium oxides have demonstrated the highest OER activities. However, their limited availability and high production costs make them less suitable for widespread and scalable applications. Therefore, the scientific community is actively exploring more cost-effective alternatives composed of transition metal compounds. These alternatives aim to provide efficient and sustainable catalysts for OER, contributing to the development of environmentally friendly and economically viable energy solutions.

6.2. Materials and Methods.

6.2.1. Chemicals and Reagents.

All of the chemicals used in this study were employed as received without the need for additional purification. The copper diacetate monohydrate ($Cu(OAc)_2.H_2O$) (ACS reagent, ≥98.0%), cobalt acetate tetrahydrate ($Co(OAc)_2.4H_2O$) (ACS Reagent ≥98.0%), 2,4-Hexadiyn-1,6-diol (97%), potassium hydroxide (KOH ≥ 98%), Sodium rhodizonate dibasic ($C_6Na_2O_6$) (97%), bromoacetic acid (CH_2BrCO_2H) (Reagent Grade 97%), sodium hydride (NaH) (Dry 90%), sodium borohydride ($NaBH_4$) (powder, ≥98.0%), hydrogen tetrachloroaurate trihydrate ($HAuCl_4$ $.3H_2O$, 99.9%), palladium(II) nitrate dihydrate ($Pd(NO_3)_2.2H_2O$) (~40% Pd basis), Methanol (CH_3OH) (anhydrous, 99.8%), N,N dimethylformamide ($HCON(CH_3)_2$) (anhydrous, 99.8%), Benzyl bromide ($C_6H_5CH_2Br$) (reagent grade, 98%), dichloromethane (CH_2Cl_2) (contains 40-150 ppm amylene as stabilizer, ACS reagent, ≥99.5%), magnesium sulfate ($MgSO_4$) (anhydrous, ReagentPlus®, ≥99.5%), Hydrochloric acid (HCl) (ACS reagent, 37%) and Tetrahydrofuran (THF, C_4H_8O) (anhydrous, ≥99.9%, inhibitor-free) were purchased from Sigma-Aldrich. Deionized (DI) water (>18.20 MI cm resistivity) was used from the Milli-Q® instrument (Millipore Corporation).

6.2.2. Synthesis of 6-(benzyloxy)hexa-2,4-diyn-1-ol:

In a 100-mL round-bottomed flask equipped with a magnetic stirrer bar and oven-dried, 2,4-Hexadiyn-1,6-diol (1.0 g, 9.1 mmol, 4.0 equiv) was combined with an aqueous solution of KOH (10 mL, 510 mg, 9.1 mmol, 4.0 equiv). The flask was then sealed with a glass stopper and stirred at room temperature (RT) for 5 minutes. Subsequently, benzyl bromide (390 mg, 0.28 mL, 2.25 mmol, 1.0 equiv) was added dropwise using a syringe over a period of 2-3 minutes. The resulting mixture was allowed to stir at RT for 48 hours. After the reaction, the mixture was transferred to a separatory funnel and extracted with CH2Cl2 (3 × 15 mL). The combined organic extracts were washed with brine (10 mL), then dried using magnesium sulfate (MgSO4), filtered, and concentrated in vacuo at a temperature range of 20 - 23 °C and a vacuum pressure of approximately 20 mm Hg. This process yielded a pale-yellow oil with a percentage yield for the intermediate reaction of 30.1%.

6.2.3. Synthesis of {[6-(benzyloxy)hexa-2,4-diyn-1-yl] oxy} acetic acid:

In this step, the process involved the alcohol obtained in the previous step. It was dissolved in anhydrous THF (Tetrahydrofuran) and added gradually under a nitrogen (N2) atmosphere to a suspension of NaH in THF. The mixture was stirred until the evolution of hydrogen gas (H2) ceased. Afterward, a solution of bromoacetic acid in anhydrous THF was added to the suspension and stirring continued until a Thin Layer Chromatography (TLC) analysis indicated the complete disappearance of the alcohol. The addition of water (H2O) followed, and the solvent was concentrated under reduced pressure. The residue was dissolved in H2O, washed with ethyl acetate (EtOAc), and the aqueous phase was acidified with a solution of half-concentrated HCl (hydrochloric acid) to reach a pH of 1. It was then extracted with EtOAc.

The combined organic layers were dried over sodium sulfate (Na2SO4), filtered, and concentrated under vacuum to yield the final product with a percentage yield of 56.5%.

6.2.4. Preparation of Cu ligand.

In the next step, 100 mg (0.4 mmol, 2 equiv) of diynic acid was dissolved in 8 ml of methanol, and 40 mg (0.2 mmol, 1 equiv) of copper acetate monohydrate was added at room temperature. The mixture was stirred for 18 hours. Afterward, the solvent was removed by vacuum evaporation, leaving behind the crude compound for the subsequent step in the process.

6.2.5. Preparation of Co ligand.

The preparation of the Co ligand followed the same methodology as for the Cu ligand, but cobalt acetate tetrahydrate was used instead of copper acetate monohydrate.

6.2.6. Synthesis of PDA-Cu_2O nanoparticles.

In the initial step, Cu nanoparticles were synthesized using a chemical reduction method. The procedure involved dissolving the previously prepared copper ligand (40 mg, 0.07 mmol, 1 equiv) in a mixture of methanol and DMF (MeOH: DMF = 5:1). This mixture was then subjected to N2 bubbling for 15 minutes. Subsequently, sodium borohydride (NaBH4) (6.0 mg, 0.14 mmol, 2 equiv) was slowly added in portions at room temperature. During this process, the color of the mixture transitioned from blue to brown, indicating the precipitation of Cu nanoparticles. The reaction was carried out under a N2 atmosphere for 8 hours. The resulting Cu nanoparticles were separated via centrifugation, washed multiple times with a mixture of methanol and DMF, and finally dried under high vacuum. It's important to note that these Cu nanoparticles gradually oxidized over time, transforming into Cu2O nanoparticles upon exposure to air. . Finally, using AIBN as a photoinitiator, the material was photo-polymerized with UV light to obtain polydiacetylene-embedded copper(I) oxide nanoparticles PDA-Cu$_2$O NPs.

6.2.7. Synthesis of CoO nanoparticles.

The synthesis of CoO nanoparticles followed a similar methodology to that employed for Cu$_2$O nanoparticles, with the only variation being the utilization of a cobalt ligand instead of the copper ligand.

6.2.8. OER Experimental Methods.

The catalyst inks, including RuO2, PDA-Cu2O, and PDA-CoO, were prepared by mixing 1 mg of the respective catalytic material with a solution consisting of 1 mL of methanol and 30 µL of Nafion®. These mixtures were homogenized using ultrasound for 30 minutes. Following the preparation of the catalyst inks, they were applied to a cleaned glassy carbon electrode, with loadings of approximately 0.3 mg/cm2 for commercial RuO$_2$ and 1 mg/cm2 for Cu and Co catalysts. The modified electrodes were allowed to air-dry at room temperature for 30 minutes.

The electrochemical evaluation of the Oxygen Evolution Reaction (OER) was conducted using the inked glassy carbon electrode. The electrode was submerged in a 0.1 M KOH solution that had been purged with N2 for 10 minutes. The electrochemical potential was swept within a range of 200 to 1000 mV vs. 4MKCl/Ag/AgCl/ at a scan rate of 10 mV/s, enabling the assessment of OER performance under these controlled conditions.

6.2.9. Removal of Cu_2O nanoparticles.

To remove the Cu_2O nanoparticles and create cavities inside, the photopolymerized product underwent a treatment with 0.1 N HCl. The mixture was stirred at room temperature for 12 hours and later neutralized by adding 0.1 N NaOH solution. The final product was collected through centrifugation.

6.2.10. Preparation of Au NPs and Pd NPs using the PDA polymer.

In the process, 10 mg of nanotemplated PDA was added to an aqueous solution containing either HAuCl4 or Pd(NO3)2 (1 mmol in 5 mL of solution). This mixture was stirred at room temperature overnight. After allowing the metal salts to permeate the PDA polymer, the PDA material was separated via centrifugation, then resuspended in water. To this resuspended PDA, an aqueous solution of sodium rhodizonate (3.88 mmol in 5 mL of solution) was added. The resulting mixture was stirred at room temperature for 30 minutes, following which the PDA material with impregnated nanoparticles was again separated via centrifugation and subsequently dried under vacuum conditions.

6.3. Results and discussion.

In this study, we present the synthesis of a metal-coordinating diyne compound, specifically ([6-(benzyloxy)hexa-2,4-diyn-1-yl]oxy)acetic acid. This compound has the ability to coat copper (Cu) and cobalt (Co) nanoparticles. Upon photopolymerization, it forms a covalent organic framework (COF) that acts as a structural support for the generation of newly formed nanoparticles. This innovative approach was exemplified through the COF-templated growth of gold (Au) and palladium (Pd) nanoparticles, as illustrated in Scheme 6.1.

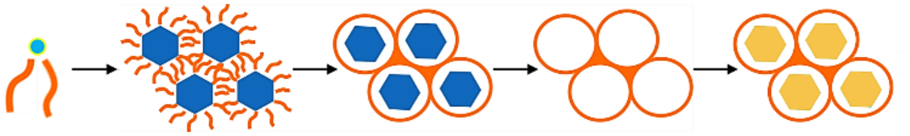

Scheme 6.1: NP-templated polydiacetylene COF cast formation.

The synthesis of polydiacetylene-embedded copper oxide nanoparticles (PDA-Cu2O NPs) involved a stepwise procedure, as depicted in Scheme 6.2. Initially, the process commenced with the utilization of 2,4-hexadiyn-1,6-diol, a symmetric dialkyne-diol molecule (1). To protect one of the alcohol groups, benzyl chloride was employed, leading to the formation of 6-(benzyloxy)hexa-2,4-diyn-1-ol (2). Subsequently, compound 2 was transformed into an ether through a reaction with bromoacetic acid, giving rise to {[6-(benzyloxy)hexa-2,4-diyn-1-yl]oxy}acetic acid (3). Compound (3) then underwent a reaction with copper acetate monohydrate salt, resulting in the copper complex (4). This complex was subsequently subjected to a reduction process, leading to the generation of copper nanoparticles (5), which were effectively stabilized by the ligand (3). Finally, the photo-polymerization of compound (5) was achieved by employing AIBN as a photoinitiator in the presence of UV light. This process yielded polydiacetylene-embedded copper(I) oxide nanoparticles, designated as PDA-Cu2O NPs (6).

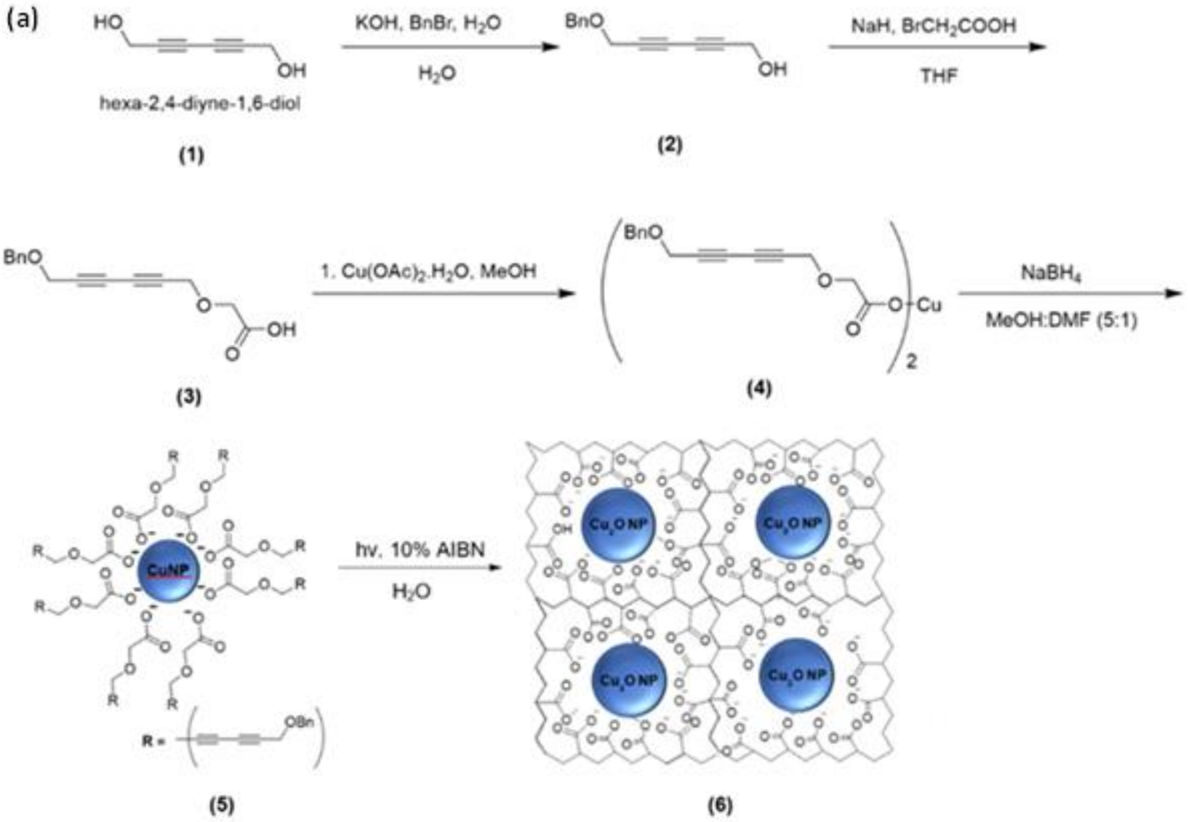

Scheme 6.2: NP-templated polydiacetylene COF cast formation.

The polydiacetylene (PDA) complex with copper oxide (Cu_2O) and cobalt ocyde (CoO) nanoparticles (NPs) displayed several noteworthy characteristics. These NPs were stable, maintaining their integrity and properties over time. They exhibited a spherical shape, suggesting uniformity in their structure, and were monodispersed within the solid polymer matrix. Furthermore, it was possible to selectively remove the copper component from these PDA-Cu_2O NPs through a treatment with hydrochloric acid (HCl). This process led to the creation of a microporous polydiacetylene metal-free covalent organic framework (COF). The removal of copper allowed the resulting COF to be free from metal components, making it an intriguing porous material for various applications.

The metal-free COF, in this case, served as a casting mold to facilitate the growth of new metallic nanoparticles composed of gold (Au) and palladium (Pd). The process involved treating the metal-free COF with solutions of HAuCl4 or Pd(NO3)2. Subsequently, sodium rhodizonate was introduced to the mixture to act as a reducing agent. This process resulted in the formation of polydiacetylene-embedded gold (8) and palladium (9) nanoparticles according to Scheme 5.3.

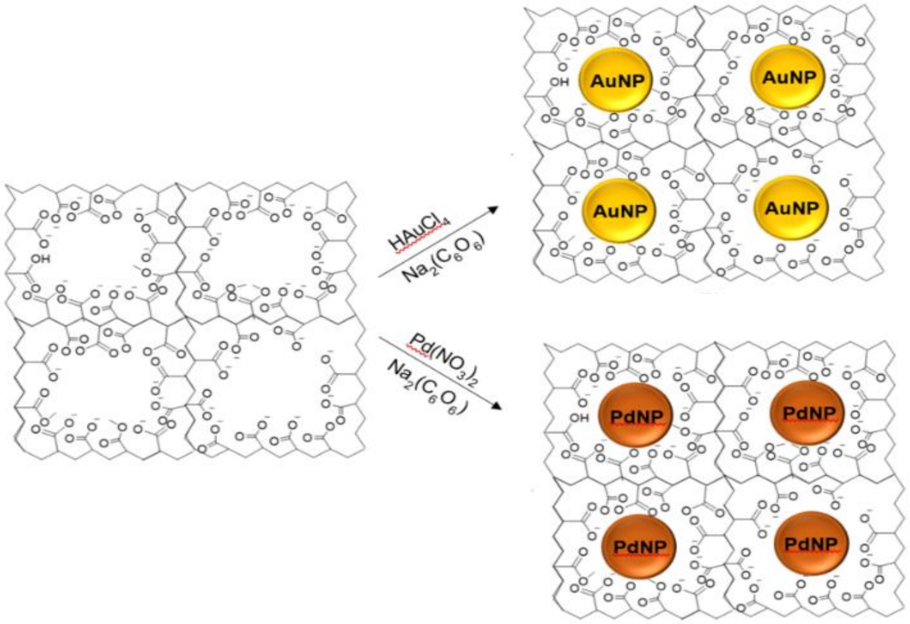

Scheme 6.3: Preparation of Au NPs and PD NPs using PDA polymer as a support.

It's noteworthy that this reduction process was carried out in a manner that led to the creation of AuNPs and PdNPs within the cavities of the COF, and these newly formed nanoparticles exhibited sizes similar to those of the Cu2O NPs that were initially used during the templating process. A crucial aspect of this approach was the utilization of the mild reducing agent sodium rhodizonate instead of strong reducing agents like NaBH4. This choice was deliberate and aimed at preventing the rapid reduction of gold on the polymer surface and ensuring that the reduction primarily occurred within the COF cavities.

6.3.1. Analysis of Crystalline Structure by XRD.

The X-ray diffraction (XRD) analysis of compounds 6 through 9 provides valuable insights into their structural characteristics. PDA-Cu_2O (6) displayed distinct XRD peaks, unequivocally indicating the presence of Cu2O nanoparticles. Importantly, there were no observable XRD peaks associated with Cu or CuO, emphasizing the high purity of the Cu_2O nanoparticles embedded within the polymer matrix. Following the removal of Cu2O, the resulting metal-free COF exhibited an XRD pattern marked by the absence of sharp peaks, signifying its amorphous nature.

This confirmed the successful elimination of Cu_2O nanoparticles from the COF structure. The XRD (X-ray diffraction) spectrum obtained for the PDA-CoO material reveals distinct peaks, each of which corresponds to specific crystallographic planes of cobalt oxide (CoO) within the sample. Notably, there is a prominent peak at approximately 38°, which can be attributed to the (111) plane of CoO. Additionally, a peak is observed at around 42°, corresponding to the (200) plane, and another peak at approximately 75°, signifying the presence of the (311) plane of CoO. These distinct peaks in the XRD pattern provide strong and precise confirmation of the existence of cobalt oxide within the polymeric material, with the peaks' positions indicative of the crystallographic orientation and arrangement of the CoO nanoparticles in the composite.

Upon the regrowth of Au and Pd nanoparticles on this metal-free COF, represented as compounds PDA-Au and PDA-Pd, their XRD diffractograms revealed distinguishable peaks corresponding to AuNPs and PdNPs, respectively. Notably, these peaks appeared less sharply defined, possibly due to the larger quantity of nanoparticles adopting a less crystalline and more amorphous morphology. This amorphous nature can have practical advantages, as amorphous nanoparticles tend to exhibit enhanced reactivity[314], which is a desirable feature for a wide range of catalytic and materials science applications.

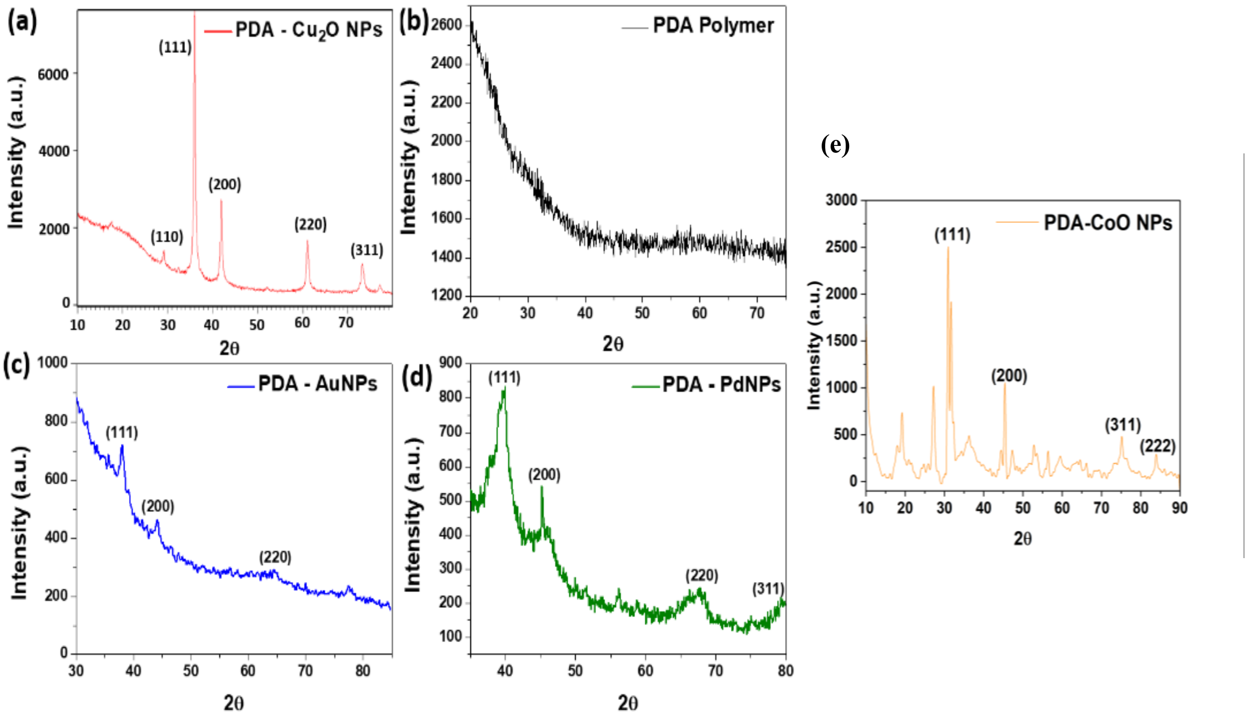

Figure 6.1: XRD diffractograms of (a) PDA-Cu_2O NPs, (b) PDA polymer after NP extraction, (c) PDA-Au NPs, (d) PDA-Pd NPs and (e) PDA-CoO,

6.3.2. Thermogravimetric Analysis (TGA).

Thermogravimetric analysis (TGA) was utilized to explore the thermal decomposition behaviors of compounds PDA-Cu_2O, PDA-Polymer, PDA-AuNPs and PDA-PdNPs as illustrated in Figure 6.2. The results provided valuable insights into the thermal stabilities of these materials.

Following the extraction of Cu2O nanoparticles, PDA polymer exhibited complete decomposition at approximately 200 °C, as evident in Figure 6.2b. In contrast, PDA-Cu2O (Figure 6.2a), PDA-AuNPs (Figure 6.2c), and PDA-PdNPs (Figure 6.2d) displayed distinct decomposition profiles. These profiles were characterized by a relatively linear weight loss trend until reaching stability points, observed at approximately 600 °C for PDA-Cu2O, PDA-AuNPs, and about 400 °C for PDA-PdNPs.

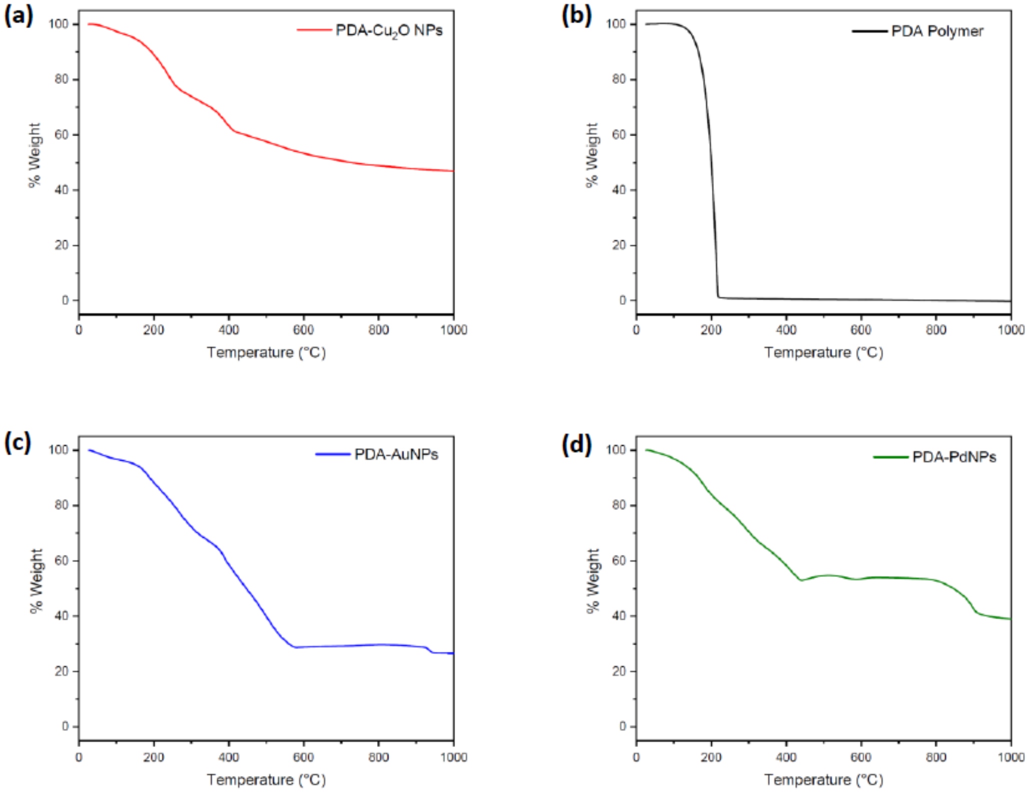

Figure 6.2: TGA analysis of (a) PDA polymer with Cu2O NPs, (b) PDA polymer after NP extraction, (c) PDA polymer with Au NPs and (d) PDA polymer with Pd NPs.

The stability points were reached when the materials retained a specific percentage of their initial weight. For PDA-Cu2O and PDA-PdNPs, this point corresponded to 50% of their original weight, while for PDA-AuNPs, it was observed at 30% compared to the initial 50% weight of PDA-Cu2O. These findings indicate that the reduction of gold and palladium nanoparticles onto the hollow PDA polymer was quantitative for PDA-PdNPs and approximately 60% for PDA-AuNPs. The stability points signify the extent of nanoparticle reduction, offering valuable information about the thermal properties of these materials.

6.3.3. BET Study.

The BET surface analysis of the metal-free PDA polymer yielded intriguing insights into its structural characteristics, with the corresponding data presented in Figure 5.3. Notably, this analysis revealed a specific surface area of approximately 14.32 m^2/g for the metal-free PDA polymer. These findings are especially important as they indicate that, following the removal of Cu_2O nanoparticles, the pores within the COF structure exhibit a tendency to close. Despite this apparent closure, the pores remain functionally active, allowing them to efficiently absorb Au and Pd salts, ultimately facilitating the formation of products PDA-AuNPs and PDA-PdNPs.

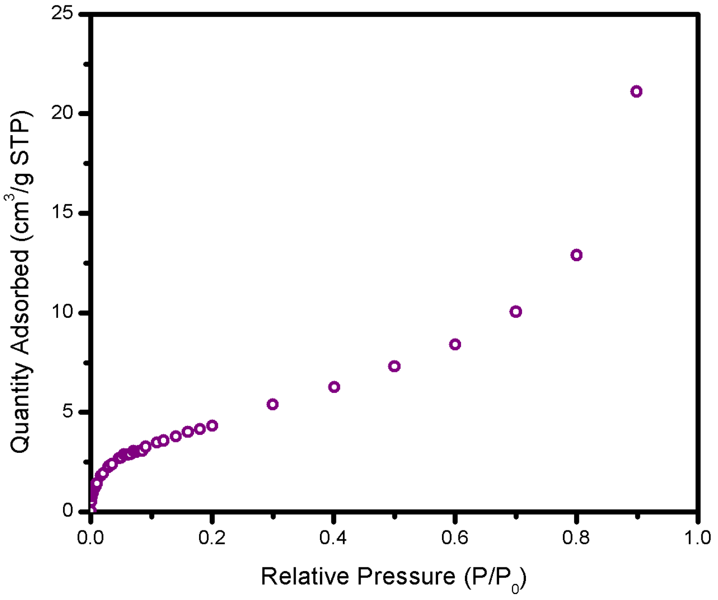

Figure 6.3: BET surface area analysis of PDA polymer after removing Cu2O nanoparticles. Total BET surface area: 14.3206 m2/g.

This observation underscores the remarkable adaptability and structural flexibility of the PDA polymer, enabling it to host metal nanoparticles and interact with various species, even as its porous structure undergoes modifications. The unique surface properties and behavior of the metal-free PDA polymer further emphasizes its potential in accommodating different functional components for diverse applications in materials science and catalysis.

6.3.4. Morphological analysis by TEM.

Transmission electron microscopy (TEM) images provide valuable insights into the structural features of the materials in question. As depicted in Figure 6.4a, TEM images of PDA-Cu_2O illustrate the presence of Cu_2O nanoparticles embedded within the polydiacetylene matrix. In Figure 6.4b, the transmission electron microscopy (TEM) image reveals the presence of CoO nanoparticles embedded within the polymeric material. These nanoparticles exhibit a distinct spherical structure characterized by a high level of monodispersion, signifying that they have a uniform and consistent size and shape distribution. The average size of these CoO nanoparticles falls between 2 to 5 nm. This level of uniformity is essential for precise control and predictable behavior in applications that rely on nanomaterials. Moreover, the absence of agglomeration in both the PDA-Cu2O material and the PDA-CoO nanocomposite is a significant advantage, ensuring that the nanoparticles remain well-dispersed and do not cluster together. This feature is crucial for maintaining the material's structural integrity and optimizing its performance in electrocatalysis. Subsequently, TEM images of the post-assembly casted products, PDA-AuNPs (Figure 6.4c) and PDA-PdNPs (Figure 6.4d), vividly reveal the incorporation of metal nanoparticles within the polydiacetylene structure. Notably, the TEM analysis indicates that PDA-AuNPs exhibit an average particle size of approximately 2.5 nm, while PDA-PdNPs possess an average particle size of around 3.5 nm. These sizes are in close proximity to the average particle size observed in PDA-Cu2O, which measures 3.5 nm.

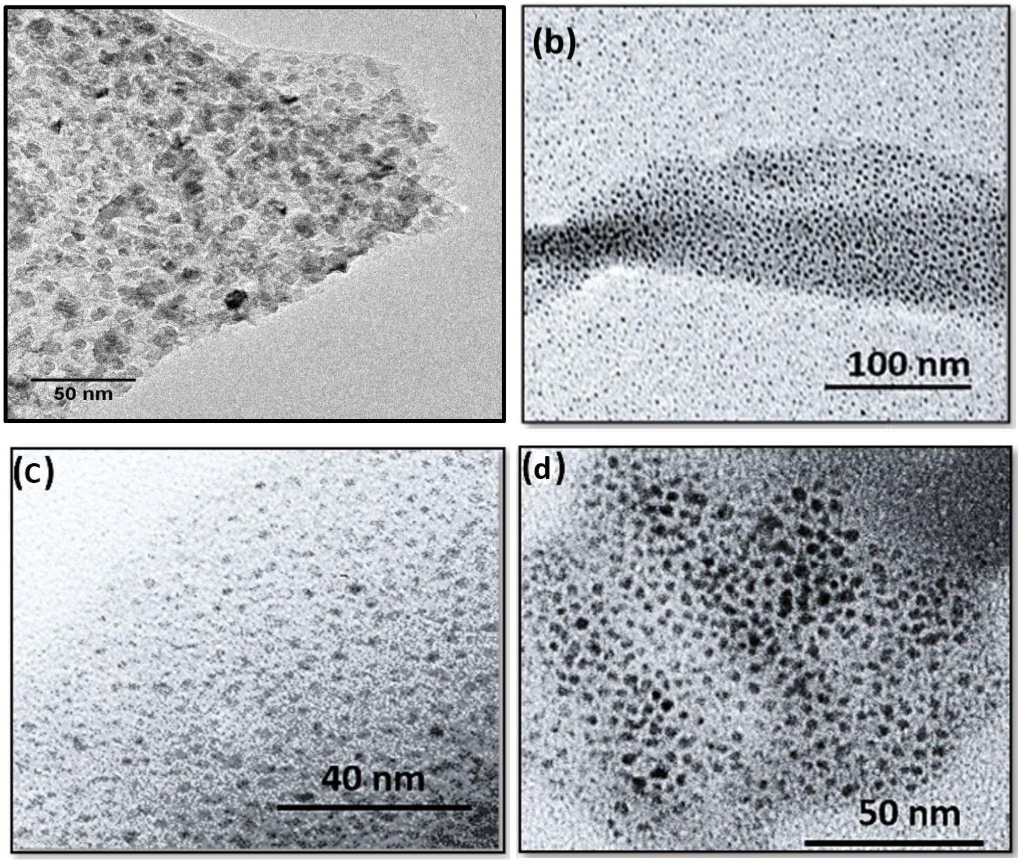

Figure 6.4: TEM images of (a)PDA-CoO NPs, (b) PDA-Cu_2O NPsAuNPs, (c) PDA-AuNPs and PDA-PdNPs nanomaterials.

This uniformity in particle size across the different materials underscores the precision and efficacy of the metal-free COF as a nanocasting mold. It demonstrates the COF's ability to act as a scaffold that accurately dictates the size and shape of the embedded nanoparticles during the casting process. Such control over nanoparticle dimensions is essential for tailoring the properties of these materials for specific applications, including catalysis and sensing.

6.3.5. Morphological SEM and EDX analysis.

The scanning electron microscopy (SEM) image in Figure 6.5 and Figure 6.6 provides insights into the structural characteristics of the PDA-Cu2O and PDA-CoO nanomaterials. It reveals the presence of a crystalline environment within the materials, indicating a well-defined and organized structure. This crystalline structure is crucial for understanding the material's properties and behavior in various applications.

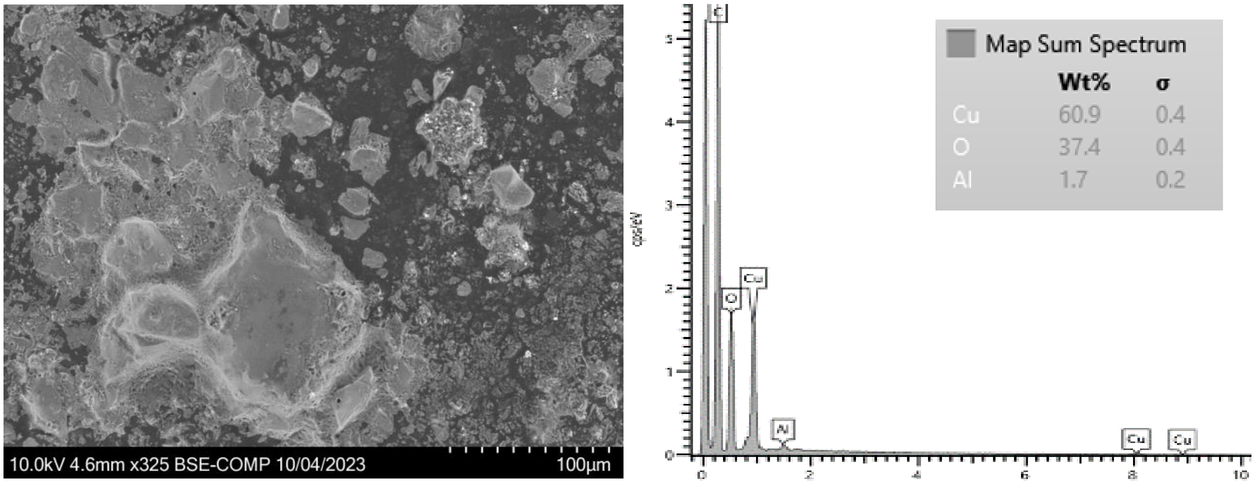

Figure 6.5: (a) Scanning electron microscopy (SEM) and (b) Energy-Dispersive X-Ray Spectroscopy of PDA-Cu_2O.

Additionally, the energy-dispersive X-ray spectroscopy (EDS) elemental analysis offers valuable quantitative information about the material's composition. Specifically, it reveals that the PDA-Cu_2O material contains approximately 60% copper (Cu), while the PDA-CoO shows high values of oxygen and around 10% of cobalt (Co) within its structure. This analysis is essential for assessing the purity and elemental composition of the material, which can have a significant impact on its performance in specific applications.

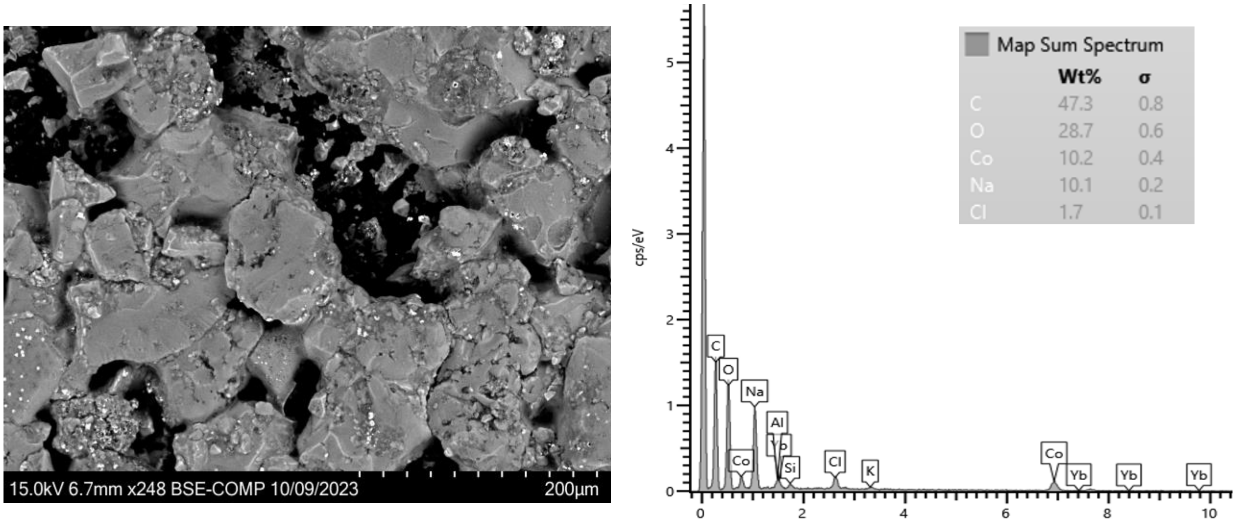

Map Sum Spectrum

	Wt%	σ
C	47.3	0.8
O	28.7	0.6
Co	10.2	0.4
Na	10.1	0.2
Cl	1.7	0.1

Figure 6.6: (a) Scanning electron microscopy (SEM) and (b) Energy-Dispersive X-Ray Spectroscopy of PDA-CoO.

6.3.6. Catalytic activity for Oxygen Evolution Reaction (OER).

In this study, the Oxygen Evolution Reaction (OER) was examined using two distinct nanocatalysts synthesized within the scope of this research: PDA-Co_2O and PDA-CoO. The OER performance of these catalysts was assessed through linear sweep voltammetry, with the results being presented in Figure 6.6. A reference catalyst, RuO_2, was included in these experiments for comparison.

The experimental setup involved subjecting the nanocatalysts to a 10-minute N2-purged 0.1 M KOH solution while rotating at 1600 rpm. During this process, the potential was swept across a range from 200 to 1200 mV vs. 4MKCl/Ag/AgCl/ at a scan rate of 10 mV/s. These voltammetry experiments have provided valuable data, shedding light on the catalytic activity of the various nanocatalysts in the context of OER. By comparing their performance to the benchmark RuO_2 catalyst, this research aims to determine their suitability for a range of applications, particularly within the realms of renewable energy technologies and electrochemical processes. It is essential to note that all potentials are referenced to the Reversible Hydrogen Electrode (RHE) for the materials under investigation.

Figure 6.7 presents a comprehensive analysis of the electrocatalytic performance of two previously synthesized materials, namely PDA-Cu and PDA-Co, within the context of the Oxygen Evolution Reaction (OER). These materials exhibit substantial electrocatalytic activity, as demonstrated by their performance compared to RuO_2, a reference catalyst for this process.

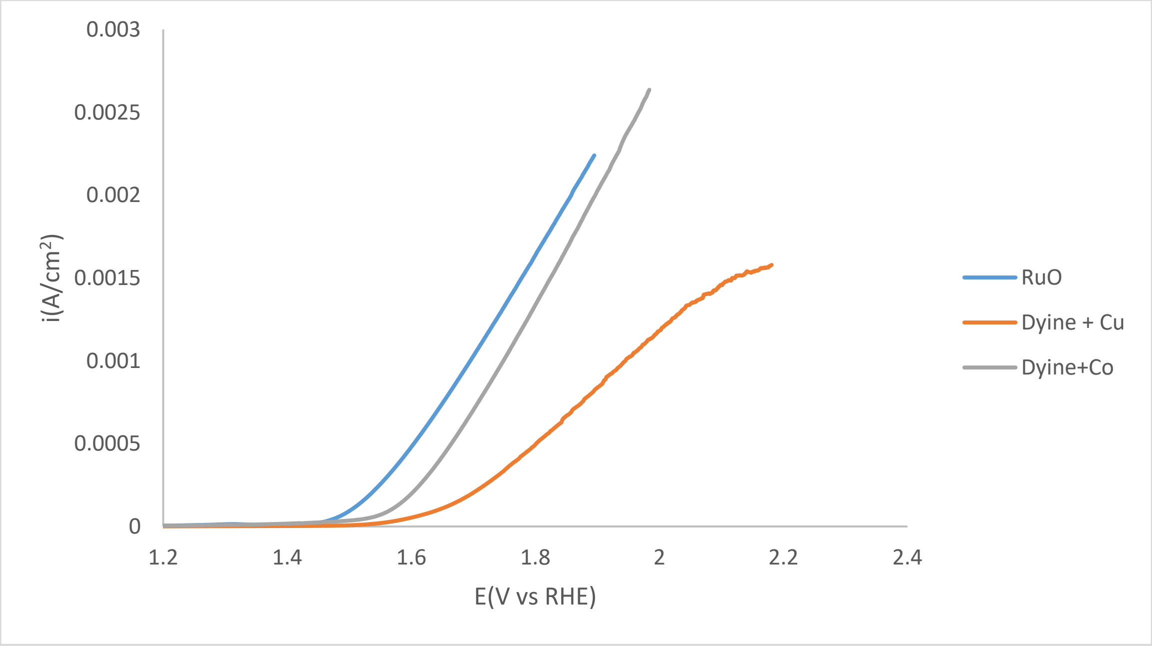

Figure 6.7: Electrocatalytic activity of PDA-Cu2O and PDA-CoO to perform oxygen evolution reactions.

The onset potential for PDA-Cu is measured at 0.65 eV, indicating its ability to initiate the OER process effectively. On the other hand, PDA-Co exhibits a slightly lower onset potential of 0.55 eV, which closely approaches the reference performance of RuO_2. These results are highly promising, particularly for PDA-Co, as they suggest its potential as a catalyst in OER applications.

It's crucial to emphasize that the outstanding performance of these materials is not solely attributed to the choice of the metal component. The polymeric COF material significantly contributes to their performance. This contribution arises from the COF's remarkable electrical conductivity, facilitated by the extensive conjugate system inherent in its structural framework, and its ability to effectively stabilize the metallic nanoparticles within the material. This synergy between the COF and the metal components plays a crucial role in improving the electrocatalytic activity of the materials.

6.4. Conclusions

In summary, our study introduces an innovative approach to synthesize a covalent organic framework (COF) using nanoparticle-templating. This COF is created through the photopolymerization of a binding diyne compound with Cu and Co sources, the final synthesized material is effectively acting as a nanocasting mold for the controlled formation of fresh nanoparticles within its internal structure. The successful generation of AuNPs and PdNPs within the COF, which mirrors the size and shape attributes of the original Cu_2O NPs, demonstrates the effectiveness of this innovative synthesis technique.

This approach not only allows for the incorporation of different metallic nanoparticles into the porous COF material but also imparts unique structural attributes to these newly formed nanoparticles, originating from the initially entrapped nanomaterials.

Furthermore, our study delves into the electrochemical properties of these synthesized nanomaterials, evaluating their catalytic potential for oxygen evolution reactions. The results reveal remarkable catalytic activity for both materials, with particular emphasis on the PDA-CoO nanomaterial, which exhibits potential values closely approaching those of the RuO2 reference catalyst. These findings underscore the promising applications of this material in the fields of electrochemistry and clean energy generation.

References

[1] Hasan, S. (2015). A review on nanoparticles: their synthesis and types. Res. J. Recent Sci, 2277, 2502.

[2] Smita, S., Gupta, S. K., Bartonova, A., Dusinska, M., Gutleb, A. C., & Rahman, Q. (2012). Nanoparticles in the environment: assessment using the causal diagram approach. Environmental Health, 11, 1-11.

[3] Cho, E. J., Holback, H., Liu, K. C., Abouelmagd, S. A., Park, J., & Yeo, Y. (2013). Nanoparticle characterization: state of the art, challenges, and emerging technologies. Molecular pharmaceutics, 10(6), 2093-2110.

[4] Machado, S., Pacheco, J. G., Nouws, H. P. A., Albergaria, J. T., & Delerue-Matos, C. (2015). Characterization of green zero-valent iron nanoparticles produced with tree leaf extracts. Science of the total environment, 533, 76-81.

[5] Masciangioli, T., & Zhang, W. X. (2003). Peer reviewed: environmental technologies at the nanoscale.

[6] Roco, M. C. (2003). Broader societal issues of nanotechnology. *Journal of nanoparticle research*, *5*, 181-189.

[7] Choi, M., Biswas, P., Fissan, H., & Pui, D. Y. H. (2003). Special Issue on Nanoparticles: Technology and Sustainable Development. *J. Nanopart. Res*.

[8] Biswas, P., & Wu, C. Y. (2005). Nanoparticles and the environment. *Journal of the air & waste management association*, *55*(6), 708-746.

[9] Ealia, S. A. M., & Saravanakumar, M. P. (2017, November). A review on the classification, characterisation, synthesis of nanoparticles and their application. In *IOP conference series: materials science and engineering* (Vol. 263, No. 3, p. 032019). IOP Publishing.

[10] Wang, Q., Chen, L., Liu, Z., Tsumori, N., Kitta, M., & Xu, Q. (2019). Phosphate-mediated immobilization of high-performance aupd nanoparticles for dehydrogenation of formic acid at room temperature. Advanced Functional Materials, 29(39), 1903341.

[11] Cao, Y., Geng, W., Shi, R., Shang, L., Waterhouse, G. I., Liu, L., ... & Zhang, T. (2016). Thiolate-Mediated Photoinduced Synthesis of Ultrafine Ag2S Quantum Dots from Silver Nanoparticles. Angewandte Chemie International Edition, 55(48), 14952-14957.

[12] Hui, C. Y., Liu, M., Li, Y., & Brennan, J. D. (2018). A paper sensor printed with multifunctional bio/nano materials. Angewandte Chemie, 130(17), 4639-4643.

[13] Gao, L., Cao, K., Hu, X., Xiao, R., Gan, B., Wang, W., & Lu, Y. (2020). Nano electromechanical approach for flexible piezoresistive sensor. Applied Materials Today, 18, 100475.

[14] Liu, P., Zhu, K., Gao, Y., Luo, H., & Lu, L. (2017). Recent progress in the applications of vanadium-based oxides on energy storage: from low-dimensional nanomaterials synthesis to 3D micro/nano-structures and free-standing electrodes fabrication. Advanced Energy Materials, 7(23), 1700547.

[15] Wu, J., Mahajan, A., Riekehr, L., Zhang, H., Yang, B., Meng, N., ... & Yan, H. (2018). Perovskite Srx (Bi1− xNa0. 97− xLi0. 03) 0.5 TiO3 ceramics with polar nano regions for high power energy storage. Nano Energy, 50, 723-732.

[16] Bjornmalm, M., Thurecht, K. J., Michael, M., Scott, A. M., & Caruso, F. (2017). Bridging bio–nano science and cancer nanomedicine. ACS nano, 11(10), 9594-9613.

[17] Zhang, S., Zhou, S., Liu, H., Xing, M., Ding, B., & Li, B. (2020). Pinecone-inspired nanoarchitectured smart microcages enable nano/microparticle drug delivery. Advanced Functional Materials, 30(28), 2002434.

[18] Tao, R., Ma, X., Wei, X., Jin, Y., Qiu, L., & Zhang, W. (2020). Porous organic polymer material supported palladium nanoparticles. Journal of Materials Chemistry A, 8(34), 17360-17391.

[19] Zhu, Q. L., & Xu, Q. (2016). Immobilization of ultrafine metal nanoparticles to high-surface-area materials and their catalytic applications. Chem, 1(2), 220-245.

[20] Yang, J., Zhu, Y., Fan, M., Sun, X., Wang, W. D., & Dong, Z. (2019). Ultrafine palladium nanoparticles confined in core–shell magnetic porous organic polymer nanospheres as highly efficient hydrogenation catalyst. Journal of colloid and interface science, 554, 157-165.

[21] Zhang, R., Huang, K., Wang, D., Hussain, N., Zhang, A., Wei, H., ... & Wu, H. (2019). Ultrafine Fe/Fe3C nanoparticles on nitrogen-doped mesoporous carbon by low-temperature synthesis for highly efficient oxygen reduction. Electrochimica Acta, 313, 255-260.

[22] Zhao, Z. W., Zhou, X., Liu, Y. N., Shen, C. C., Yuan, C. Z., Jiang, Y. F., ... & Xu, A. W. (2018). Ultrasmall Ni nanoparticles embedded in Zr-based MOFs provide high selectivity for CO 2 hydrogenation to methane at low temperatures. Catalysis Science & Technology, 8(12), 3160-3165.

[23] Voorhees, P. W. (1985). The theory of Ostwald ripening. Journal of Statistical Physics, 38, 231-252.

[24] Zhang, Y., Hu, Y., Zhao, J., Park, E., Jin, Y., Liu, Q., & Zhang, W. (2019). Covalent organic framework-supported Fe–TiO 2 nanoparticles as ambient-light-active photocatalysts. Journal of Materials Chemistry A, 7(27), 16364-16371.

[25] Cui, X., Xu, Y., Chen, L., Zhao, M., Yang, S., & Wang, Y. (2019). Ultrafine Pd nanoparticles supported on zeolite-templated mesocellular graphene network via framework aluminum

mediation: An advanced oxygen reduction electrocatalyst. Applied Catalysis B: Environmental, 244, 957-964.

[26] Li, H., Zhang, M., Yi, L., Liu, Y., Chen, K., Shao, P., & Wen, Z. (2021). Ultrafine Ru nanoparticles confined in 3D nitrogen-doped porous carbon nanosheet networks for alkali-acid Zn-H2 hybrid battery. Applied Catalysis B: Environmental, 280, 119412.

[27] Chen, F., Shen, K., Chen, J., Yang, X., Cui, J., & Li, Y. (2019). General immobilization of ultrafine alloyed nanoparticles within metal–organic frameworks with high loadings for advanced synergetic catalysis. ACS Central Science, 5(1), 176-185.

[28] Lu, S., Hu, Y., Wan, S., McCaffrey, R., Jin, Y., Gu, H., & Zhang, W. (2017). Synthesis of ultrafine and highly dispersed metal nanoparticles confined in a thioether-containing covalent organic framework and their catalytic applications. Journal of the American Chemical Society, 139(47), 17082-17088.

[29] Cao, H. L., Huang, H. B., Chen, Z., Karadeniz, B., Lü, J., & Cao, R. (2017). Ultrafine silver nanoparticles supported on a conjugated microporous polymer as high-performance nanocatalysts for nitrophenol reduction. ACS applied materials & interfaces, 9(6), 5231-5236.

[30] Lapworth, D. J., Baran, N., Stuart, M. E., & Ward, R. S. (2012). Emerging organic contaminants in groundwater: a review of sources, fate and occurrence. *Environmental pollution*, *163*, 287-303.

[31] Verstraeten, I. M., Fetterman, G. S., Meyer, M. T., Bullen, T., & Sebree, S. K. (2005). Use of tracers and isotopes to evaluate vulnerability of water in domestic wells to septic waste. *Groundwater Monitoring & Remediation*, *25*(2), 107-117.

[32] Heberer, T., Mechlinski, A., Fanck, B., Knappe, A., Massmann, G., Pekdeger, A., & Fritz, B. (2004). Field studies on the fate and transport of pharmaceutical residues in bank filtration. *Groundwater Monitoring & Remediation*, *24*(2), 70-77.

[33] Kümmerer, K. (2001). Drugs in the environment: emission of drugs, diagnostic aids and disinfectants into wastewater by hospitals in relation to other sources–a review. *Chemosphere*, *45*(6-7), 957-969.

[34] Eckel, W. P., Ross, B., & Isensee, R. K. (1993). Pentobarbital found in ground water. *Groundwater*, *31*(5), 801-804.

[35] Buerge, I. J., Buser, H. R., Kahle, M., Muller, M. D., & Poiger, T. (2009). Ubiquitous occurrence of the artificial sweetener acesulfame in the aquatic environment: an ideal chemical marker of domestic wastewater in groundwater. *Environmental science & technology*, *43*(12), 4381-4385.

[36] Heathwaite, A. L., Quinn, P. F., & Hewett, C. J. M. (2005). Modelling and managing critical source areas of diffuse pollution from agricultural land using flow connectivity simulation. *Journal of Hydrology*, *304*(1-4), 446-461.

[37] Kim, G., Yur, J., & Kim, J. (2007). Diffuse pollution loading from urban stormwater runoff in Daejeon city, Korea. *Journal of environmental management*, *85*(1), 9-16.

[38] Mohan, D., Sarswat, A., Ok, Y. S., & Pittman Jr, C. U. (2014). Organic and inorganic contaminants removal from water with biochar, a renewable, low cost and sustainable adsorbent–a critical review. *Bioresource technology*, *160*, 191-202.

[39] Devi, P., Singh, P., & Kansal, S. K. (Eds.). (2020). *Inorganic Pollutants in Water*. Elsevier.

[40] Reneau Jr, R. B., Hagedorn, C., & Degen, M. J. (1989). Fate and transport of biological and inorganic contaminants from on-site disposal of domestic wastewater. *Journal of Environmental Quality*, *18*(2), 135-144.

[41] World Health Organization. (2004). *Guidelines for drinking-water quality* (Vol. 1). World Health Organization.

[42] Ahluwalia, S. S., & Goyal, D. (2007). Microbial and plant derived biomass for removal of heavy metals from wastewater. *Bioresource technology*, *98*(12), 2243-2257.

[43] Fu, F., & Wang, Q. (2011). Removal of heavy metal ions from wastewaters: a review. *Journal of environmental management*, *92*(3), 407-418.

[44] Ali, I., Mbianda, X. Y., Burakov, A., Galunin, E., Burakova, I., Mkrtchyan, E., ... & Grachev, V. (2019). Graphene based adsorbents for remediation of noxious pollutants from wastewater. *Environment international*, *127*, 160-180.

[45] Shan, G., Surampalli, R. Y., Tyagi, R. D., & Zhang, T. C. (2009). Nanomaterials for environmental burden reduction, waste treatment, and nonpoint source pollution control: a review. *Frontiers of Environmental Science & Engineering in China*, *3*, 249-264.

[46] Ghasemzadeh, G., Momenpour, M., Omidi, F., Hosseini, M. R., Ahani, M., & Barzegari, A. (2014). Applications of nanomaterials in water treatment and environmental remediation. *Frontiers of environmental science & engineering*, *8*, 471-482.

[47] Medina, S. H., & El-Sayed, M. E. (2009). Dendrimers as carriers for delivery of chemotherapeutic agents. *Chemical reviews*, *109*(7), 3141-3157.

[48] Tomalia, D. A., Naylor, A. M., & Goddard III, W. A. (1990). Starburst dendrimers: molecular-level control of size, shape, surface chemistry, topology, and flexibility from atoms to macroscopic matter. *Angewandte Chemie International Edition in English*, *29*(2), 138-175.

[49] Diallo, M. S., Christie, S., Swaminathan, P., Balogh, L., Shi, X., Um, W., ... & Johnson, J. H. (2004). Dendritic chelating agents. 1. Cu (II) binding to ethylene diamine core poly (amidoamine) dendrimers in aqueous solutions. *Langmuir, 20*(7), 2640-2651.

[50] Mangun, C. L., Yue, Z., Economy, J., Maloney, S., Kemme, P., & Cropek, D. (2001). Adsorption of organic contaminants from water using tailored ACFs. *Chemistry of materials*, *13*(7), 2356-2360.

[51] Rai, M., Yadav, A., & Gade, A. (2009). Silver nanoparticles as a new generation of antimicrobials. *Biotechnology advances*, *27*(1), 76-83.

[52] Lowry, G. V., & Johnson, K. M. (2004). Congener-specific dechlorination of dissolved PCBs by microscale and nanoscale zerovalent iron in a water/methanol solution. *Environmental Science & Technology*, *38*(19), 5208-5216.

[53] Stone, V., Nowack, B., Baun, A., van den Brink, N., von der Kammer, F., Dusinska, M., ... & Fernandes, T. F. (2010). Nanomaterials for environmental studies: classification, reference material issues, and strategies for physico-chemical characterisation. *Science of the total environment*, *408*(7), 1745-1754.

[54] Hu, J. S., Zhong, L. S., Song, W. G., & Wan, L. J. (2008). Synthesis of hierarchically structured metal oxides and their application in heavy metal ion removal. *Advanced Materials*, *20*(15), 2977-2982.

[55] Chu, S., & Majumdar, A. (2012). Opportunities and challenges for a sustainable energy future. *nature*, *488*(7411), 294-303.

[56] Cook, T. R., Dogutan, D. K., Reece, S. Y., Surendranath, Y., Teets, T. S., & Nocera, D. G. (2010). Solar energy supply and storage for the legacy and nonlegacy worlds. *Chemical reviews*, *110*(11), 6474-6502.

[57] Benson, E. E., Kubiak, C. P., Sathrum, A. J., & Smieja, J. M. (2009). Electrocatalytic and homogeneous approaches to conversion of CO 2 to liquid fuels. *Chemical Society Reviews*, *38*(1), 89-99.

[58] Turner, J. A. (2004). Sustainable hydrogen production. *Science*, *305*(5686), 972-974.

[59] Zeng, K., & Zhang, D. (2010). Recent progress in alkaline water electrolysis for hydrogen production and applications. *Progress in energy and combustion science*, *36*(3), 307-326.

[60] Marini, S., Salvi, P., Nelli, P., Pesenti, R., Villa, M., Berrettoni, M., ... & Kiros, Y. (2012). Advanced alkaline water electrolysis. *Electrochimica Acta*, *82*, 384-391.

[61] Carrette, L., Friedrich, K. A., & Stimming, U. (2001). Fuel cells-fundamentals and applications. *Fuel cells*, *1*.

[62] Arico, A. S., Srinivasan, S., & Antonucci, V. (2001). DMFCs: from fundamental aspects to technology development. *Fuel cells*, *1*(2), 133-161.

[63] Palacin, M. R. (2009). Recent advances in rechargeable battery materials: a chemist's perspective. *Chemical Society Reviews*, *38*(9), 2565-2575.

[64] Suntivich, J., Gasteiger, H. A., Yabuuchi, N., Nakanishi, H., Goodenough, J. B., & Shao-Horn, Y. (2011). Design principles for oxygen-reduction activity on perovskite oxide catalysts for fuel cells and metal–air batteries. *Nature chemistry*, *3*(7), 546-550.

[65] Cheng, F., & Chen, J. (2012). Metal–air batteries: from oxygen reduction electrochemistry to cathode catalysts. *Chemical Society Reviews*, *41*(6), 2172-2192.

[66] Suen, N. T., Hung, S. F., Quan, Q., Zhang, N., Xu, Y. J., & Chen, H. M. (2017). Electrocatalysis for the oxygen evolution reaction: recent development and future perspectives. *Chemical Society Reviews*, *46*(2), 337-365.

[67] Roger, I., Shipman, M. A., & Symes, M. D. (2017). Earth-abundant catalysts for electrochemical and photoelectrochemical water splitting. *Nature Reviews Chemistry*, *1*(1), 0003.

[68] You, B., & Sun, Y. (2018). Innovative strategies for electrocatalytic water splitting. *Accounts of chemical research*, *51*(7), 1571-1580.

[69] Sultan, S., Tiwari, J. N., Singh, A. N., Zhumagali, S., Ha, M., Myung, C. W., ... & Kim, K. S. (2019). Single atoms and clusters based nanomaterials for hydrogen evolution, oxygen evolution reactions, and full water splitting. *Advanced Energy Materials*, *9*(22), 1900624.

[70] Jin, H., Wang, J., Su, D., Wei, Z., Pang, Z., & Wang, Y. (2015). In situ cobalt–cobalt oxide/N-doped carbon hybrids as superior bifunctional electrocatalysts for hydrogen and oxygen evolution. *Journal of the American Chemical Society*, *137*(7), 2688-2694.

[71] Chen, X., Li, C., Grätzel, M., Kostecki, R., & Mao, S. S. (2012). Nanomaterials for renewable energy production and storage. *Chemical Society Reviews*, *41*(23), 7909-7937.

[72] Mao, S. S., Shen, S., & Guo, L. (2012). Nanomaterials for renewable hydrogen production, storage and utilization. *Progress in Natural Science: Materials International*, *22*(6), 522-534.

[73] Wang, X., & Chen, X. (Eds.). (2018). *Novel nanomaterials for biomedical, environmental and energy applications*. Elsevier.

[74] Niemann, M. U., Srinivasan, S. S., Phani, A. R., Kumar, A., Goswami, D. Y., & Stefanakos, E. K. (2008). Nanomaterials for hydrogen storage applications: a review. *Journal of Nanomaterials, 2008*.

[75] Ojha, K., Saha, S., Dagar, P., & Ganguli, A. K. (2018). Nanocatalysts for hydrogen evolution reactions. *Physical Chemistry Chemical Physics*, *20*(10), 6777-6799.

[76] Cherevko, S., Reier, T., Zeradjanin, A. R., Pawolek, Z., Strasser, P., & Mayrhofer, K. J. (2014). Stability of nanostructured iridium oxide electrocatalysts during oxygen evolution reaction in acidic environment. *Electrochemistry Communications*, *48*, 81-85.

[77] Kong, F. D., Zhang, S., Yin, G. P., Wang, Z. B., Du, C. Y., Chen, G. Y., & Zhang, N. (2012). Electrochemical studies of Pt/Ir–IrO2 electrocatalyst as a bifunctional oxygen electrode. *International journal of hydrogen energy*, *37*(1), 59-67.

[78] Zheng, Y., Jiao, Y., Zhu, Y., Li, L. H., Han, Y., Chen, Y., ... & Qiao, S. Z. (2016). High electrocatalytic hydrogen evolution activity of an anomalous ruthenium catalyst. *Journal of the American Chemical Society*, *138*(49), 16174-16181.

[79] Anantharaj, S., Ede, S. R., Sakthikumar, K., Karthick, K., Mishra, S., & Kundu, S. (2016). Recent trends and perspectives in electrochemical water splitting with an emphasis on sulfide, selenide, and phosphide catalysts of Fe, Co, and Ni: a review. *Acs Catalysis*, *6*(12), 8069-8097.

[80] Hu, Q., Li, G., Han, Z., Wang, Z., Huang, X., Yang, H., ... & He, C. (2019). Recent progress in the hybrids of transition metals/carbon for electrochemical water splitting. *Journal of Materials Chemistry A*, *7*(24), 14380-14390.

[81] Jamesh, M. I. (2016). Recent progress on earth abundant hydrogen evolution reaction and oxygen evolution reaction bifunctional electrocatalyst for overall water splitting in alkaline media. *Journal of Power Sources*, *333*, 213-236.

[82] Song, F., Bai, L., Moysiadou, A., Lee, S., Hu, C., Liardet, L., & Hu, X. (2018). Transition metal oxides as electrocatalysts for the oxygen evolution reaction in alkaline solutions: an application-inspired renaissance. *Journal of the American Chemical Society*, *140*(25), 7748-7759.

[83] Osmieri, L., Monteverde Videla, A. H., Ocón, P., & Specchia, S. (2017). Kinetics of oxygen electroreduction on Me–N–C (Me= Fe, Co, Cu) catalysts in acidic medium: insights on the effect of the transition metal. *The Journal of Physical Chemistry C*, *121*(33), 17796-17817.

[84] Yuan, N., Jiang, Q., Li, J., & Tang, J. (2020). A review on non-noble metal based electrocatalysis for the oxygen evolution reaction. *Arabian Journal of Chemistry*, *13*(2), 4294-4309.

[85] Li, Q., Li, J., Xu, J., Zhang, N., Li, Y., Liu, L., ... & Deepak, F. L. (2020). Ultrafine-grained porous Ir-based catalysts for high-performance overall water splitting in acidic media. *ACS Applied Energy Materials*, *3*(4), 3736-3744.

[86] Paul, S. C., Dey, S. C., Molla, M. A. I., Islam, M. S., Debnath, S., Miah, M. Y., ... & Sarker, M. (2021). Nanomaterials as electrocatalyst for hydrogen and oxygen evolution reaction: Exploitation of challenges and current progressions. *Polyhedron*, *193*, 114871.

[87] Aubert, A. H., Bauer, R., & Lienert, J. (2018). A review of water-related serious games to specify use in environmental Multi-Criteria Decision Analysis. *Environmental modelling & software*, *105*, 64-78.

[88] Rijsberman, F. R. (2006). Water scarcity: fact or fiction?. *Agricultural water management*, *80*(1-3), 5-22.

[89] Saha, N., Rahman, M. S., Ahmed, M. B., Zhou, J. L., Ngo, H. H., & Guo, W. (2017). Industrial metal pollution in water and probabilistic assessment of human health risk. *Journal of environmental management*, *185*, 70-78.

[90] Bhat, S. A., Singh, S., Singh, J., Kumar, S., & Vig, A. P. (2018). Bioremediation and detoxification of industrial wastes by earthworms: vermicompost as powerful crop nutrient in sustainable agriculture. *Bioresource technology*, *252*, 172-179.

[91] Wang, N., Du, Y., Ma, W., Xu, P., & Han, X. (2017). Rational design and synthesis of SnO2-encapsulated α-Fe2O3 nanocubes as a robust and stable photo-Fenton catalyst. *Applied Catalysis B: Environmental*, *210*, 23-33.

[92] Huang, Y. F., Sun, X. Y., Huo, S. H., Li, Y., & Zhong, C. (2019). Core-shell dual-MOF heterostructures derived magnetic CoFe2O4/CuO (sub) microcages with superior catalytic performance. *Applied Surface Science*, *466*, 637-646.

[93] Rego, R. M., Kuriya, G., Kurkuri, M. D., & Kigga, M. (2021). MOF based engineered materials in water remediation: Recent trends. *Journal of hazardous materials*, *403*, 123605.

[94] Kummu, M., Guillaume, J. H., de Moel, H., Eisner, S., Flörke, M., Porkka, M., ... & Ward, P. J. (2016). The world's road to water scarcity: shortage and stress in the 20th century and pathways towards sustainability. *Scientific reports*, *6*(1), 38495.

[95] Tong, T., & Elimelech, M. (2016). The global rise of zero liquid discharge for wastewater management: drivers, technologies, and future directions. *Environmental science & technology*, *50*(13), 6846-6855.

[96] Alrumman, S. A., El-kott, A. F., & Keshk, S. M. A. S. (2016). Water pollution: Source and treatment. *American Journal of Environmental Engineering*, *6*(3), 88-98.

[97] Mon, M., Bruno, R., Ferrando-Soria, J., Armentano, D., & Pardo, E. (2018). Metal–organic framework technologies for water remediation: towards a sustainable ecosystem. *Journal of materials chemistry A*, *6*(12), 4912-4947.

[98] Wang, C. C., Li, J. R., Lv, X. L., Zhang, Y. Q., & Guo, G. (2014). Photocatalytic organic pollutants degradation in metal–organic frameworks. *Energy & Environmental Science*, *7*(9), 2831-2867.

[99] Nasrollahzadeh, M., Shafiei, N., Nezafat, Z., & Bidgoli, N. S. S. (2020). Recent progresses in the application of lignin derived (nano) catalysts in oxidation reactions. *Molecular Catalysis*, *489*, 110942.

[100] Ma, M., Yang, Y., Feng, R., Jia, L., Chen, G., Li, W., & Lyu, P. (2018). Preparation and characterization of magnetic hollow Fe3O4/P (GMA-EGDMA)-SO3H/Au-PPy recyclable catalyst for catalytic reduction of 4-nitrophenol. *Applied Organometallic Chemistry*, *32*(12), e4534.

[101] Duan, C., Liu, C., Meng, X., Lu, W., & Ni, Y. (2019). Fabrication of carboxymethylated cellulose fibers supporting Ag NPs@ MOF-199s nanocatalysts for catalytic reduction of 4-nitrophenol. *Applied Organometallic Chemistry*, *33*(5), e4865.

[102] Nemanashi, M., & Meijboom, R. (2016). “Cat in a bag” recycling of dendrimer encapsulated Au nanoparticles by use of dialysis membrane bag in the reduction of 4-nitrophenol: proof of heterogeneous catalysis. *Catalysis Communications*, *83*, 53-57.

[103] Jiang, Z., Xie, J., Jiang, D., Jing, J., & Qin, H. (2012). Facile route fabrication of nano-Ni core mesoporous-silica shell particles with high catalytic activity towards 4-nitrophenol reduction. *CrystEngComm*, *14*(14), 4601-4611.

[104] Zhang, Y., Zhang, N., Tang, Z. R., & Xu, Y. J. (2014). Graphene oxide as a surfactant and support for in-situ synthesis of Au–Pd nanoalloys with improved visible light photocatalytic activity. *The Journal of Physical Chemistry C*, *118*(10), 5299-5308.

[105] Herrmann, W. A., & Cornils, B. (Eds.). (2002). *Applied Homogeneous Catalysis with Organometallic Compounds: A Comprehensive Handbook in Three Volumes*. Wiley-VCH.

[106] Burda, C., Chen, X., Narayanan, R., & El-Sayed, M. A. (2005). Chemistry and properties of nanocrystals of different shapes. *Chemical reviews*, *105*(4), 1025-1102.

[107] Chinnappan, A., Eshkalak, S. K., Baskar, C., Khatibzadeh, M., Kowsari, E., & Ramakrishna, S. (2019). Flower-like 3-dimensional hierarchical Co 3 O 4/NiO microspheres for 4-nitrophenol reduction reaction. *Nanoscale Advances*, *1*(1), 305-313.

[108] Ploychompoo, S., Liang, Q., Zhou, X., Wei, C., & Luo, H. (2021). Fabrication of Zn-MOF-74/polyacrylamide coated with reduced graphene oxide (Zn-MOF-74/rGO/PAM) for As (III) removal. *Physica E: Low-dimensional Systems and Nanostructures*, *125*, 114377.

[109] Langseth, E., Swang, O., Arstad, B., Lind, A., Cavka, J. H., Jensen, T. L., ... & Heyn, R. H. (2019). Synthesis and characterization of Al@ MOF materials. *Materials Chemistry and Physics*, *226*, 220-225.

[110] Cheng, G., Zhang, A., Zhao, Z., Chai, Z., Hu, B., Han, B., ... & Wang, X. (2021). Extremely stable amidoxime functionalized covalent organic frameworks for uranium extraction from seawater with high efficiency and selectivity. *Science Bulletin*, *66*(19), 1994-2001.

[111] Li, J., Wang, X., Zhao, G., Chen, C., Chai, Z., Alsaedi, A., ... & Wang, X. (2018). Metal–organic framework-based materials: superior adsorbents for the capture of toxic and radioactive metal ions. *Chemical Society Reviews*, *47*(7), 2322-2356.

[112] Liu, J., Wöll, C. Surface-supported metal–organic framework thin films: fabrication methods, applications, and challenges. Chem. Soc. Rev. 2017. 46, 5730–5770.

[113] Liu, Y., Huo, Y., Wang, X., Yu, S., Ai, Y., Chen, Z., ... & Wang, X. (2021). Impact of metal ions and organic ligands on uranium removal properties by zeolitic imidazolate framework materials. *Journal of Cleaner Production*, *278*, 123216.

[114] Liu, X., Pang, H., Liu, X., Li, Q., Zhang, N., Mao, L., ... & Wang, X. (2021). Orderly porous covalent organic frameworks-based materials: superior adsorbents for pollutants removal from aqueous solutions. *The innovation, 2*(1).

[115] Wang, C., Luan, J., & Wu, C. (2019). Metal-organic frameworks for aquatic arsenic removal. *Water research*, *158*, 370-382.

[116] Li, B., Wen, H. M., Cui, Y., Zhou, W., Qian, G., & Chen, B. (2016). Emerging multifunctional metal–organic framework materials. *Advanced Materials*, *28*(40), 8819-8860.

[117] Silva, P., Vilela, S. M., Tome, J. P., & Paz, F. A. A. (2015). Multifunctional metal–organic frameworks: from academia to industrial applications. *Chemical Society Reviews*, *44*(19), 6774-6803.

[118] Bétard, A., & Fischer, R. A. (2012). Metal–organic framework thin films: from fundamentals to applications. *Chemical reviews*, *112*(2), 1055-1083.

[119] Kadhom, M., & Deng, B. (2018). Metal-organic frameworks (MOFs) in water filtration membranes for desalination and other applications. *Applied Materials Today*, *11*, 219-230.

[120] Li, J., Wang, H., Yuan, X., Zhang, J., & Chew, J. W. (2020). Metal-organic framework membranes for wastewater treatment and water regeneration. *Coordination Chemistry Reviews*, *404*, 213116.

[121] Li, X., Liu, Y., Wang, J., Gascon, J., Li, J., & Van der Bruggen, B. (2017). Metal–organic frameworks based membranes for liquid separation. *Chemical Society Reviews*, *46*(23), 7124-7144.

[122] Hermes, S., Schröder, F., Chelmowski, R., Wöll, C., & Fischer, R. A. (2005). Selective nucleation and growth of metal− organic open framework thin films on patterned COOH/CF3-terminated self-assembled monolayers on Au (111). *Journal of the American Chemical Society*, *127*(40), 13744-13745.

[123] Furukawa, H., Cordova, K. E., O’Keeffe, M., & Yaghi, O. M. (2013). The chemistry and applications of metal-organic frameworks. *Science*, *341*(6149), 1230444.

[124] Dhaka, S., Kumar, R., Deep, A., Kurade, M. B., Ji, S. W., & Jeon, B. H. (2019). Metal–organic frameworks (MOFs) for the removal of emerging contaminants from aquatic environments. *Coordination Chemistry Reviews*, *380*, 330-352.

[125] Yaghi, O. M., O'Keeffe, M., Ockwig, N. W., Chae, H. K., Eddaoudi, M., & Kim, J. (2003). Reticular synthesis and the design of new materials. *Nature*, *423*(6941), 705-714.

[126] Lu, W., Wei, Z., Gu, Z. Y., Liu, T. F., Park, J., Park, J., ... & Zhang, Q. (2014). Gentle Iii, T.; Bosch, M.; Zhou, H.-C. *Chem. Soc. Rev*, *43*(16), 5561-5593.

[127] Rego, R. M., Kuriya, G., Kurkuri, M. D., & Kigga, M. (2021). MOF based engineered materials in water remediation: Recent trends. *Journal of hazardous materials*, *403*, 123605.

[128] Sabo, M., Henschel, A., Fröde, H., Klemm, E., & Kaskel, S. (2007). Solution infiltration of palladium into MOF-5: synthesis, physisorption and catalytic properties. *Journal of Materials Chemistry*, *17*(36), 3827-3832.

[129] Huang, Y., Liu, S., Lin, Z., Li, W., Li, X., & Cao, R. (2012). Facile synthesis of palladium nanoparticles encapsulated in amine-functionalized mesoporous metal–organic frameworks and catalytic for dehalogenation of aryl chlorides. *Journal of catalysis*, *292*, 111-117.

[130] Wang, L., Meng, T., Fan, Y., Chen, C., Guo, Z., Wang, H., & Zhang, Y. (2018). Electrochemical study of acetaminophen oxidation by gold nanoparticles supported on a leaf-like zeolitic imidazolate framework. *Journal of colloid and interface science*, *524*, 1-7.

[131] Wang, L., Meng, T., Liang, L., Sun, J., Wu, S., Wang, H., ... & Zhang, Y. (2019). Fabrication of amine-functionalized metal-organic frameworks with embedded palladium nanoparticles for highly sensitive electrochemical detection of telomerase activity. *Sensors and Actuators B: Chemical*, *278*, 133-139.

[132] Nabi, S., Sofi, F. A., Rashid, N., Ingole, P. P., & Bhat, M. A. (2020). Au-nanoparticle loaded nickel-copper bimetallic MOF: An excellent catalyst for chemical degradation of Rhodamine B. *Inorganic Chemistry Communications*, *117*, 107949.

[133] Huang, G., Yang, Q., Xu, Q., Yu, S. H., & Jiang, H. L. (2016). Polydimethylsiloxane coating for a palladium/MOF composite: highly improved catalytic performance by surface hydrophobization. *Angewandte Chemie*, *128*(26), 7505-7509.

[134] Koo, W. T., Choi, S. J., Kim, S. J., Jang, J. S., Tuller, H. L., & Kim, I. D. (2016). Heterogeneous sensitization of metal–organic framework driven metal@ metal oxide complex catalysts on an oxide nanofiber scaffold toward superior gas sensors. *Journal of the American Chemical Society*, *138*(40), 13431-13437.

[135] Zhao, Y., Zhang, J., Song, J., Li, J., Liu, J., Wu, T., ... & Han, B. (2011). Ru nanoparticles immobilized on metal–organic framework nanorods by supercritical CO 2-methanol solution: highly efficient catalyst. *Green Chemistry*, *13*(8), 2078-2082.

[136] Zlotea, C., Campesi, R., Cuevas, F., Leroy, E., Dibandjo, P., Volkringer, C., ... & Latroche, M. (2010). Pd nanoparticles embedded into a metal-organic framework: synthesis, structural characteristics, and hydrogen sorption properties. *Journal of the American Chemical Society*, *132*(9), 2991-2997.

[137] Li, F., Li, R., Feng, Y., Gong, T., Zhang, M., Wang, L., ... & Zhang, Y. (2019). Facile synthesis of Au-embedded porous carbon from metal-organic frameworks and for sensitive detection of acetaminophen in pharmaceutical products. *Materials Science and Engineering: C*, *95*, 78-85.

[138] Meng, T., Wang, L., Jia, H., Gong, T., Feng, Y., Li, R., ... & Zhang, Y. (2019). Facile synthesis of platinum-embedded zirconia/porous carbons tri-component nanohybrids from metal-

organic framework and their application for ultra-sensitively detection of methyl parathion. *Journal of colloid and interface science*, *536*, 424-430.

[139] Jiang, H. L., Akita, T., Ishida, T., Haruta, M., & Xu, Q. (2011). Synergistic catalysis of Au@ Ag core− shell nanoparticles stabilized on metal− organic framework. *Journal of the American Chemical Society*, *133*(5), 1304-1306.

[140] Siu, P. W., Brown, Z. J., Farha, O. K., Hupp, J. T., & Scheidt, K. A. (2013). A mixed dicarboxylate strut approach to enhancing catalytic activity of a de novo urea derivative of metal–organic framework UiO-67. *Chemical Communications*, *49*(93), 10920-10922.

[141] Liu, X., Akerboom, S., Jong, M. D., Mutikainen, I., Tanase, S., Meijerink, A., & Bouwman, E. (2015). Mixed-lanthanoid metal–organic framework for ratiometric cryogenic temperature sensing. *Inorganic chemistry*, *54*(23), 11323-11329.

[142] Sun, Q., Liu, M., Li, K., Han, Y., Zuo, Y., Wang, J., ... & Guo, X. (2016). Controlled synthesis of mixed-valent Fe-containing metal organic frameworks for the degradation of phenol under mild conditions. *Dalton Transactions*, *45*(19), 7952-7959.

[143] White, R. J., Luque, R., Budarin, V. L., Clark, J. H., & Macquarrie, D. J. (2009). Supported metal nanoparticles on porous materials. Methods and applications. *Chemical Society Reviews*, *38*(2), 481-494.

[144] Goel, S., Wu, Z., Zones, S. I., & Iglesia, E. (2012). Synthesis and catalytic properties of metal clusters encapsulated within small-pore (SOD, GIS, ANA) zeolites. *Journal of the American Chemical Society*, *134*(42), 17688-17695.

[145] Zhu, Q. L., & Xu, Q. (2016). Immobilization of ultrafine metal nanoparticles to high-surface-area materials and their catalytic applications. *Chem*, *1*(2), 220-245.

[146] Radhakrishnan, L., Reboul, J., Furukawa, S., Srinivasu, P., Kitagawa, S., & Yamauchi, Y. (2011). Preparation of microporous carbon fibers through carbonization of Al-based porous coordination polymer (Al-PCP) with furfuryl alcohol. *Chemistry of Materials*, *23*(5), 1225-1231.

[147] Estevez, L., Dua, R., Bhandari, N., Ramanujapuram, A., Wang, P., & Giannelis, E. P. (2013). A facile approach for the synthesis of monolithic hierarchical porous carbons–high performance materials for amine based CO 2 capture and supercapacitor electrode. *Energy & Environmental Science*, *6*(6), 1785-1790.

[148] Chaikittisilp, W., Ariga, K., & Yamauchi, Y. (2013). A new family of carbon materials: synthesis of MOF-derived nanoporous carbons and their promising applications. *Journal of Materials Chemistry A*, *1*(1), 14-19.

[149] Hu, M., Reboul, J., Furukawa, S., Torad, N. L., Ji, Q., Srinivasu, P., ... & Yamauchi, Y. (2012). Direct carbonization of Al-based porous coordination polymer for synthesis of nanoporous carbon. *Journal of the American Chemical Society*, *134*(6), 2864-2867.

[150] Jiang, H. L., Liu, B., Lan, Y. Q., Kuratani, K., Akita, T., Shioyama, H., ... & Xu, Q. (2011). From metal–organic framework to nanoporous carbon: toward a very high surface area and hydrogen uptake. *Journal of the American Chemical Society*, *133*(31), 11854-11857.

[151] Liu, B., Shioyama, H., Akita, T., & Xu, Q. (2008). Metal-organic framework as a template for porous carbon synthesis. *Journal of the American Chemical Society*, *130*(16), 5390-5391.

[152] Yao, Y., Chen, H., Lian, C., Wei, F., Zhang, D., Wu, G., ... & Wang, S. (2016). Fe, Co, Ni nanocrystals encapsulated in nitrogen-doped carbon nanotubes as Fenton-like catalysts for organic pollutant removal. *Journal of hazardous materials*, *314*, 129-139.

[153] Ahsan, M. A., Deemer, E., Fernandez-Delgado, O., Wang, H., Curry, M. L., El-Gendy, A. A., & Noveron, J. C. (2019). Fe nanoparticles encapsulated in MOF-derived carbon for the reduction of 4-nitrophenol and methyl orange in water. *Catalysis Communications*, *130*, 105753.

[154] Liu, J., Lukose, B., Shekhah, O., Arslan, H. K., Weidler, P., Gliemann, H., ... & Wöll, C. (2012). A novel series of isoreticular metal organic frameworks: realizing metastable structures by liquid phase epitaxy. *Scientific reports*, *2*(1), 921.

[155] Li, Y., Hou, G., Yang, J., Xie, J., Yuan, X., Yang, H., & Wang, M. (2016). Facile synthesis of MOF 235 and its superior photocatalytic capability under visible light irradiation. *RSC advances*, *6*(20), 16395-16403.

[156] Tian, Y., Liu, Y., Pang, F., Wang, F., & Zhang, X. (2015). Green synthesis of nanostructured Ni-reduced graphene oxide hybrids and their application for catalytic reduction of 4-nitrophenol. *Colloids and Surfaces A: Physicochemical and Engineering Aspects*, *464*, 96-103.

[157] Wu, X. Q., Zhao, J., Wu, Y. P., Dong, W. W., Li, D. S., Li, J. R., & Zhang, Q. (2018). Ultrafine Pt nanoparticles and amorphous nickel supported on 3D mesoporous carbon derived from Cu-metal–organic framework for efficient methanol oxidation and nitrophenol reduction. *ACS applied materials & interfaces*, *10*(15), 12740-12749.

[158] Han, D., Li, B., Xing, G., Zhang, Y., Chen, Y., Sun, Y., ... & Yang, J. (2018). Facile synthesis of Fe3Pt-Ag nanocomposites for catalytic reduction of methyl orange. *Chemical Research in Chinese Universities*, *34*(6), 871-876.

[159] Das, D., Banerjee, D., Mondal, M., Shett, A., Das, B., Das, N. S., ... & Chattopadhyay, K. K. (2018). Nickel doped graphitic carbon nitride nanosheets and its application for dye degradation by chemical catalysis. *Materials Research Bulletin*, *101*, 291-304.

[160] Soomro, R. A., & Nafady, A. (2015). Catalytic reductive degradation of methyl orange using air resilient copper nanostructures. *Journal of Nanomaterials*, *16*(1), 120-120.

[161] Veerakumar, P., Chen, S. M., Madhu, R., Veeramani, V., Hung, C. T., & Liu, S. B. (2015). Nickel nanoparticle-decorated porous carbons for highly active catalytic reduction of organic dyes and sensitive detection of Hg (II) ions. *ACS applied materials & interfaces*, *7*(44), 24810-24821.

[162] Bureau Of Labor Statistics, National Institute for Occupational Safety and Health (NIOSH) and the Department Of Labor (2003) Respirator Usage in Private Sector Firms. NIOSH, Morgantown.

[163] Ostiguy, C., Soucy, B., Lapointe, G., Woods, C., & Ménard, L. (2008). Les effets sur la santé reliés aux nanoparticules, 2e édition (avril 2008.

[164] Donaldson, K., Stone, V., Clouter, A., Renwick, L., & MacNee, W. (2001). Ultrafine particles Occup Environ Med 58: 211–216. *Find this article online*.

[165] Oberdörster, G. (2000). Toxicology of ultrafine particles: in vivo studies Phil Trans R Soc Lond A 358: 2719–2740. *Find this article online*.

[166] McCullough, N. V., Brosseau, L. M., & Vesley, D. (1997). Collection of three bacterial aerosols by respirator and surgical mask filters under varying conditions of flow and relative humidity. *The Annals of occupational hygiene*, *41*(6), 677-690.

[167] Tran, C. L., Buchanan, D., Cullen, R. T., Searl, A., Jones, A. D., & Donaldson, K. (2000). Inhalation of poorly soluble particles. II. Influence of particle surface area on inflammation and clearance. *Inhalation toxicology*, *12*(12), 1113-1126.

[168] Warheit, D. B., Webb, T. R., Colvin, V. L., Reed, K. L., & Sayes, C. M. (2007). Pulmonary bioassay studies with nanoscale and fine-quartz particles in rats: toxicity is not dependent upon particle size but on surface characteristics. *Toxicological sciences*, *95*(1), 270-280.

[169] Warheit, D. B., Webb, T. R., Reed, K. L., Frerichs, S., & Sayes, C. M. (2007). Pulmonary toxicity study in rats with three forms of ultrafine-TiO2 particles: differential responses related to surface properties. *Toxicology*, *230*(1), 90-104.

[170] Warheit, D. B., Sayes, C. M., Reed, K. L., & Swain, K. A. (2008). Health effects related to nanoparticle exposures: environmental, health and safety considerations for assessing hazards and risks. *Pharmacology & therapeutics*, *120*(1), 35-42.

[171] Lowry, G. V., Alvarez, P., Dionysiou, D., & Biswas, P. (2006). Assessing the risks of manufactured nanomaterials/MR Wiesner [and others]. *Environ Sci Technol*, *40*(14), 4336-4345.

[172] Limbach, L. K., Bereiter, R., Müller, E., Krebs, R., Gälli, R., & Stark, W. J. (2008). Removal of oxide nanoparticles in a model wastewater treatment plant: influence of agglomeration and surfactants on clearing efficiency. *Environmental science & technology*, *42*(15), 5828-5833.

[173] Huang, H. L., Wang, H. P., Wei, G. T., Sun, I. W., Huang, J. F., & Yang, Y. W. (2006). Extraction of nanosize copper pollutants with an ionic liquid. *Environmental science & technology*, *40*(15), 4761-4764.

[174] Kang, P. K., & Shah, D. O. (1997). Filtration of nanoparticles with dimethyldioctadecylammonium bromide treated microporous polypropylene filters. *Langmuir*, *13*(6), 1820-1826.

[175] Qiao, L., Zhu, A., Yang, H., Zeng, W., Dong, R., Tan, P., ... & Pan, J. (2018). Copper–nickel embedded into a nitrogen-doped carbon octahedron as an effective bifunctional electrocatalyst. *Inorganic Chemistry Frontiers*, *5*(9), 2276-2283.

[176] Chen, Y.; Fan, Z.; Zhang, Z.; Niu, W.; Li, C.; Yang, N.; Zhang, H. Two-dimensional metal nanomaterials: Synthesis, properties, and applications. Chem. Rev. 2018, 118, 6409–6455.

[177] Zhu, Y.; Peng, L.; Fang, Z.; Yan, C.; Zhang, X.; Yu, G. Structural engineering of 2D nanomaterials for energy storage and catalysis. Adv. Mater. 2018, 30, 1706347.

[178] Giljohann, D.A.; Seferos, D.S.; Daniel, W.L.; Massich, M.D.; Patel, P.C.; Mirkin, C.A. Gold nanoparticles for biology and medicine. Angew. Chem. Int. Ed. 2010, 49, 3280–3294.

[179] Campelo, J.M.; Luna, D.; Luque, R.; Marinas, J.M.; Romero, A.A. Sustainable preparation of supported metal nanoparticles and their applications in catalysis. ChemSusChem 2009, 2, 18–45.

[180] Sathyavathi, R.; Krishna, M.B.; Rao, S.V.; Saritha, R.; Rao, D.N. Biosynthesis of silver nanoparticles using Coriandrum sativum leaf extract and their application in nonlinear optics. Adv. Sci. Lett. 2010, 3, 138–143.

[181] Kim, T.Y.; Song, D.; Barea, E.M.; Lee, J.H.; Kim, Y.R.; Cho, W.; Kang, Y.S. Origin of the high open-circuit voltage in solid-state dye-sensitized solar cells employing polymer electrolyte. Nano Energy 2016, 28, 455–461.

[182] Wang, J.; Polleux, J.; Lim, J.; Dunn, B. Pseudocapacitive contributions to electrochemical energy storage in TiO2 (anatase) nanoparticles. J. Phys. Chem. C 2007, 111, 14925–14931.

[183] Luo, X.; Morrin, A.; Killard, A.J.; Smyth, M.R. Application of nanoparticles in electrochemical sensors and biosensors. Electroanalysis 2006, 18, 319–326

[184] He, Z.; Zhang, Z.; Bi, S. Nanoparticles for organic electronics applications. Mater. Res. Express 2020, 7, 012004.

[185] Huang, X.; Neretina, S.; El-Sayed, M.A. Gold nanorods: From synthesis and properties to biological and biomedical applications. Adv. Mater. 2009, 21, 4880–4910.

[186] Singh, J.; Dutta, T.; Kim, K.H.; Rawat, M.; Samddar, P.; Kumar, P. 'Green' synthesis of metals and their oxide nanoparticles: Applications for environmental remediation. J. Nanobiotechnol. 2018, 16, 1–24.

[187] Badawy, A.A.; Ghanem, A.F.; Yassin, M.A.; Youssef, A.M.; Rehim, M.H.A. Utilization and characterization of cellulose nanocrystals decorated with silver and zinc oxide nanoparticles for removal of lead ion from wastewater. Environ. Nanotechnol. Monit. Manag. 2021, 16, 100501.

[188] Das, T.K.; Poater, A. Review on the use of heavy metal deposits from water treatment waste towards catalytic chemical syntheses. Int. J. Mol. Sci. 2021, 22, 13383.

[189] Somu, P.; Paul, S. Casein-based biogenic-synthesized zinc oxide nanoparticles simultaneously decontaminate heavy metals, dyes, and pathogenic microbes: A rational strategy for wastewater treatment. J. Chem. Technol. Biotechnol. 2018, 93, 2962–2976.

[190] Hariharan, C. Photocatalytic degradation of organic contaminants in water by ZnO nanoparticles: Revisited. Appl. Catal. A Gen. 2006, 304, 55–61.

[191] Liu, Y.; Deng, Y.; Sun, Z.; Wei, J.; Zheng, G.; Asiri, A.M.; Zhao, D. Hierarchical Cu2S micro sponges constructed from nanosheets for efficient photocatalysis. Small 2013, 9, 2702–2708.

[192] Kumar, S.G.; Rao, K.K. Zinc oxide based photocatalysis: Tailoring surface-bulk structure and related interfacial charge carrier dynamics for better environmental applications. Rsc Adv. 2015, 5, 3306–3351.

[193] Hossain, M.A.; Elias, M.; Sarker, D.R.; Diba, Z.R.; Mithun, J.M.; Azad, M.A.K.; Uddin, M.N. Synthesis of Fe-or Ag-doped TiO2–MWCNT nanocomposite thin films and their visible-light-induced catalysis of dye degradation and antibacterial activity. Res. Chem. Intermed. 2018, 44, 2667–2683.

[194] Wahid, K.A.; Rahim, I.A.; Safri, S.N.; Ariffin, A.H. Synthesis of ZnO nanorods at very low temperatures using ultrasonically pre-treated growth solution. Processes 2023, 11, 708.

[195] Lv, M.S.; Li, C.; Li, Y.N.; Zhang, X.F.; Deng, Z.P.; Cheng, X.L.; Gao, S. Facilely controlled synthesis of porous ZnO nanotubes with rich oxygen vacancies for highly sensitive and selective detection of NO2 at low temperatures. Sens. Actuators B Chem. 2023, 375, 132865.

[196] Wang, X.; Song, J.; Wang, Z.L. Nanowire and nanobelt arrays of zinc oxide from synthesis to properties and to novel devices. J. Mater. Chem. 2007, 17, 711–720.

[197] Kumar, R.; Kumar, G.; Umar, A. ZnO nano-mushrooms for photocatalytic degradation of methyl orange. Mater. Lett. 2013, 97, 100–103.

[198] Sharma, H.; Kaur, N.; Singh, N.; Jang, D.O. Synergetic catalytic effect of ionic liquids and ZnO nanoparticles on the selective synthesis of 1, 2-disubstituted benzimidazoles using a ball-milling technique. Green Chem. 2015, 17, 4263–4270.

[199] Krobthong, S.; Rungsawang, T.; Wongrerkdee, S. Comparison of ZnO Nanoparticles Prepared by Precipitation and Combustion for UV and Sunlight-Driven Photocatalytic Degradation of Methylene Blue. Toxics 2023, 11, 266.

[200] Jalali, T.; Ghanavati, F.; Osfouri, S. Green synthesis of ZnO nanoparticles using marine brown algae (Cystoseira) extract comprising sol–gel, and combustion techniques based on dye-sensitized solar cells application. Int. J. Mod. Phys. B 2023, 245017.

[201] Alberti, S.; Basciu, I.; Vocciante, M.; Ferretti, M. Experimental and physicochemical comparison of ZnO nanoparticles' activity for photocatalytic applications in wastewater treatment. Catalysts 2021, 11, 678.

[202] Yu, J.; Liu, X.; Wang, G.; Zhi, H.; Dong, J.; Hao, J.; Zhang, X.; Liu, B. Synthesis of the porous ZnO nanosheets and tio2/zno/fto composite films by a low-temperature hydrothermal method and their applications in photocatalysis and electrochromism. Coatings 2022, 12, 695

[203] Sansenya, T.; Masri, N.; Chankhanittha, T.; Senasu, T.; Piriyanon, J.; Mukdasai, S.; Nanan, S. Hydrothermal synthesis of ZnO photocatalyst for detoxification of anionic azo dyes and antibiotics. J. Phys. Chem. Solids 2022, 160, 110353.

[204] Ding, J.; Chen, S.; Han, N.; Shi, Y.; Hu, P.; Li, H.; Wang, J. Aerosol-assisted chemical vapor deposition of nanostructured ZnO thin films for NO2 and ethanol monitoring. Ceram. Int. 2020, 46, 15152–15158.

[205] Ponja, S.D.; Sathasivam, S.; Parkin, I.P.; Carmalt, C.J. Highly conductive and transparent gallium-doped zinc oxide thin films via chemical vapor deposition. Sci. Rep. 2020, 10, 638.

[206] Shkir, M.; Palanivel, B.; Khan, A.; Kumar, M.; Chang, J.H.; Mani, A.; AlFaify, S. Enhanced photocatalytic activities of facile auto-combustion synthesized ZnO nanoparticles for wastewater treatment: An impact of Ni doping. Chemosphere 2022, 291, 132687.

[207] Sultana, K.A.; Islam, M.T.; Silva, J.A.; Turley, R.S.; Hernandez-Viezcas, J.A.; Gardea-Torresdey, J.L.; Noveron, J.C. Sustainable synthesis of zinc oxide nanoparticles for photocatalytic degradation of organic pollutant and generation of hydroxyl radical. J. Mol. Liq. 2020, 307, 112931.

[208] Naik, M.A.; Mishra, B.G.; Dubey, A. Combustion synthesized WO3–ZrO2 nanocomposites as catalysts for the solvent-free synthesis of coumarins. Colloids Surf. A Physicochem. Eng. Asp. 2008, 317, 234–238.

[209] Ngulube, T.; Gumbo, J.R.; Masindi, V.; Maity, A. An update on synthetic dye adsorption onto clay-based minerals: A state-of-art review. J. Environ. Manag. 2017, 191, 35–57.

[210] Morcillo-Martín, R.; Espinosa, E.; Rabasco-Vílchez, L.; Sanchez, L.M.; de Haro, J.; Rodríguez, A. Cellulose nanofiber-based aerogels from wheat straw: Influence of surface load and lignin content on their properties and dye removal capacity. Biomolecules 2022, 12, 232.

[211] Maleki, A.; Moradi, F.; Shahmoradi, B.; Rezaee, R.; Lee, S.M. The photocatalytic removal of diazinon from aqueous solutions using tungsten oxide doped zinc oxide nanoparticles immobilized on a glass substrate. J. Mol. Liq. 2020, 297, 111918.

[212] Szostak, K.; Banach, M. Sorption and photocatalytic degradation of methylene blue on bentonite-ZnO-CuO nanocomposite. J. Mol. Liq. 2019, 286, 110859.

[213] Kausar, A.; Iqbal, M.; Javed, A.; Aftab, K.; Bhatti, H.N.; Nouren, S. Dyes adsorption using clay and modified clay: A review. J. Mol. Liq. 2018, 256, 395–407.

[214] Chen, Y.; He, F.; Ren, Y.; Peng, H.; Huang, K. Fabrication of chitosan/PAA multilayer onto magnetic microspheres by LbL method for removal of dyes. J. Chem. Eng. 2014, 249, 79–92.

[215] Adeel, M.; Saeed, M.; Khan, I.; Muneer, M.; Akram, N. Synthesis and characterization of Co–ZnO, and evaluation of its photocatalytic activity for photodegradation of methyl orange. ACS Omega 2021, 6, 1426–1435.

[216] Aljuaid, A.; Almehmadi, M.; Alsaiari, A.A.; Allahyani, M.; Abdulaziz, O.; Alsharif, A.; Alsaiari, J.A.; Saih, M.; Alotaibi, R.T.; Khan, I. g-C3N4 Based Photocatalyst for the Efficient Photodegradation of Toxic Methyl Orange Dye: Recent Modifications and Future Perspectives. Molecules 2023, 28, 3199.

[217] Bhosale, A.; Kadam, J.; Gade, T.; Sonawane, K.; Garadkar, K. Efficient photodegradation of methyl orange and bactericidal activity of Ag-doped ZnO nanoparticles. J. Indian Chem. Soc. 2023, 100, 100920.

[218] Khan, S.; Naushad, M.; Govarthanan, M.; Iqbal, J.; Alfadul, S.M. Emerging contaminants of high concern for the environment: Current trends and future research. Environ. Res. 2022, 207, 112609.

[219] Hasnat, M.A.; Safwan, J.A.; Islam, M.S.; Rahman, Z.; Karim, M.R.; Pirzada, T.J.; Rahman, M.M. Electrochemical decolorization of Methylene blue at Pt electrode in KCl solution for environmental remediation. J. Ind. Eng. Chem. 2015, 21, 787–791.

[220] Ljubas, D.; Smoljanić, G.; Juretić, H. Degradation of Methyl Orange and Congo Red dyes using TiO2 nanoparticles activated by the solar and the solar-like radiation. J. Environ. Manag. 2015, 161, 83–91.

[221] Piaskowski, K.; Świderska-Dąbrowska, R.; Zarzycki, P.K. Dye removal from water and wastewater using various physical, chemical, and biological processes. J. AOAC Int. 2018, 101, 1371–1384.

[222] Islam, M.T.; Jing, H.; Yang, T.; Zubia, E.; Goos, A.G.; Bernal, R.A.; Noveron, J.C. Fullerene stabilized gold nanoparticles supported on titanium dioxide for enhanced photocatalytic degradation of methyl orange and catalytic reduction of 4-nitrophenol. J. Environ. Chem. Eng. 2018, 6, 3827–3836.

[223] Islam, M.T.; Dominguez, A.; Turley, R.S.; Kim, H.; Sultana, K.A.; Shuvo, M.A.I.; Noveron, J.C. Development of photocatalytic paint based on TiO2 and photopolymer resin for the degradation of organic pollutants in water. Sci. Total Environ. 2020, 704, 135406.

[224] Islam, M.T.; Dominguez, A.; Alvarado-Tenorio, B.; Bernal, R.A.; Montes, M.O.; Noveron, J.C. Sucrose-mediated fast synthesis of zinc oxide nanoparticles for the photocatalytic degradation of organic pollutants in water. ACS Omega 2019, 4, 6560–6572.

[225] Meena, P.L.; Poswal, K.; Surela, A.K. Facile synthesis of ZnO nanoparticles for the effective photodegradation of malachite green dye in aqueous solution. Water Environ. J. 2022, 36, 513–524

[226] Becheri, A.; Dürr, M.; Lo Nostro, P.; Baglioni, P. Synthesis and characterization of zinc oxide nanoparticles: Application to textiles as UV-absorbers. J. Nanopart. Res. 2008, 10, 679–689.

[227] Tripathy, N.; Ahmad, R.; Song, J.E.; Ko, H.A.; Hahn, Y.B.; Khang, G. Photocatalytic degradation of methyl orange dye by ZnO nanoneedle under UV irradiation. Mater. Lett. 2014, 136, 171–174.

[228] Molla, M.A.I.; Furukawa, M.; Tateishi, I.; Katsumata, H.; Kaneko, S. Studies of effects of calcination temperature on the crystallinity and optical properties of Ag-doped ZnO nanocomposites. J. Compos. Sci. 2019, 3, 18.

[229] Kaur, J.; Bansal, S.; Singhal, S. Photocatalytic degradation of methyl orange using ZnO nanopowders synthesized via thermal decomposition of oxalate precursor method. Phys. B Condens. Matter 2013, 416, 33–38.

[230] Balcha, A.; Yadav, O.P.; Dey, T. Photocatalytic degradation of methylene blue dye by zinc oxide nanoparticles obtained from precipitation and sol-gel methods. Environ. Sci. Pollut. Res. 2016, 23, 25485–25493.

[231] Shen, J.H.; Chiang, T.H.; Tsai, C.K.; Jiang, Z.W.; Horng, J.J. Mechanistic insights into hydroxyl radical formation of Cu-doped ZnO/g-C3N4 composite photocatalysis for enhanced degradation of ciprofloxacin under visible light: Efficiency, kinetics, products identification and toxicity evaluation. J. Environ. Chem. Eng. 2022, 10, 107352.

[232] Tahir, M., Pan, L., Idrees, F., Zhang, X., Wang, L., Zou, J. J., & Wang, Z. L. (2017). Electrocatalytic oxygen evolution reaction for energy conversion and storage: a comprehensive review. *Nano Energy*, *37*, 136-157.

[233] Kim, J. S., Kim, B., Kim, H., & Kang, K. (2018). Recent progress on multimetal oxide catalysts for the oxygen evolution reaction. *Advanced Energy Materials*, *8*(11), 1702774.

[234] Fabbri, E., & Schmidt, T. J. (2018). Oxygen evolution reaction—the enigma in water electrolysis. *Acs Catalysis*, *8*(10), 9765-9774.

[235] Wu, Z. P., Lu, X. F., Zang, S. Q., & Lou, X. W. (2020). Non-noble-metal-based electrocatalysts toward the oxygen evolution reaction. *Advanced Functional Materials*, *30*(15), 1910274.

[236] Zhu, Y., Tahini, H. A., Hu, Z., Chen, Z. G., Zhou, W., Komarek, A. C., ... & Shao, Z. (2020). Boosting oxygen evolution reaction by creating both metal ion and lattice-oxygen active sites in a complex oxide. *Advanced Materials*, *32*(1), 1905025.

[237] Zhuang, L., Ge, L., Yang, Y., Li, M., Jia, Y., Yao, X., & Zhu, Z. (2017). Ultrathin iron-cobalt oxide nanosheets with abundant oxygen vacancies for the oxygen evolution reaction. *Advanced Materials*, *29*(17), 1606793.

[238] Xu, H., Shang, H., Wang, C., Jin, L., Chen, C., Wang, C., & Du, Y. (2020). Three-dimensional open CoMoOx/CoMoSx/CoSx nanobox electrocatalysts for efficient oxygen evolution reaction. *Applied Catalysis B: Environmental*, *265*, 118605.

[239] Wang, X. L., Dong, L. Z., Qiao, M., Tang, Y. J., Liu, J., Li, Y., ... & Lan, Y. Q. (2018). Exploring the performance improvement of the oxygen evolution reaction in a stable bimetal–organic framework system. *Angewandte Chemie International Edition*, *57*(31), 9660-9664.

[240] Feng, C., Faheem, M. B., Fu, J., Xiao, Y., Li, C., & Li, Y. (2020). Fe-based electrocatalysts for oxygen evolution reaction: progress and perspectives. *ACS Catalysis*, *10*(7), 4019-4047.

[241] Suen, N. T., Hung, S. F., Quan, Q., Zhang, N., Xu, Y. J., & Chen, H. M. (2017). Electrocatalysis for the oxygen evolution reaction: recent development and future perspectives. *Chemical Society Reviews*, *46*(2), 337-365.

[242] Song, F., Busch, M. M., Lassalle-Kaiser, B., Hsu, C. S., Petkucheva, E., Bensimon, M., ... & Hu, X. (2019). An unconventional iron nickel catalyst for the oxygen evolution reaction. *ACS central science*, *5*(3), 558-568.

[243] Divanis, S., Kutlusoy, T., Boye, I. M. I., Man, I. C., & Rossmeisl, J. (2020). Oxygen evolution reaction: a perspective on a decade of atomic scale simulations. *Chemical science*, *11*(11), 2943-2950.

[244] Zhang, J., Zhao, Z., Xia, Z., & Dai, L. (2015). A metal-free bifunctional electrocatalyst for oxygen reduction and oxygen evolution reactions. *Nature nanotechnology*, *10*(5), 444-452.

[245] Wang, H. F., Chen, L., Pang, H., Kaskel, S., & Xu, Q. (2020). MOF-derived electrocatalysts for oxygen reduction, oxygen evolution and hydrogen evolution reactions. *Chemical Society Reviews*, *49*(5), 1414-1448.

[246] Xue, Z., Liu, K., Liu, Q., Li, Y., Li, M., Su, C. Y., ... & Li, G. (2019). Missing-linker metal-organic frameworks for oxygen evolution reaction. *Nature communications*, *10*(1), 1-8.

[247] Xu, L., Jiang, Q., Xiao, Z., Li, X., Huo, J., Wang, S., & Dai, L. (2016). Plasma-engraved Co3O4 nanosheets with oxygen vacancies and high surface area for the oxygen evolution reaction. *Angewandte Chemie*, *128*(17), 5363-5367.

[248] McCrory, C. C., Jung, S., Peters, J. C., & Jaramillo, T. F. (2013). Benchmarking heterogeneous electrocatalysts for the oxygen evolution reaction. *Journal of the American Chemical Society*, *135*(45), 16977-16987.

[249] Fabbri, E., Habereder, A., Waltar, K., Kötz, R., & Schmidt, T. J. (2014). Developments and perspectives of oxide-based catalysts for the oxygen evolution reaction. *Catalysis Science & Technology*, *4*(11), 3800-3821.

[250] Habibi Y, Lucia LA, Rojas O. Cellulose nanocrystals: chemistry, selfassembly, and applications. *Chem Rev*. 2010;110(6):3479-3500.

[251] De Souza Lima MM, Borsali R. Rodlike cellulose microcrystals: structure, properties, and applications. *Macromol Rapid Commun*. 2004;25: 771-787.

[252] Siqueira G, Abdillahi H, Bras J, Dufresne A. High reinforcing capability cellulose nanocrystals extracted from Syngonanthus nitens (Capim Dourado). *Cellulose*. 2010;17:289-298.

[253] Reale Batista MD, Drzal LT. Carbon fiber/epoxy matrix composite interphases modified with cellulose nanocrystals. *Compo Sci Technol*. 2018;164:274-281.

[254] Li, Z.; Yao, C.; Wang, F.; Cai, Z.; Wang, X. Cellulose nanofiber-templated three-dimension TiO2 hierarchical nanowire network for photoelectrochemical photoanode. *Nanotechnology* 2014, *25* (50), 504005.

[255] Li, Z.; Yao, C.; Yu, Y.; Cai, Z.; Wang, X. Highly Efficient Capillary Photoelectrochemical Water Splitting Using Cellulose Nanofiber-Templated TiO2 Photoanodes. *Advanced Materials* 2014, *26* (14), 2262-2267.

[256] Li, Z.; Yao, C.; Wang, Y.-C.; Mikael, S.; Gunasekaran, S.; Ma, Z.; Cai, Z.; Wang, X. High-density platinum nanoparticle-decorated titanium dioxide nanofiber networks for efficient capillary photocatalytic hydrogen generation. *Journal of Materials Chemistry A* **2016**, *4* (30), 11672-11679.

[257] Nair, S. S., Chen, J., Slabon, A., & Mathew, A. P. (2020). Converting cellulose nanocrystals into photocatalysts by functionalisation with titanium dioxide nanorods and gold nanocrystals. *RSC advances*, *10*(61), 37374-37381.

[258] Reiner, R. S., & Rudie, A. W. (2013). Process scale-up of cellulose nanocrystal production to 25 kg per batch at the forest products laboratory. *In: Production and applications of Cellulose nanomaterials, TAPPI Press, Chapter 1.1, 2013; pp. 21-24.*, *1*, 21-24.

[259] Reiner, R. S., & Rudie, A. W. (2017). Experiences with scaling-up production of TEMPO-grade cellulose nanofibrils. In *Nanocelluloses: Their preparation, properties, and applications* (pp. 227-245). American Chemical Society.

[260] Saito, T., Kimura, S., Nishiyama, Y., & Isogai, A. (2007). Cellulose nanofibers prepared by TEMPO-mediated oxidation of native cellulose. *Biomacromolecules*, *8*(8), 2485-2491.

[261] Yoon SH, Jin HJ, Kook MC, Pyun YR. Electrically conductive bacterial cellulose by incorporation of carbon nanotubes. Biomacromolecules. 2006 Apr 10;7(4):1280-4.

[262] He Z, Jiang Y, Sun D, Dai L, Wang H. Advanced LiTi 2 (PO 4) 3/C anode by incorporation of carbon nanotubes for aqueous lithium-ion batteries. Ionics. 2017 Mar;23:575-83.

[263] MacDonald RA, Voge CM, Kariolis M, Stegemann JP. Carbon nanotubes increase the electrical conductivity of fibroblast-seeded collagen hydrogels. Acta biomaterialia. 2008 Nov 1;4(6):1583-92.

[264] Gökçeli G, Karatepe N. Improving the properties of indium tin oxide thin films by the incorporation of carbon nanotubes with solution-based techniques. Thin Solid Films. 2020 Mar 1;697:137844.

[265] Jiang X, Drzal LT. Improving electrical conductivity and mechanical properties of high density polyethylene through incorporation of paraffin wax coated exfoliated graphene

nanoplatelets and multi-wall carbon nano-tubes. Composites Part A: Applied Science and Manufacturing. 2011 Nov 1;42(11):1840-9.

[266] Duongthipthewa A, Su Y, Zhou L. Electrical conductivity and mechanical property improvement by low-temperature carbon nanotube growth on carbon fiber fabric with nanofiller incorporation. Composites Part B: Engineering. 2020 Feb 1;182:107581.

[267] Dreaden, E. C., Alkilany, A. M., Huang, X., Murphy, C. J., & El-Sayed, M. A. (2012). The golden age: gold nanoparticles for biomedicine. *Chemical Society Reviews*, *41*(7), 2740-2779.

[268] Stark, W. J., Stoessel, P. R., Wohlleben, W., & Hafner, A. J. C. S. R. (2015). Industrial applications of nanoparticles. *Chemical Society Reviews*, *44*(16), 5793-5805.

[269] Zhang, Y., Chu, W., Foroushani, A. D., Wang, H., Li, D., Liu, J., ... & Yang, W. (2014). New gold nanostructures for sensor applications: a review. *Materials*, *7*(7), 5169-5201.

[270] Huang, Y. F., Lin, Y. W., Lin, Z. H., & Chang, H. T. (2009). Aptamer-modified gold nanoparticles for targeting breast cancer cells through light scattering. *Journal of Nanoparticle Research*, *11*, 775-783.

[271] Matsubara, K., Kawata, S., & Minami, S. (1988). Optical chemical sensor based on surface plasmon measurement. *Applied optics*, *27*(6), 1160-1163.

[272] Ding, L., Hao, C., Xue, Y., & Ju, H. (2007). A bio-inspired support of gold nanoparticles−chitosan nanocomposites gel for immobilization and electrochemical study of K562 Leukemia cells. *Biomacromolecules*, *8*(4), 1341-1346.

[273] Agarwal, N., Solanki, V. S., Pare, B., Singh, N., & Jonnalagadda, S. B. (2023). Current trends in nanocatalysis for green chemistry and its applications-a mini-review. *Current Opinion in Green and Sustainable Chemistry*, 100788.

[274] Ueda, A., Oshima, T., & Haruta, M. (1997). Reduction of nitrogen monoxide with propene in the presence of oxygen and moisture over gold supported on metal oxides. *Applied catalysis B: environmental*, *12*(2-3), 81-93.

[275] Andreeva, D., Tabakova, T., Idakiev, V., Christov, P., & Giovanoli, R. (1998). Au/α-Fe2O3 catalyst for water–gas shift reaction prepared by deposition–precipitation. *Applied Catalysis A: General*, *169*(1), 9-14.

[276] Jimenez-Falcao, S., Méndez-Arriaga, J. M., García-Almodóvar, V., García-Valdivia, A. A., & Gómez-Ruiz, S. (2022). Gold Nanozymes: Smart Hybrids with Outstanding Applications. *Catalysts*, *13*(1), 13.

[277] Coelho, S. C., Rocha, S., Pereira, M. C., Coelho, M. A., & Juzenas, P. (2013, February). Functionalized gold nanoparticles for drug delivery. In *2013 IEEE 3rd Portuguese Meeting in Bioengineering (ENBENG)* (pp. 1-4). IEEE.

[278] Paciotti, G. F., Myer, L., Weinreich, D., Goia, D., Pavel, N., McLaughlin, R. E., & Tamarkin, L. (2004). Colloidal gold: a novel nanoparticle vector for tumor directed drug delivery. *Drug delivery*, *11*(3), 169-183.

[279] Rao, C. R., Kulkarni, G. U., Thomas, P. J., & Edwards, P. P. (2000). Metal nanoparticles and their assemblies. *Chemical Society Reviews*, *29*(1), 27-35.

[280] Lisiecki, I. (2005). Size, shape, and structural control of metallic nanocrystals. *The Journal of Physical Chemistry B*, *109*(25), 12231-12244.

[281] Murphy, C. J., Sau, T. K., Gole, A. M., Orendorff, C. J., Gao, J., Gou, L., ... & Li, T. (2005). Anisotropic metal nanoparticles: synthesis, assembly, and optical applications. *The Journal of Physical Chemistry B*, *109*(29), 13857-13870.

[282] Sasidharan, M., Nakashima, K., Gunawardhana, N., Yokoi, T., Ito, M., Inoue, M., ... & Tatsumi, T. (2011). Periodic organosilica hollow nanospheres as anode materials for lithium ion rechargeable batteries. *Nanoscale*, *3*(11), 4768-4773.

[283] Smetana, A. B., Wang, J. S., Boeckl, J., Brown, G. J., & Wai, C. M. (2007). Fine-tuning size of gold nanoparticles by cooling during reverse micelle synthesis. *Langmuir*, *23*(21), 10429-10432.

[284] Hiramatsu, H., & Osterloh, F. E. (2004). A simple large-scale synthesis of nearly monodisperse gold and silver nanoparticles with adjustable sizes and with exchangeable surfactants. *Chemistry of materials*, *16*(13), 2509-2511.

[285] Johnson, C. J., Dujardin, E., Davis, S. A., Murphy, C. J., & Mann, S. (2002). Growth and form of gold nanorods prepared by seed-mediated, surfactant-directed synthesis. *Journal of Materials Chemistry*, *12*(6), 1765-1770.

[286] Rowsell, J. L., & Yaghi, O. M. (2004). Metal–organic frameworks: a new class of porous materials. *Microporous and mesoporous materials*, *73*(1-2), 3-14.

[287] Furukawa, H., Cordova, K. E., O'Keeffe, M., & Yaghi, O. M. (2013). The chemistry and applications of metal-organic frameworks. *Science*, *341*(6149), 1230444.

[288] Kuppler, R. J., Timmons, D. J., Fang, Q. R., Li, J. R., Makal, T. A., Young, M. D., ... & Zhou, H. C. (2009). Potential applications of metal-organic frameworks. *Coordination Chemistry Reviews*, *253*(23-24), 3042-3066.

[289] Feng, X., Ding, X., & Jiang, D. (2012). Covalent organic frameworks. *Chemical Society Reviews*, *41*(18), 6010-6022.

[290] Liu, R., Tan, K. T., Gong, Y., Chen, Y., Li, Z., Xie, S., ... & Jiang, D. (2021). Covalent organic frameworks: an ideal platform for designing ordered materials and advanced applications. *Chemical Society Reviews*, *50*(1), 120-242.

[291] Alahakoon, S. B., Diwakara, S. D., Thompson, C. M., & Smaldone, R. A. (2020). Supramolecular design in 2D covalent organic frameworks. *Chemical Society Reviews*, *49*(5), 1344-1356.

[292] Pandey, P., Katsoulidis, A. P., Eryazici, I., Wu, Y., Kanatzidis, M. G., & Nguyen, S. T. (2010). Imine-linked microporous polymer organic frameworks. *Chemistry of Materials*, *22*(17), 4974-4979.

[293] Ding, S. Y., Dong, M., Wang, Y. W., Chen, Y. T., Wang, H. Z., Su, C. Y., & Wang, W. (2016). Thioether-based fluorescent covalent organic framework for selective detection and facile removal of mercury (II). *Journal of the American Chemical Society*, *138*(9), 3031-3037.

[294] Li, Z., Zhang, Y., Xia, H., Mu, Y., & Liu, X. (2016). A robust and luminescent covalent organic framework as a highly sensitive and selective sensor for the detection of Cu 2+ ions. *Chemical Communications*, *52*(39), 6613-6616.

[295] Wang, M., Wang, F., Wang, Y., Zhang, W., & Chen, X. (2015). Polydiacetylene-based sensor for highly sensitive and selective Pb2+ detection. *Dyes and Pigments*, *120*, 307-313.

[296] Pumtang, S., Siripornnoppakhun, W., Sukwattanasinitt, M., & Ajavakom, A. (2011). Solvent colorimetric paper-based polydiacetylene sensors from diacetylene lipids. *Journal of colloid and interface science*, *364*(2), 366-372.

[297] Furukawa, H., & Yaghi, O. M. (2009). Storage of hydrogen, methane, and carbon dioxide in highly porous covalent organic frameworks for clean energy applications. *Journal of the American Chemical Society*, *131*(25), 8875-8883.

[298] Li, Z., Zhi, Y., Feng, X., Ding, X., Zou, Y., Liu, X., & Mu, Y. (2015). An azine-linked covalent organic framework: synthesis, characterization and efficient gas storage. *Chemistry–A European Journal*, *21*(34), 12079-12084.

[299] Xu, H., Gao, J., & Jiang, D. (2015). Stable, crystalline, porous, covalent organic frameworks as a platform for chiral organocatalysts. *Nature chemistry*, *7*(11), 905-912.

[300] Ding, S. Y., Gao, J., Wang, Q., Zhang, Y., Song, W. G., Su, C. Y., & Wang, W. (2011). Construction of covalent organic framework for catalysis: Pd/COF-LZU1 in Suzuki–Miyaura coupling reaction. *Journal of the American Chemical Society*, *133*(49), 19816-19822.

[301] Fang, Q., Gu, S., Zheng, J., Zhuang, Z., Qiu, S., & Yan, Y. (2014). 3D microporous base-functionalized covalent organic frameworks for size-selective catalysis. *Angewandte Chemie*, *126*(11), 2922-2926.

[302] Lee, J., Kim, S. M., & Lee, I. S. (2014). Functionalization of hollow nanoparticles for nanoreactor applications. *Nano Today*, *9*(5), 631-667.

[303] El-Kaderi, H. M., Hunt, J. R., Mendoza-Cortés, J. L., Côté, A. P., Taylor, R. E., O'Keeffe, M., & Yaghi, O. M. (2007). Designed synthesis of 3D covalent organic frameworks. *Science*, *316*(5822), 268-272.

[304] Wan, S., Guo, J., Kim, J., Ihee, H., & Jiang, D. (2009). A photoconductive covalent organic framework: self-condensed arene cubes composed of eclipsed 2D polypyrene sheets for photocurrent generation. *Angewandte Chemie International Edition*, *48*(30), 5439-5442.

[305] Spitler, E. L., & Dichtel, W. R. (2010). Lewis acid-catalysed formation of two-dimensional phthalocyanine covalent organic frameworks. *Nature chemistry*, *2*(8), 672-677.

[306] Tilford, R. W., Mugavero III, S. J., Pellechia, P. J., & Lavigne, J. J. (2008). Tailoring microporosity in covalent organic frameworks. *Advanced Materials*, *20*(14), 2741-2746.

[307] Kuhn, P., Antonietti, M., & Thomas, A. (2008). Porous, covalent triazine-based frameworks prepared by ionothermal synthesis. *Angewandte Chemie International Edition, 47*(18), 3450-3453.

[308] Bojdys, M. J., Jeromenok, J., Thomas, A., & Antonietti, M. (2010). Rational extension of the family of layered, covalent, triazine-based frameworks with regular porosity. *Advanced materials*, *22*(19), 2202-2205.

[309] Uribe-Romo, F. J., Hunt, J. R., Furukawa, H., Klock, C., O'Keeffe, M., & Yaghi, O. M. (2009). A crystalline imine-linked 3-D porous covalent organic framework. *Journal of the American Chemical Society*, *131*(13), 4570-4571.

[310] Kandambeth, S., Mallick, A., Lukose, B., Mane, M. V., Heine, T., & Banerjee, R. (2012). Construction of crystalline 2D covalent organic frameworks with remarkable chemical (acid/base) stability via a combined reversible and irreversible route. *Journal of the American Chemical Society*, *134*(48), 19524-19527.

[311] Beaudoin, D., Maris, T., & Wuest, J. D. (2013). Constructing monocrystalline covalent organic networks by polymerization. *Nature chemistry*, *5*(10), 830-834.

[312] Shi, W., & Lei, A. (2014). 1, 3-Diyne chemistry: synthesis and derivations. *Tetrahedron Letters*, *55*(17), 2763-2772.

[313] Singh, A., Arango, J. C., Shi, A., d'Aliberti, J. B., & Claridge, S. A. (2023). Surface-Templated Glycopolymer Nanopatterns Transferred to Hydrogels for Designed Multivalent Carbohydrate–Lectin Interactions across Length Scales. *Journal of the American Chemical Society*, *145*(3), 1668-1677.

[314] Indra, A., Menezes, P. W., Sahraie, N. R., Bergmann, A., Das, C., Tallarida, M., ... & Driess, M. (2014). Unification of catalytic water oxidation and oxygen reduction reactions: amorphous

beat crystalline cobalt iron oxides. *Journal of the American chemical society*, *136*(50), 17530-17536.

Vita.

Javier Hernandez Ortega was born in Cuba and graduated with a BSc from the University of Havana in 2016. In June 2018, he embarked on his Ph.D. journey in Chemistry at the University of Texas at El Paso, under the guidance of Prof. Juan Noveron. His research primarily revolved around the synthesis and characterization of novel materials and inorganic compounds. Javier's work also encompassed the design of solid supports tailored for the encapsulation of nanomaterials, with the potential for applications in water remediation and electrocatalysis. Throughout his academic journey, he has made notable contributions, coauthoring four peer-reviewed articles that have added to the body of scientific knowledge. In addition, he has had the privilege of supervising the research of five undergraduate students during their tenure in the laboratory, providing mentorship and guidance.